



N°d'ordre NNT : 2016LYSEI150

THESE de DOCTORAT DE L'UNIVERSITE DE LYON
opérée au sein de
I'INSA de Lyon

Ecole Doctorale 34
Matériaux

Soutenue publiquement 13/12/2016, par :
Osamu Waseda

**Atomic scale investigation of aging in
metals**

Devant le jury composé de :

Becquart, Charlotte Professeur Université Lille I Présidente

Rodney, David Professeur Université Lyon I	Rapporteur
Neugebauer, David Professeur MPI Düsseldorf	Rapporteur
Jelea, Andrei Docteur IRSN	Examineur
Ribeiro, Fabienne Docteur IRSN	Examineur

Perez, Michel Professeur INSA Lyon	Directeur de thèse
Morthomas, Julien Docteur INSA Lyon	Co-directeur de thèse
Chantrenne, Patrice Professeur INSA Lyon	Invité

*Intussen moet ik m'n denkbelden hoog en droog houden, in de tijden die komen
zijn ze misschien toch nog uit te voeren!*

Contents

0	Introduction	1
1	Simulation methodology	8
1.1	Molecular Dynamics	9
1.2	Energy minimization	10
1.3	Metropolis Monte Carlo	11
1.4	Atomistic Kinetic Monte Carlo	13
1.4.1	CI-NEB	14
1.4.2	LinCoSS	16
1.5	Choice of interatomic potential	18
2	Ordering of Carbon in Supersaturated α-Fe	20
2.1	Introduction	21
2.2	Thermodynamic calculation	25
2.3	Simulation Methodology	28
2.3.1	Metropolis Monte Carlo	28
2.3.2	Molecular Dynamics	29
2.3.3	Simulation box	30
2.3.4	Radial distribution function	31
2.4	Results	31
2.4.1	Convergence of simulations	31
2.4.2	Order-Disorder behaviour given by MMC and thermodynamical calculation	32
2.4.3	Order-disorder transition diagram of MD	37
2.4.4	Interpretation of the order-disorder transition given through thermodynamical calculation, MMC and MD	38
2.4.5	Formation of α'' -Fe and twinned martensite	39
2.5	Conclusion	41

3	Formation of carbon Cottrell atmospheres in bcc iron and their effect on the stress field around edge and screw dislocations	44
3.1	Introduction	45
3.2	Method	46
3.2.1	Simulation box	46
3.2.2	Metropolis Monte Carlo	48
3.3	Results	50
3.3.1	Convergence of MMC simulations	50
3.3.2	Carbon density distribution of Cottrell atmospheres	51
3.3.3	Evolution of stress field	54
3.3.4	Carbon ordering around dislocations	56
3.3.5	Evaluation of λ and comparison with the model of Cottrell	57
3.4	Conclusion	63
4	Formation kinetics of carbon Cottrell atmospheres	64
4.1	Introduction	65
4.2	Limit of LinCoSS	66
4.2.1	Treatment of the ecto-LinCoSS zone	71
4.3	Chemical correction	73
4.4	Elastic correction	76
4.5	Treatment of carbon atoms outside AKMC boundary	78
4.6	Final scheme of AKMC	80
4.7	Results	82
4.8	Conclusion	85
5	Grain boundary stabilization by solute segregation in nanocrystalline Ni	88
5.1	Introduction	89
5.2	Computational approach	90
5.2.1	Interatomic potential	90
5.2.2	Metropolis Monte Carlo	91
5.2.3	Molecular Dynamics Simulation	91
5.2.4	Calculation of orientation angle	92
5.3	Results and Discussion	92
5.3.1	Metropolis Monte Carlo	92
5.3.2	Molecular Dynamics	93
5.4	Conclusions	96
6	Conclusion and perspectives	98

Appendices	103
A Assessment of the order parameter via free energy calculation	104
B Anisotropic elasticity theory	108
C How to calculate attempt frequency κ	116
D Correction of LinCoSS	118
D.1 First possibility: Stress gradient	119
D.2 Second possibility: Reliability of measurement with CI-NEB	120
D.3 Third possibility: Dependence on cross terms	122
D.4 Validity of LinCoSS: Conclusion	128
E Chemical correction library	129
E.1 Creation of chemical correction library	129
E.2 Implementation in AKMC	131
F Elastic correction library	133
F.1 Creation of elastic correction library	133
F.2 Implementation in AKMC	134

Nomenclature

AKMC	Atomistic Kinetic Monte Carlo
CG	Conjugate Gradient
CI-NEB	Climbing Image Nudged Elastic Band
DFT	Density Functional Theory
EAM	Embedded Atom Method
LinCoSS	Linear Combination of Stress States
MD	Molecular Dynamics
MMC	Metropolis Monte Carlo
MS	Molecular Statics
RB-potential	Raulot-Becquart potential

Chapter 0

Introduction

A number of structure materials, such as steel, are subject to aging that limits their physical properties. According to the theory of Cottrell and Bilby [Cottrell and Bilby, 1949], solute atoms, such as carbon or nitrogen, segregate around structural defects, such as dislocations, as the structural defects attract the solute atoms through their stress field. This creates clouds of solute atoms around dislocations, which are called “Cottrell Atmospheres”. Cottrell atmospheres inhibit the movement of initially mobile dislocations [Strudel *et al.*, 1979]. As a result, the dislocations require more force to move, which results in an augmentation of yield stress [De *et al.*, 2000; Lavaire *et al.*, 2001] (*cf.* fig. 1 (a), (b)). A sufficiently strong force for the dislocation to be displaced provokes a chain reaction of dislocation movement [Caillard and Bonneville, 2015], which, on the macroscopic level, leads to a sudden fracture of the material.

The knowledge of aging level is vital for industrial applications, such as for the vessel of a nuclear reactor. Irradiation leads in particular to a change in the dislocation density, the length of dislocations, existing precipitates and also the diffusion coefficients. The main macroscopic manifestation of aging under irradiation appears in the form of a shift in the temperature of ductile-brittle transition of the steel. The knowledge of the ageing behaviour after this stage is important, since if the reactor is cooled down quickly in case of emergency, it is crucial not to lower the temperature below certain value, in order to avoid cracks in the vessel, which may occur due to a rapid thermal contraction [Al Mazouzi *et al.*, 2011]. The importance in this field is even more notable, as the nuclear industry is switching from constructing new nuclear plants to strengthening the safety systems of existing reactors due to the high cost of building new power plants [Ballesteros *et al.*, 2012].

Aside from the rise in yield stress, the steel aging can be observed in the form of Lüders band or Portevin-Le Chatelier effect (PLC effect) [Portevin and

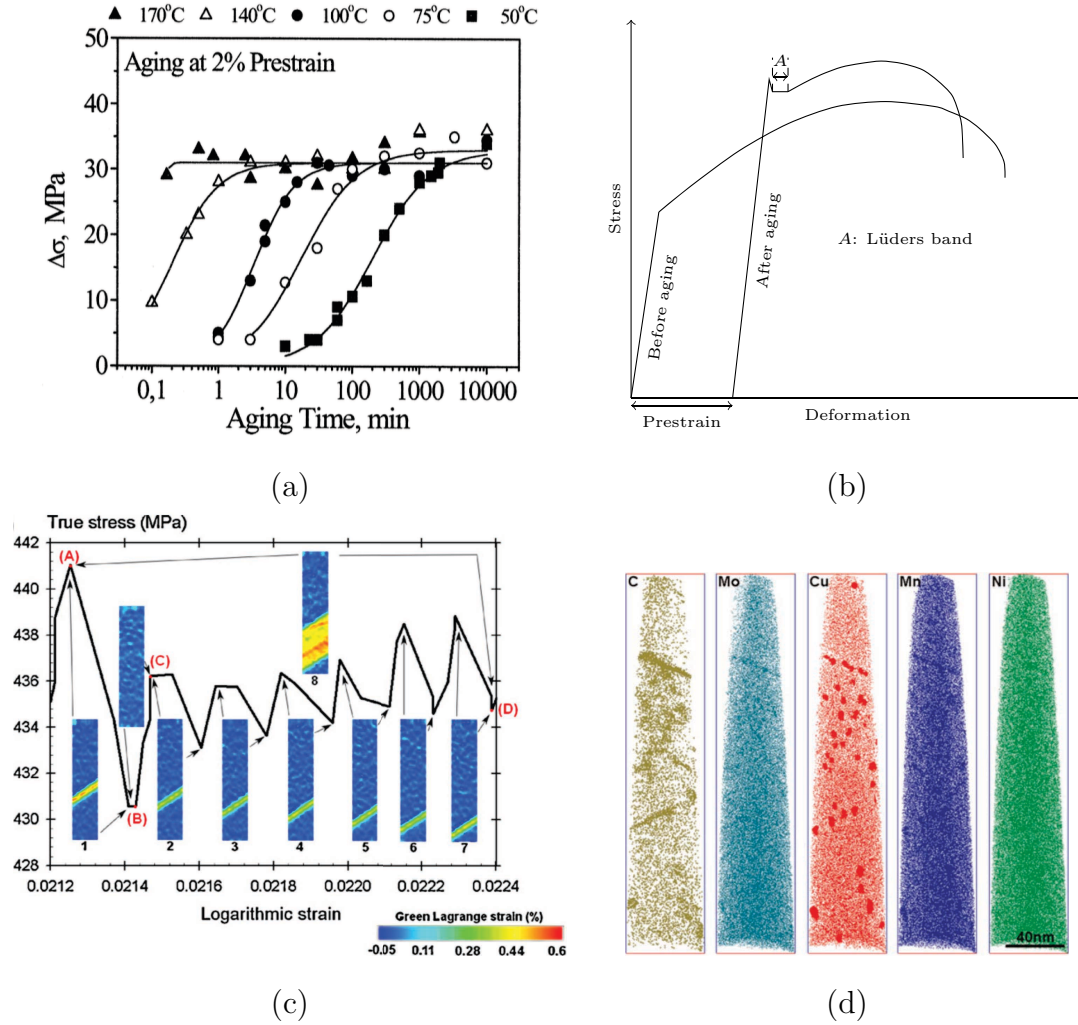


Figure 1: (a): Increase in the yield stress over the course of aging with various temperature, figure reproduced from [De *et al.*, 2000]. (b): Typical stress behavior during the tensile test before and after aging. (c) Portevin-Le Chatelier effect and deformation map showing a Lüders band, figure reproduced from [Renard *et al.*, 2010]. (d) Atom probe tomography (APT) reconstructed 3D atom distribution, figure reproduced from [Liu and Zhao, 2012].

Le Chatelier, 1923; Kubin *et al.*, 1992; Belotteau *et al.*, 2009] (*cf.* fig. 1 (b), (c)). The apparition of Lüders band is due to the dislocation piling, which occurs when the unpinning of dislocations takes place when a material undergoes a certain amount of deformation. The PLC effect can be observed when the material is deformed sufficiently slowly for the C atoms to catch up with the movement of dislocation, so that a chain of dislocation unpinnings can be observed.

The aging process of steel can be classified into several distinct phenomena, depending on timescale, solute content, and initial structure. In the case of ultra low carbon (ULC) steels, the prestraining process nucleates dislocations and releases the solute atoms into the matrix, in which C atoms are ill-placed due to the

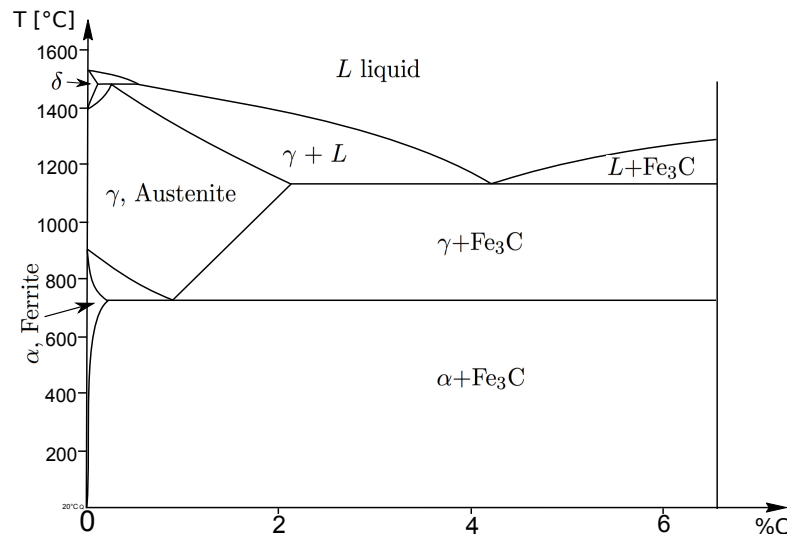


Figure 2: Fe-C phase diagram

extremely low solubility of C in bcc Fe at ambient temperature [Lindstrand, 1955] (*cf.* fig. 2). Eventually the C atoms segregate around defects and/or precipitate to form cementite (Fe_3C) [De *et al.*, 2001; Zhao *et al.*, 2000, 2001].

For a steel with higher C contents, cooling process from a high temperature would lead to a diffusionless transformation from austenite (γ -Fe), which has an fcc structure, to martensite (α' -Fe), which has a bcc structure. α' -Fe is itself a metastable supersaturated form of ferrite (*cf.* fig. 2). Whereas the α' -Fe phase can be confirmed through the X-ray diffraction pattern which is stretched in one direction [Barrett, 1943], it has also been observed that this distortion disappears for lower C concentrations [Xiao *et al.*, 1995], but the mechanism of the disappearance of the distortion has not been well clarified so far.

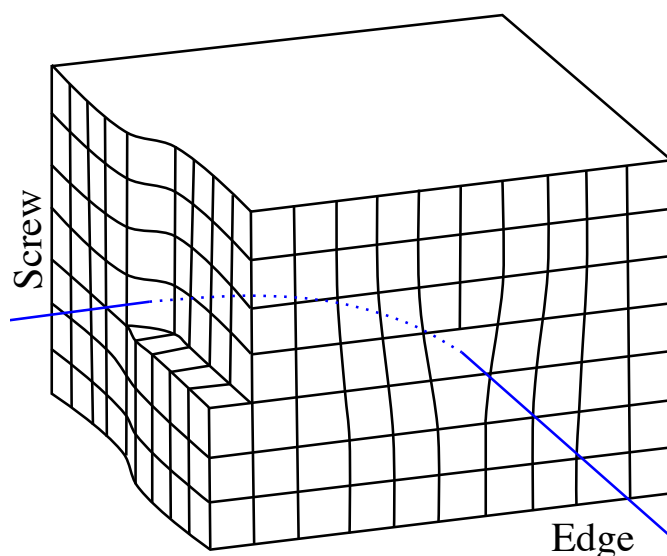


Figure 3: Schematic illustration of how an edge dislocation and a screw dislocation are interconnected. The blue line represents the dislocation line for both dislocations.

Despite the scientific and industrial importance, after decades of research, a

complete description of the structure, the formation kinetics as well as the pinning force of Cottrell atmospheres has not been well established, mainly because it requires information at the atomistic level, whereas the kinetics may attain a very large time scale. The carbon diffusion in the bcc iron crystal is characterized by interstitial jumps between octahedral sites, passing through a tetrahedral site. Eventually they arrive in a screw and an edge dislocation and are believed to stay there to fill the structural misfit of the dislocations (*cf.* fig. 3). From the experimental point of view, the segregation of C atoms has been investigated by various methods, such as spectroscopy [Kamber *et al.*, 1961], thermoelectric power [Massardier *et al.*, 2004] or atom probe tomography [Miller *et al.*, 2003]. These experiments evidenced solute atom segregation in steels (*cf.* fig. 1 (d)) and suggested the size of a Cottrell atmosphere of around 8 nm, and the time to reach saturation for a Cottrell atmosphere at room temperature is of a timescale of several months [Massardier *et al.*, 2004; De *et al.*, 2000, 1999]. Yet, at the atomic level, the distribution of carbon atoms around the dislocation core or the effect of the atmosphere on the stress field around the dislocation cannot be directly derived from these experimental results. Moreover, it is extremely difficult to take other phenomena into account, such as dislocation reorganization or precipitation during aging, which may have influenced the overall results.

From the theoretical point of view, several methods have been employed for the atomic description of the Cottrell atmospheres. Bacon *et al.* [Bacon *et al.*, 1980] described the interaction between a dislocation and a carbon atom considering the tetragonal distortion due to carbon atoms in the bcc structure as elastic dipole. Based on the interatomic potential for Fe atoms developed by Ackland *et al.* [Ackland *et al.*, 2004], Becquart *et al.* [Becquart *et al.*, 2007] developed the Raulot-Becquart interatomic potential (RB-potential) using the empirical embedded atom method (EAM). The RB-potential was created specifically to model the force exerted on a C atom in an octahedral and a tetrahedral interstitial site of the bcc-Fe matrix. Clouet *et al.* [Clouet *et al.*, 2008] compared the binding energies produced by the RB-potential and those calculated through the anisotropic elasticity theory and demonstrated their compatibility. Similarly, Clouet *et al.* [Clouet *et al.*, 2009] showed that the anisotropic elasticity theory developed by Hirth and Lothe [Hirth and Lothe, 1968] well corresponded to the Density Functional Theory (DFT) calculation, demonstrating an agreement between DFT, the anisotropic elasticity theory and the RB-potential. Hanlumuang *et al.* [Hanlumuang *et al.*, 2010] also employed the elasticity theory and the DFT method to show that the chemical and magnetic effects beyond the elastic coefficients do not play an important role in the dislocation-carbon interaction. Even though these results do

not give a concrete structure of the Cottrell atmospheres, they indicate that the atmosphere formation can well be described via elastic effects and therefore using the RB-potential.

Since aging is a process that may require a time range of up to years and cannot be treated by conventional methods such as MD, the kinetic aspect of the atmosphere formation has been mostly studied via diffusion equation, Atomistic Kinetic Monte Carlo (AKMC) or combination of both [Zhao *et al.*, 2000; Soenen *et al.*, 2004; Veiga *et al.*, 2011]. In contrast to the diffusion equation, which does not take angular variation around the dislocation line into account, AKMC would allow a more precise description. However, it requires the knowledge of activation energy for each interstitial jump, which usually requires a lengthy Molecular Static (MS) simulation. Veiga *et al.* [Veiga *et al.*, 2010] utilized the Climbing Image Nudged Elastic Band (CI-NEB) method [Henkelman and Jónsson, 2000; Barkema and Mousseau, 1996] to calculate the activation energies between octahedral interstitial sites and performed an AKMC simulation for one carbon atom. It was shown in particular that the stress field of the edge dislocation introduces a bias in the diffusion of a single carbon atom close to the line defect. However, as the activation energies were calculated in a simulation box without taking C-C interactions into account, it did not give an insight into the evolution of Cottrell atmospheres. At the same time, since their CI-NEB method requires a lengthy MS calculation, it is not realistic to extend the same framework to a simulation containing more than one carbon atom. A possibility to overcome this problem arose as the Linear Combination of Stress States (LinCoSS) method [Tchitchekova *et al.*, 2014] was developed, in which the activation energies are calculated from the local stress field around the carbon atoms, which can be obtained rapidly. However, this has not been implemented yet. Ventelon *et al.* have recently found by performing first principles calculations that carbon segregation induces the reconstruction of the screw dislocation core [Ventelon *et al.*, 2015]. Furthermore, the effect of Cottrell atmospheres on the mobility of a screw dislocation in low carbon Fe-C alloys has been investigated using Molecular Dynamics (MD) simulations, with the atmospheres being built via on-lattice Metropolis Monte Carlo (MMC) [Veiga *et al.*, 2015]. This result showed that the segregation of a few C atoms in the dislocation core causes a strong pinning force. MD simulations performed by Khater *et al.* have shown the role of carbon in solid solution (*i.e.*, randomly distributed in the simulation box) on the glide of an edge dislocation in bcc iron [Khater *et al.*, 2014]. Even though these results indicate high binding energy and therefore stability of C atoms in the Cottrell atmospheres around screw and edge dislocations due to stress, there has never been a thorough investigation

of atmosphere formation kinetics and atmosphere structure that involved a high number of C atoms simultaneously.

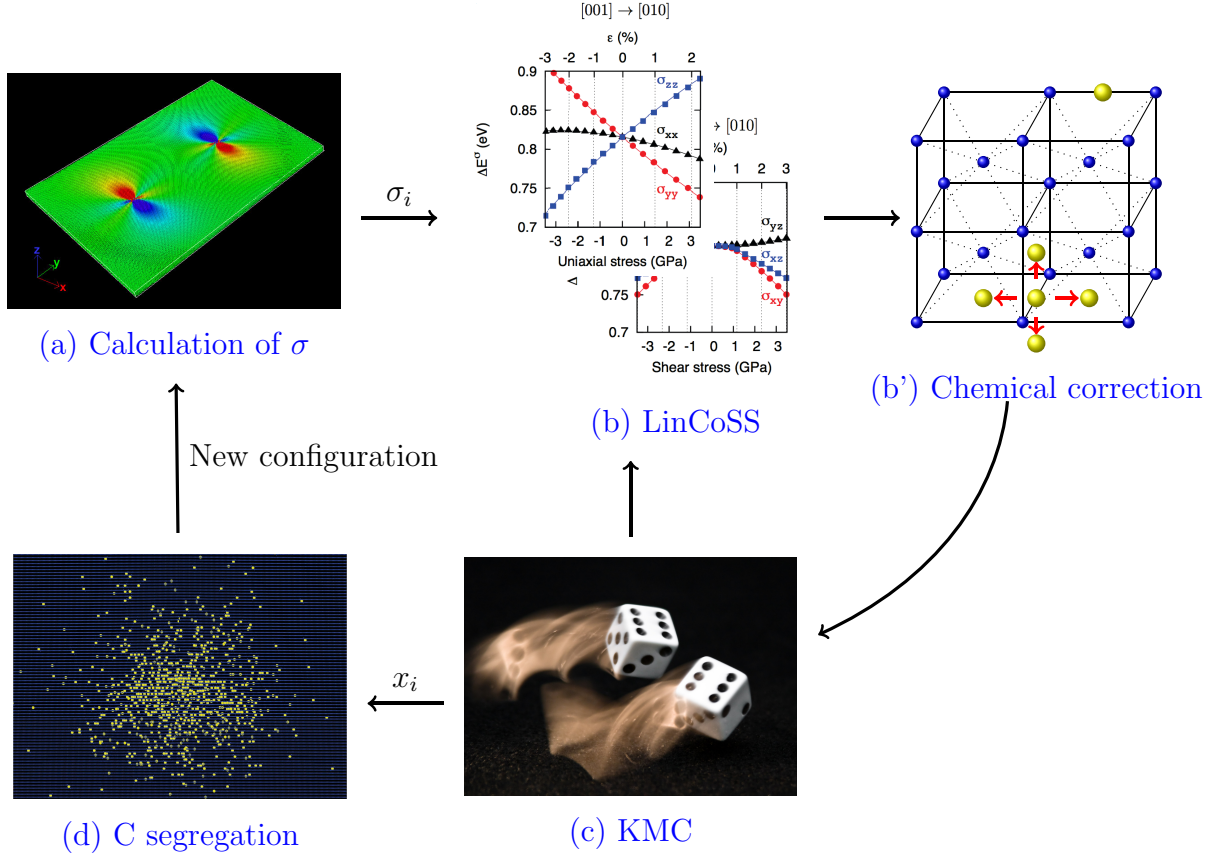


Figure 4: AKMC scheme. From the stress field calculated by LAMMPS (a), the activation energies are calculated by LinCoSS (b) and depending on whether there are neighboring atoms or not, chemical corrections are added (b'). These activation energies are incorporated into AKMC to displace C atoms. Over the course of the Cottrell atmosphere formation, the dislocation core is changed to the one that is prepared beforehand by MMC (d).

The main goal of this thesis is to understand the formation structure and kinetics of Cottrell atmospheres around edge and screw dislocations combining AKMC, MMC and other methods (*cf.* fig. 4 for the full on-the-fly scheme). Using the algorithm that is developed to create the Cottrell atmospheres, also a special case of Fe-C phase, namely α' -Fe is investigated. Furthermore, the same MMC technique is employed for the study of thermal stability of nanocrystalline Ni, in which solute atoms are inserted. For this, the chapters are constructed as follows:

1. In the first chapter, the computational methods, namely MD, Energy minimization methods, MMC, AKMC, CI-NEB, LinCoSS and the interatomic

potential for Fe-C that were developed previously and used in this work are presented.

2. In the second chapter, thermal stability of α' -Fe is investigated through MD, MMC and thermodynamic calculation over a large temperature range and various C contents in a bulk. These different methods are compared to explain the effects of many-body interactions on the thermodynamical quantities.
3. In the third chapter, MMC is used to build C Cottrell atmospheres around edge and screw dislocations for various C contents. The techniques employed to accelerate MMC are also presented. The structure of Cottrell atmospheres and the evolution of stress field are studied. Also the ordering state of C around dislocations is studied.
4. In the fourth chapter, the formation kinetics of Cottrell atmospheres around edge and screw dislocations is studied via AKMC. The technique to calculate activation energies, LinCoSS, is further developed from the original form to be adapted for the problem.
5. Fifth chapter: As an application of the methods developed for this work, grain boundary segregation of alloying atoms in the nanocrystalline Ni and the stability of grains is studied via MMC and MD. Since the thematics are entirely different from the other chapters, a separate introduction is given for this topic.

Chapter 1

Simulation methodology

Abstract

In this chapter, simulation methods employed in the subsequent chapters, namely Molecular Dynamics, Molecular Statics, Metropolis Monte Carlo, Kinetic Monte Carlo and LinCoSS are explained. It is focused on the methodology that was developed prior to this thesis.

1.1 Molecular Dynamics

Molecular Dynamics (MD) is a method based on the Newtonian mechanics that gives the dynamics of a system of particles. In classical mechanics, the Hamiltonian H of a system containing N interacting particles is given by

$$H(\{\vec{r}_i, \vec{p}_i\}) = \sum_{i=1}^N \frac{|\vec{p}_i|^2}{2m_i} + U(\vec{r}_1, \dots, \vec{r}_N) \quad (1.1)$$

where \vec{r}_i, \vec{p}_i are the particle positions and momentum, m_i their mass and $U(\vec{r}_1, \dots, \vec{r}_N)$ the interatomic potential. The classical equations of motion are derived from the Hamiltonian $H(\{\vec{r}_i, \vec{p}_i\})$:

$$\frac{d\vec{r}_i}{dt} = \frac{\partial H}{\partial \vec{p}_i} \quad (1.2)$$

$$\frac{d\vec{p}_i}{dt} = - \frac{\partial H}{\partial \vec{r}_i} \quad (1.3)$$

Eqs. (1.1), (1.2) and (1.3) lead to the equations of motion:

$$m_i \frac{d^2 \vec{r}_i}{dt^2} = -\vec{\nabla}_i U(\vec{r}_1, \dots, \vec{r}_N) \quad (1.4)$$

Provided that the interatomic potential $U(\vec{r}_1, \dots, \vec{r}_N)$ (*cf.* sec. 1.5) and the initial state $\{\vec{r}_i(t=0), \vec{p}_i(t=0)\}$ are known, the trajectory of each particle can be fully described by integrating eq. (1.4). Since the analytical solution of this equation cannot be found in general (known as n -body problem), it is solved numerically using the Verlet algorithm [Verlet, 1967].

Verlet Algorithm

In this algorithm, the position \vec{r}_i of the particle i at the time point $t + \Delta t$ is calculated through:

$$\vec{r}_i(t + \Delta t) = 2\vec{r}_i(t) - \vec{r}_i(t - \Delta t) - \frac{1}{m} \vec{\nabla}_i U(\vec{r}_1, \dots, \vec{r}_N) \frac{\Delta t^2}{2} \quad (1.5)$$

This calculation is performed iteratively. The time discretization is typically of the order of fs. It was confirmed that with $\Delta t = 0.5$ fs, the potential energy under NVE condition stayed constant in time for the Fe-C systems treated in the following chapters. The velocity of the particle i is calculated through

$$\vec{v}_i(t) = \frac{\vec{r}_i(t + \Delta t) - \vec{r}_i(t - \Delta t)}{2\Delta t} \quad (1.6)$$

In contrast to the Euler algorithm, in which the position is obtained from the velocity and the velocity is obtained from the acceleration, the Verlet algorithm allows to obtain the position directly from the acceleration. This makes the error related to the time discretization smaller.

1.2 Energy minimization

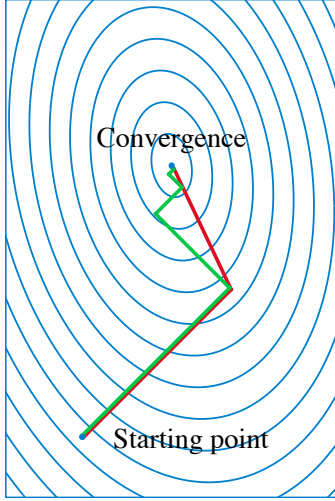


Figure 1.1: Illustration of the conjugate gradient method converging towards a minimum. The blue lines symbolizes the energy landscape. The red line is the trajectory of the system going from a higher energy state to the local minimum. The algorithm would follow the green line if the second term in eq. (1.9) is absent.

Molecular Statics (MS) is a simulation technique that gives a force free state of a given arrangement of atoms by displacing them to minimize the forces exerted on them. This corresponds to the state at the temperature of 0 K. Therefore, in contrast to MD, MS does not have a notion of time. The energy minimization is mainly performed by the Conjugate Gradient (CG) technique (*cf.* fig. 1.1). From a given position $\vec{r}_{i,0}$ and a direction vector $\vec{x}_{i,0}$ of arbitrary values, the position of atom i is updated iteratively by:

$$\vec{r}_{i,n+1} = \vec{r}_{i,n} - \alpha_n \vec{x}_{i,n} \quad (1.7)$$

The step size α_n and the direction vector $\vec{x}_{i,n}$ are calculated at each iteration following the line search procedure:

$$\alpha_n = \min_{\alpha} [U(\vec{r}_{1,n} - \alpha \vec{\nabla}_1 U(\vec{r}_{1,n}, \dots, \vec{r}_{N,n}), \dots, \vec{r}_{N,n} - \alpha \vec{\nabla}_N U(\vec{r}_{1,n}, \dots, \vec{r}_{N,n}))] \quad (1.8)$$

$$\vec{x}_{i,n+1} = \alpha_n \vec{\nabla}_i U(\vec{r}_{1,n+1}, \dots, \vec{r}_{N,n+1}) + \frac{|\vec{\nabla}_i U(\vec{r}_{1,n+1}, \dots, \vec{r}_{N,n+1})|^2}{|\vec{\nabla}_i U(\vec{r}_{1,n}, \dots, \vec{r}_{N,n})|^2} \vec{x}_{i,n} \quad (1.9)$$

This algorithm remembers the trajectory of the previous step, which is represented

by the second term in eq. (1.9). This term allows the system to avoid a twisted behavior while converging to the energy minimum (*cf.* fig. 1.1). The iteration of CG is repeated until the force exerted on any atom is below 10^{-8} eV/Å or when α_n is zero.

With CG being one method to minimize the energy of the system, the minimization method Quick-min (QM) [Sheppard *et al.*, 2008] is also utilized in the following chapters. QM is a damped dynamics method which utilizes the Euler algorithm instead of the Verlet algorithm. In the Euler algorithm, the force \vec{f}_i , the velocity \vec{v}_i and the position \vec{r}_i of the atom i is given by:

$$\vec{a}_i(t + \Delta t) = -\frac{1}{m_i} \vec{\nabla}_i U(\vec{r}_1(t), \dots, \vec{r}_N(t)) \quad (1.10)$$

$$\vec{v}_i(t + \Delta t) = \vec{v}_i(t) + \Delta t \vec{a}_i(t) \quad (1.11)$$

$$\vec{r}_i(t + \Delta t) = \vec{r}_i(t) + \Delta t \vec{v}_i(t) \quad (1.12)$$

where Δt is the same time discretization as in eq. (1.5). In this method, a standard MD simulation is launched first, and whenever the scalar product of the force $\vec{f}_i(t + \Delta t)$ and the velocity $\vec{v}_i(t + \Delta t)$ of the atom i is negative (*i.e.* $\vec{f}_i(t + \Delta t) \cdot \vec{v}_i(t + \Delta t) < 0$), eq. (1.12) is not performed and $\vec{v}_i(t + \Delta t)$ is set to zero.

As both CG and QM follow the energy gradient, it may end in a local minimum and fail to find the global minimum.

1.3 Metropolis Monte Carlo

The Metropolis Monte Carlo (MMC) is a method that gives states of a system according to the Boltzmann distribution W , which is given by:

$$W = \frac{e^{-\frac{H}{k_B T}}}{Z} \quad (1.13)$$

where k_B is the Boltzmann constant, T the temperature and Z is the partition function. Just as MS, MMC does not have a notion of time. MMC is performed iteratively, and an MMC step consists of two stochastic processes. First, from the existing state of the system o , a new state n is proposed following the probability $g(o \rightarrow n)$, where the new state does not have to be physically linked to the current

state. Second, it is decided whether the new state is accepted or rejected with the probability $A(o \rightarrow n)$. According to the detailed balance condition, each transition must be accepted with the same probability as its reverse transition at equilibrium, *i.e.* when the potential energy does not vary. Hence, the following equation must be fulfilled [Frenkel and Smit, 1996]:

$$g(o \rightarrow n)W_{\text{equilibrium}}(o) = g(n \rightarrow o)W_{\text{equilibrium}}(n) \quad (1.14)$$

which gives to the definition of the acceptance probability $A(o \rightarrow n)$:

$$A(o \rightarrow n) = \min \left\{ \frac{g(n \rightarrow o)W(n)}{g(o \rightarrow n)W(o)}, 1 \right\} \quad (1.15)$$

$$= \min \left\{ \frac{g(n \rightarrow o)}{g(o \rightarrow n)} e^{-\frac{E(n)-E(o)}{k_B T}}, 1 \right\} \quad (1.16)$$

with the potential energy E . As the proposed state (*cf.* fig. 1.2) may have an

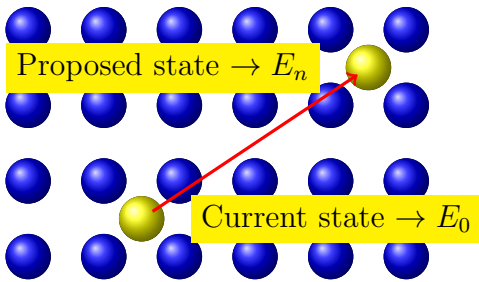


Figure 1.2: Schematic representation of a single MMC move. The spheres represent atoms and a new state is proposed for the atom represented by yellow spheres.

unrealistic arrangement of atoms in the vicinity of the displaced atom, the energy is minimized with CG before E_n is measured.

In total, the entire procedure of one MMC step can be described by the following scheme (*cf.* fig. 1.2):

1. Calculate the current potential energy E_o .
2. Propose a new state according to the probability distribution $g(o \rightarrow n)$.
3. Minimize the energy of the proposed system.
4. Calculate the potential energy of the proposed state E_n .
5. Accept or reject the proposed state according to the probability distribution $A(o \rightarrow n)$

This method is iteratively performed until the system attains the equilibrium with respect to the potential energy of the system.

1.4 Atomistic Kinetic Monte Carlo

Whereas the dynamics of a particle system can be correctly described via MD, it does not go beyond the time range of microseconds since it describes the exact position and momentum of every particle at every moment. This is particularly inefficient in the case of carbon diffusion, regarding the long dwelling time of each C atom in an interstitial site. The Atomistic Kinetic Monte Carlo (AKMC) method makes it possible to investigate the transition kinetics from one state to another, without dealing with less relevant information such as vibration of atoms, which makes this method significantly faster than MD. It is required in this method to know all the possible transition trajectories and associated transition energies, as depicted for one C atom in fig. 1.3.

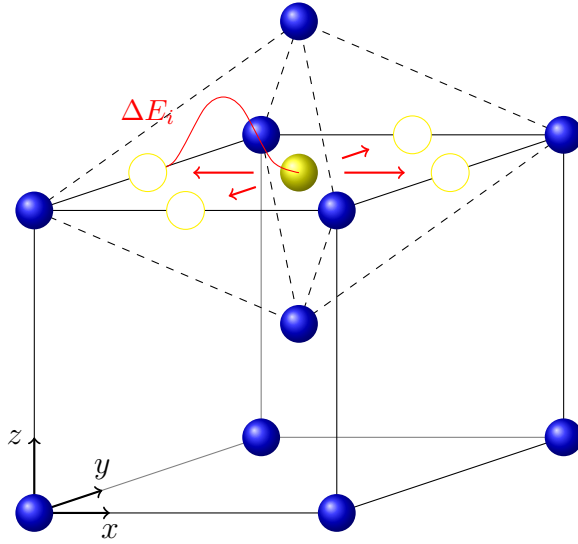


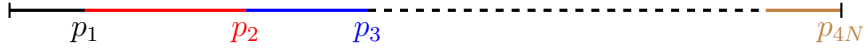
Figure 1.3: One C atom (yellow sphere) in an octahedral site in crystal bcc iron (blue spheres) and four possible transitions. For each transition there is an associated transition energy ΔE_i

Supposing that all transition trajectories and associated energies are known, the probability that the transition i takes place within a small time interval dt follows the Arrhenius law:

$$p_i dt = \kappa \exp\left(-\frac{E_i}{k_B T}\right) dt \quad (1.17)$$

where E_i is the activation energy of transition i and κ is the attempt frequency. κ is to be calculated via *ab initio* through the partition function of a C atom or from the diffusion coefficient, which can be obtained through MD or measured experimentally. In this research, it is estimated as 10^{13} s^{-1} [Voter, 2007] (*cf.* appendix C). As $p_i dt$ is the probability that the transition takes place within a time interval of dt , p_i is to be understood as transition frequency. Considering that for each octahedral interstitial site there are four neighboring octahedral interstitial sites (*cf.* fig. 1.3), there are $4N$ possible transitions for N C atoms. After cal-

culating all the transition frequencies p_1, \dots, p_{4N} , the list of these transitions is created as follows:



Then a random number ξ between 0 and $p_{\text{tot}} = \sum_{i=1}^{4N} p_i$ is taken. The transition i that satisfies the condition $\sum_{j=1}^{i-1} p_j < \xi < \sum_{j=1}^i p_j$ is effectuated. The time between two transitions is calculated via $\Delta t = p_{\text{tot}}^{-1} \ln(1/\zeta)$ with a random number $\zeta \in (0, 1)$. The whole process so far is iteratively performed, and it can be summarized as follows:

1. Calculation of transition energies
2. Creation of list of transition frequencies
3. Determination of transition to effectuate
4. Calculation of time increment

1.4.1 CI-NEB

AKMC method as described above requires the information about the trajectory of each transition along with its associated transition energy. With the Nudged Elastic Band (NEB) [Henkelman *et al.*, 2000; Henkelman and Jónsson, 2000] transition energies for a given trajectory using the MS via QM can be calculated. Historically, this method was first introduced to calculate the activation energies of hydrogen atoms on the silicon surface [Henkelman *et al.*, 2000]. It has been also employed for more complex systems such as chemical reactions that take place inside enzymes [Xie *et al.*, 2004].

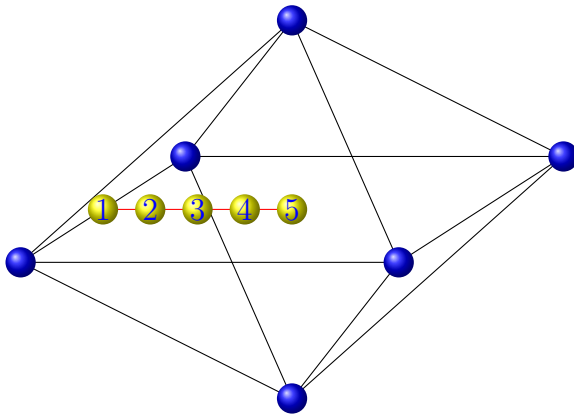


Figure 1.4: NEB with five replicas. The Fe atoms (blue spheres) are present in all replicas. Each of the C atoms is present only in each replica.

NEB looks for the trajectory which gives the path with the smallest energy barrier between two states that are known in advance. For this, a given number of simulation box replicas of the same system under investigation is created, with the first and the last replicas being the initial and the final states (*cf.* fig. 1.4). The replicas in between are created through interpolation of the initial and the final states. The simulation boxes are independent of each other, but atoms that undergo the transition are interconnected through an artificial spring force that follows the Hookes law. In the case of carbon migration, the stiffness of $K=1,000$ eV/nm² was chosen, as it gives the correct value for the activation energy for the interstitial jump in bcc iron [Tchitchekova *et al.*, 2014]. It has, however, been reported that the activation energy values do not depend on the stiffness of the spring force, as long as it stays in the same magnitude [Henkelman *et al.*, 2000]. The atoms are allowed to move only perpendicularly to the transition direction during the energy minimization.

It is, however, not very likely that the correct activation energy is found solely with NEB, as even with the additional spring force the system falls off the potential maximum, thus fails to give the correct activation energy. For this reason, the Climbing Image Nudged Elastic Band (CI-NEB) is employed. In this algorithm, the state that had the highest potential energy looks for the potential maximum by displacing the system along the given trajectory [Henkelman *et al.*, 2000].

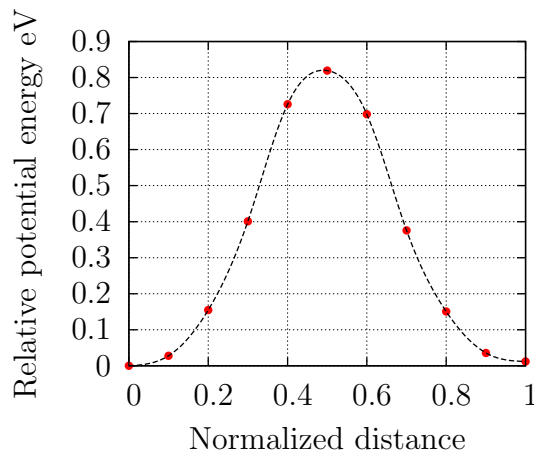


Figure 1.5: Potential energy variation of bulk bcc Fe between two octahedral interstitial sites. Relative energy is defined as the difference between the potential energy of the initial/final state and that of each replica

As an example, the activation energy of a C atom between two interstitial sites inside a stress-free bulk simulation box with CI-NEB using 11 replicas is presented in fig. 1.5. This example gives an activation energy of 0.8153 eV.

1.4.2 LinCoSS

Due to the mostly erratic movements of C atoms around a dislocation, which would require a high number of activation energy calculations, CI-NEB would be still too time-consuming to be integrated into AKMC. Considering the fact, however, that the main focus of the AKMC in this research is the diffusion of C atoms around dislocations in α -Fe, we can make following statements: 1, carbon concentration in bcc iron is relatively low; 2, attraction force of a dislocation core is governed by the elastic interaction between C atoms and the dislocation. There has been a previous work that established the relation between each component of the hydrostatic stress and the activation energy of a C atom [Garruchet and Perez, 2008]. This was extended to cover all of the stress components. This new technique, entitled LinCoSS (*Linear Combination of Stress State*), makes it possible to convert the local stress around a C atom into its activation energies, which was developed by D. Tchitchekova *et al.* [Tchitchekova *et al.*, 2014]. This section summarizes the method but a more detailed description can be found in the original paper [Tchitchekova *et al.*, 2014]. It is assumed that the activation energy variation due to the entire stress field is the same as the sum of the activation energy variation due to each stress component. In particular, this signifies for the activation energy E :

$$\begin{aligned}
 E(\sigma_{xx}, \sigma_{yy}, \sigma_{zz}, \sigma_{xy}, \sigma_{yz}, \sigma_{xz}) = & E(\sigma_{xx}, 0, 0, 0, 0, 0) + E(0, \sigma_{yy}, 0, 0, 0, 0) \\
 & + E(0, 0, \sigma_{zz}, 0, 0, 0) + E(0, 0, 0, \sigma_{xy}, 0, 0) \\
 & + E(0, 0, 0, 0, \sigma_{yz}, 0) + E(0, 0, 0, 0, 0, \sigma_{xz}) \\
 & - 5E(0, 0, 0, 0, 0, 0)
 \end{aligned} \tag{1.18}$$

Supposing that the C atom is migrating from the site type z to the site type y

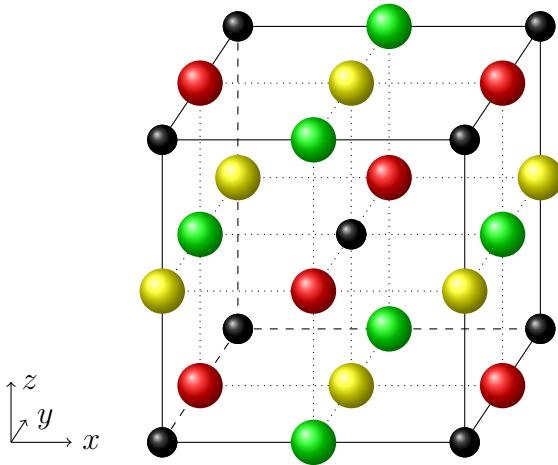


Figure 1.6: Three octahedral site types that a C atom can occupy in bcc iron (represented by black spheres). The site types x , y and z are each green, red and yellow spheres.

(cf. 1.6), the explicit equations are given by¹:

$$E(\sigma_{xx}) = a_{xx}\sigma_{xx}^2 + b_{xx}\sigma_{xx} + E_0 \quad (1.19)$$

$$E(\sigma_{yy}) = a_{yy}\sigma_{yy}^2 + b_{yy}\sigma_{yy} + E_0 \quad (1.20)$$

$$E(\sigma_{zz}) = a_{zz}\sigma_{zz}^2 + b_{zz}\sigma_{zz} + E_0 \quad (1.21)$$

$$E(\sigma_{xy}) = E_0 \quad (1.22)$$

$$E(\sigma_{xz}) = \begin{cases} a_{xz}\sigma_{xz}^2 + b_{xz}|\sigma_{xz}| + E'_0 & \text{if } |\sigma_{xz}| > 1.08 \text{ GPa} \\ a'_{xz}\sigma_{xz}^2 + E_0 & \text{otherwise.} \end{cases} \quad (1.23)$$

$$E(\sigma_{yz}) = \begin{cases} a_{yz}\sigma_{yz}^2 + b_{yz}|\sigma_{yz}| + E'_0 & \text{if } |\sigma_{yz}| > 1.08 \text{ GPa} \\ a'_{yz}\sigma_{yz}^2 + E_0 & \text{otherwise.} \end{cases} \quad (1.24)$$

with the coefficients

$$\begin{aligned} a_{xx} &= -9.0 \times 10^{-4} \text{ eV/GPa}^2 & b_{xx} &= 24.9 \times 10^{-3} \text{ eV/GPa} \\ a_{yy} &= 6.0 \times 10^{-4} \text{ eV/GPa}^2 & b_{yy} &= -24.3 \times 10^{-3} \text{ eV/GPa} \\ a_{zz} &= -8.0 \times 10^{-4} \text{ eV/GPa}^2 & b_{zz} &= -5.3 \times 10^{-3} \text{ eV/GPa} \\ a_{xz} &= -2.2 \times 10^{-3} \text{ eV/GPa}^2 & b_{xz} &= 14.5 \times 10^{-3} \text{ eV/GPa} \\ a'_{xz} &= -3.5 \times 10^{-3} \text{ eV/GPa}^2 & b_{yz} &= 15.5 \times 10^{-3} \text{ eV/GPa} \\ a_{yz} &= -3.0 \times 10^{-3} \text{ eV/GPa}^2 & E'_0 &= 0.829 \text{ eV} \\ a'_{yz} &= -1.2 \times 10^{-3} \text{ eV/GPa}^2 & E_0 &= 0.8153 \text{ eV} \end{aligned}$$

In order to calculate the activation energy from a stress state given in any coordinate system, a coordinate transformation has to be performed. As coordinate transformation is a linear mapping, a vector \vec{r} given in a coordinate system Σ can be expressed through a transformation matrix Σ with a vector \vec{r}' in a different coordinate system Σ' by $\vec{r} = S\vec{r}'$. The stress σ in the coordinate system Σ is transformed from the stress σ' in the coordinate system Σ' via $\sigma = S\sigma'S^T$. S is given by:

$$S = \begin{pmatrix} \vec{v}_0 \\ \vec{v}_1 \\ \vec{v}_2 \end{pmatrix} = \begin{pmatrix} \text{transition direction} \\ \text{site type of arrival site} \\ \text{site type of departure site} \end{pmatrix} \quad (1.25)$$

where \vec{v}_0 , \vec{v}_1 and \vec{v}_2 are normalized vectors, which are depicted in fig. 1.7 for the interstitial jump indicated. By definition, \vec{v}_0 , \vec{v}_1 and \vec{v}_2 are orthogonal to each other. Since LinCoSS is symmetric with respect to a linear mirror transformation

¹Components that are not shown are zero, *i.e.* $E(\sigma_{xx}) = E(\sigma_{xx}, 0, 0, 0, 0, 0)$

(i.e. transformation of type $x \mapsto -x$), both \vec{v}_i and $-\vec{v}_i$ ($i = 0, 1, 2$) deliver the same activation energy.

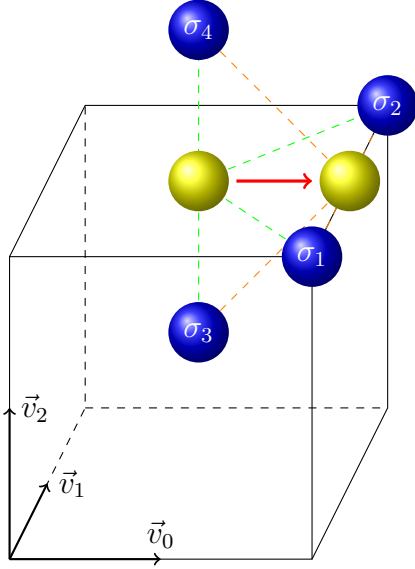


Figure 1.7: Interstitial jump of a C atom (yellow sphere). From the Fe atoms depicted (blue spheres), the stress value is calculated and the mean value is taken. \vec{v}_0 , \vec{v}_1 and \vec{v}_2 are given in eq. (1.25)

The bulk simulation box, in which LinCoSS was established, did not have stress gradient, while the stress field around dislocations does. In order to incorporate the effect of stress gradient as much as possible, for an interstitial jump, the stress is calculated from the four nearest Fe atoms from the tetrahedron (*cf.* fig. 1.7). The mean stress value is then used for LinCoSS to calculate the activation energy.

The hypothesis of the linear decomposition in eq. (1.18), however, is not valid in the region close to the dislocation line, as the stress is too high. Yet, the limit of LinCoSS was not clarified in such a way that it was not relevant to the real interstitial jumps of C atoms around a dislocation. The exact limit of LinCoSS is therefore discussed in chap. 4.

1.5 Choice of interatomic potential

As noted in the introduction, the energetics of the studied system were supplied by the empirical embedded atom method (EAM) potential. The Raulot-Becquart Fe-C EAM potential (RB-potential) [Becquart *et al.*, 2007] was built starting from the Fe potential developed by Ackland *et al.* [Ackland *et al.*, 2004], and later modified [Veiga *et al.*, 2014]. The Fe-C interactions were developed by matching of DFT results with a particular emphasis on reproducing the interaction between carbon atoms and between carbon atoms and point defects. As such, the potential has been shown to predict the octahedral site of the bcc-Fe (ferrite) lattice as the equilibrium position for carbon atoms and the tetrahedral site as the saddle point for diffusion of carbon atoms between two octahedral sites. The difference in

energy between an octahedral and tetrahedral site at 0 K and under zero applied stress is 0.815 eV/atom, which matches well with the experimentally measured activation energy for carbon diffusion [Wert, 1950; Da Silva and McLellan, 1976; McLellan and Wasz, 1993; Tibbetts, 1980; Jiang and Carter, 2003]. This potential does not contain an explicit C-C pairwise term, but it has been shown that C-C interactions are reasonably described by the many-body term compared to first principles results thanks to the embedded term [Becquart *et al.*, 2007; Sinclair *et al.*, 2010]. The potential predicts correctly that carbon atoms destabilize the usual easy core to the benefit of the hard core configuration of the screw dislocation, which is unstable in pure metals [Nguyen, 2009] in partial agreement with very recent DFT results [Clouet *et al.*, 2011]. C atoms stay in octahedral sites for low as well as for high concentrations [Veiga *et al.*, 2015]. Furthermore, it correctly gives the binding energy of a C atom near an edge dislocation [Clouet *et al.*, 2008].

This potential predicts the experimentally observed trend for tetragonality of ferrite as a function of carbon (when all carbons are located on one of the three types of octahedral sites) with the lattice parameter a varying as $a = a_0(1 + \delta_x x_c)$ and the c lattice parameter varying as $c = a_0(1 + \delta_z x_c)$, where $a_0 = 2.8553\text{\AA}$ is the lattice parameter of pure Fe for this potential, x_c is the atomic fraction of carbon, and $\delta_{x,z}$ are the distortion constants given in table 1.1. A comparison

	δ_x	δ_z	Temperature
MS/RB potential [Becquart <i>et al.</i> , 2007]	-0.088	0.56	0 K
MD/RB potential [Becquart <i>et al.</i> , 2007]	-0.1	0.6	300 K
<i>Ab initio</i> [Ventelon <i>et al.</i> , 2015]	-0.086	1.04	0 K
Experiment [Cheng <i>et al.</i> , 1988]	-0.09	0.85	300 K

Table 1.1: Comparison of δ_x and δ_z for various results.

with experimental data and a DFT calculation is presented in table 1.1. The RB potential provides an accurate description of the contraction a axis, but it underestimates the tetragonal distortion of the c axis.

As a classical EAM potential, the RB-potential does not account for the magnetic contributions to the energy of the system. This results in bcc-Fe being the stable phase from 0 K to the melting point. Disregard for the magnetic contribution to the energy of the system means that variations in physical properties of the system, such as the diffusivity of carbon, do not match experimental results at temperatures approaching the Curie temperature [McLellan and Wasz, 1993].

Chapter 2

Ordering of Carbon in Supersaturated α -Fe

Abstract

In this chapter, the thermal stability of the Zener ordering over a wide range of C contents is studied using MD, MMC and thermodynamic calculation. The atomistic simulations show that the mean field description of the Zener ordering, misses important physical quantities: firstly, through MMC it is shown that by including the direct C-C interactions, the critical temperatures are lowered. Secondly, the MD results show that due to the decline of the Young's modulus and other physical quantities, the critical temperatures rise. Within the scheme of Zener ordering, special structures are also presented.

2.1 Introduction

The richness of the simple binary Fe-C system continues to provide new opportunities for tailoring the physical, functional and mechanical properties of ferrous alloys. While the equilibrium phase diagram, pioneered by Roberts-Austen in 1897 [Roberts-Austen, 1897], is well established, our understanding of the large number of metastable phases not appearing on the phase diagram is far from well established. Metastable iron carbides find use in applications ranging from magnetic recording media [Jouanny *et al.*, 2010] to catalysts [Tau and Bennett, 1986; Zhang *et al.*, 2015]. The single largest use of metastable Fe-C phases, however, is in structural steel components. Due to its low solubility limit in Fe, C would form C-rich phases in relatively limited amount. Therefore, new routes have to be found to reach high level of supersaturation that finds application to strengthen the material [Cantergiani *et al.*, 2016]. There are a variety of examples of processes which have been argued to lead to high levels of carbon supersaturation in ferrite. Deformation processing by wire drawing, ball milling, or other severe plastic deformation processes is well known to lead to the dissolution of carbides and the formation of supersaturated ferrite [Eyre and Baxter, 1972; Moyar and Stone, 1991; Lojkowski *et al.*, 2001]. The ability to create colossal carbon supersaturation in ferrite by means of vapor deposition has been revisited [Gulino *et al.*, 2005; Castro *et al.*, 2010].

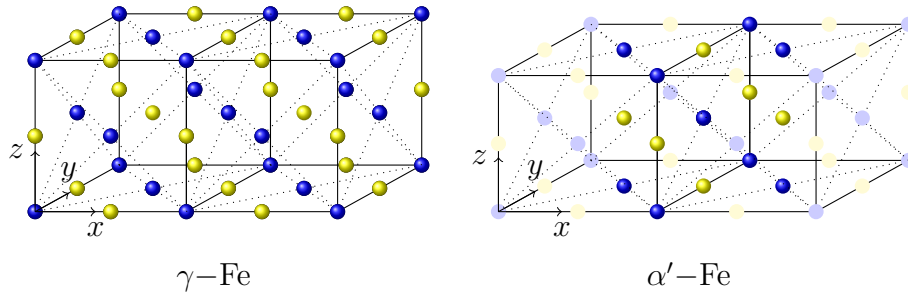


Figure 2.1: Transformation from γ -Fe (fcc) to α' -Fe (bcc). Fe: blue spheres, C: yellow spheres. This transformation leaves all the C atoms in the z -type sites. Some atoms are blurred for α' -Fe to facilitate the understanding. Except for the dilatation of α' -Fe in one direction (z -axis in this figure) and contraction in the other two directions, γ -Fe and α' -Fe are structurally equivalent.

Martensite (α' -Fe), itself a metastable supersaturated form of ferrite, is created via diffusionless transformation of austenite while quenching (*cf.* fig. 2.1). Among the three interstitial site types of ferrite (*cf.* fig. 2.2), the C atoms inside α' -Fe occupy only one interstitial site type (ordered state). The presence of an interstitial C atom leads to a tetragonal distortion of iron lattice. The deformation of the material due to this tetragonality is experimentally measured via

X-ray [Barrett, 1943]. Some investigations showed that tetragonality disappears at lower C concentrations [Xiao *et al.*, 1995], which means C atoms diffused via interstitial migrations and did not occupy the same site type anymore (disordered state). The diffusion of C atoms from martensite forms other metastable η or ϵ carbides. However, not only the composition and structure of these carbides are still a matter of some debate, but also the temperature and pressure dependence of the order-disorder transition of α' -Fe has not been fully understood until today [Bauer-Grosse, 2004; Weck *et al.*, 2012; Scott *et al.*, 2011; Krauss, 1999; Faraoun *et al.*, 2006; Zhang *et al.*, 2005; Königer *et al.*, 1997; Kehoe and Kelly, 1970].

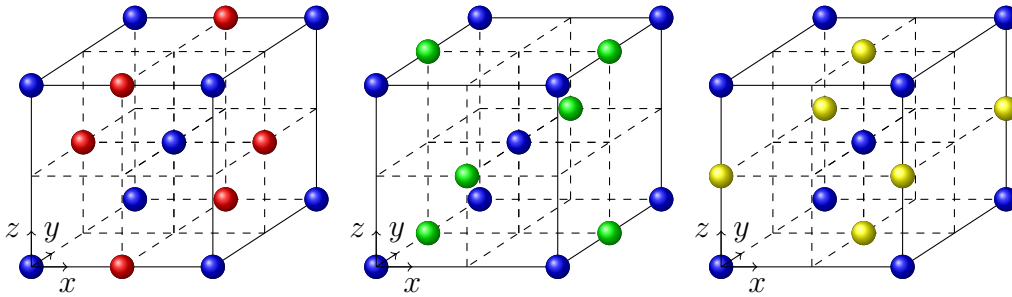


Figure 2.2: Three different site types that one C atom can occupy in different colors. In the following, the site types x , y and z refer to interstitial sites represented by red, green and yellow spheres, respectively. Fe atoms are represented in small blue spheres.

The mechanism of the order-disorder transition of α' -Fe has been first described by Zener [Zener, 1948]. In his theory, the C ordering is described via elastic strain interactions between carbon atoms. Thus, Zener's model predicts that above a critical carbon concentration and below a critical temperature, all carbon atoms tend to reside in the same octahedral site type. A more detailed treatment of this ordering was developed by Khachaturian [Khachaturian and Shatalov, 1955], as part of the so-called Microscopic Elasticity Theory (MET). In the MET treatment of interstitial ordering driven by elasticity, atomistic information in this model is encoded in the form of simplified C-C chemical interactions, which depends solely on the distance between C atoms. Udyansky *et al.* [Udyansky *et al.*, 2009] have recently re-evaluated the prediction of the order-disorder transition in supersaturated ferrite using MET parameterized via semi-empirical EAM potential for the Fe-C system. Recently, Chirkov *et al.* [Chirkov *et al.*, 2015] performed Molecular Statics (MS) and Molecular Dynamics (MD) simulations combined with thermodynamical calculation using the interatomic potential developed by Lau *et al.* [Lau *et al.*, 2007]. In this study, the MET is used, in which the potential energy variation was calculated by taking the energy difference between an ordered and a disordered state, while these states were minimized via MS. However, to create

the ordered and disordered states, the C atoms were inserted randomly into the Fe-matrix, meaning the C atoms were not distributed in a physically meaningful way.

The MET calculations, which these methods are based upon, confirmed the order-disorder transition at the critical concentration of 0.2 wt.% at room temperature proposed by Xiao *et al.* [Xiao *et al.*, 1995]. However, none of the studies took C-C interactions rigorously into consideration, whereas at high C concentration, not only the distance between C atoms, but also their arrangement with regard to the Fe atoms becomes important. This point is highlighted in the work of Ruban [Ruban, 2014], in which a hybrid method based on thermodynamical calculation and Density Functional Theory (DFT) calculation was developed in order to take chemical interactions of C atoms into account as well. The detailed description of the direct interactions between two C atoms in α -Fe of this study showed the variation of interaction energies depending on the arrangement of C atoms, demonstrating the importance of bringing the mean field description further to include direct interactions of individual C atoms. A study of the calculation of many body interaction via molecular dynamics simulations [Sinclair *et al.*, 2010] confirmed the stability of the ordered phase as a function of the C content and the temperature using the Raulot-Becquart EAM interatomic potential (RB-potential) [Becquart *et al.*, 2007], but only at 800 K and higher. This limitation was imposed by the slow diffusion of C which would require a computation time, that cannot be realized with the current computational resources.

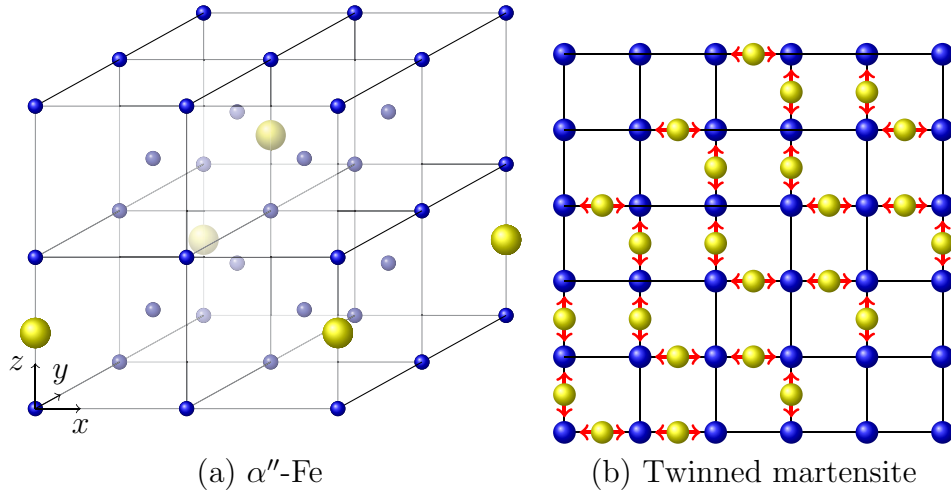


Figure 2.3: (a): Carbon arrangement inside α'' -phase (yellow spheres). Fe atoms are presented by small blue spheres. (b): An example of a twinned martensite.

Within α' -Fe, special types of ordering have also been suggested. As has been recently shown using DFT and MD/MS simulations [Sinclair *et al.*, 2010], in the

ground state, it was shown that (for high carbon supersaturation) carbon tends to prefer to reside in sites coinciding with α'' -Fe₁₆C₂ carbide, an α'' -Fe₁₆N₂-like phase, which is a completely ordered arrangement of carbon on one type of octahedral sites in a tetragonally distorted ferrite matrix (*cf.* fig. 2.3 (a)). This ordering, however, does not lead to very significant changes in the tetragonality of the system. The existence of this phase has not been beyond hypothesis [Taylor *et al.*, 1989; Van Genderen *et al.*, 1993; Zhu *et al.*, 2009; Sinclair *et al.*, 2010]. Thus, while Zener's model and MET consider two possible states (ordered and disordered) these recent results show that the details of how carbon locally orders can be important to consider as well.

Another experimental results [Lyssak and Vovk, 1965] showed a decreased tetragonal distortion in the martensite lattice of Mn steel formed on cooling austenite single crystals in liquid nitrogen. Roitburd *et al.* suggested the existence of a twinned martensite as a metastable state [Roitburd and Khachaturyan, 1970] (*cf.* fig. 2.3 (b)). This ordering pattern leads to a diagonal distortion, which is smaller than the distortion of α' -Fe having all C atoms in one site type. Kurdjumov *et al.* [Kurdjumov and Khachaturyan, 1975] demonstrated that this phase lowers the potential energy from the disordered state, but the existence of this state has not been experimentally confirmed so far.

In this chapter we present the results of our thermal stability study of Zener ordering via Metropolis Monte Carlo (MMC), MD and thermodynamic calculation in a wide range of temperatures and carbon compositions. The importance of employing different methods lies in the different thermodynamical quantities taken into account in these methods: the thermodynamical calculation is based on the minimization of the free energy where the potential energy variation is generated through the tetragonal deformation created by the C atoms in α -Fe. This effect is included in both MMC and MD, as the simulation box size is allowed to change to minimize the box pressure. Additionally, the chemical interactions are also taken into account in MMC and MD through the interatomic potential employed in this study (*cf.* sec. 1.5). Furthermore, MD takes also the temperature effects into account, which may alter certain thermodynamical quantities. The physical quantities taken into account in these methods are presented in tab. 2.1.

In all, this chapter is organized as follows: first, the simulation setup and the three different methods to investigate C ordering are explained, namely the thermodynamic calculation, MMC and MD. The disagreement of the results delivered by the three methods is explained on the basis of the difference in the physical quantities presented in tab. 2.1. Lastly, two special types of local ordering, namely the α'' -Fe₁₆C₂ phase and the martensite twinning are discussed.

	Elastic interactions	Chemical interactions	Dynamic effects
Th. calc.	✓		
MMC	✓	✓	
MD	✓	✓	✓

Table 2.1: Different physical quantities taken into account by the methods employed in this study.

2.2 Thermodynamic calculation

The order-disorder transition is characterized by the order parameter Z defined as Kurdjumov and Khachaturyan [1972]:

$$Z = \frac{3n_C^{\max}/n_C - 1}{2} \quad (2.1)$$

where n_C is the number of C atoms and $n_C^{\max} = \max\{n_C^x, n_C^y, n_C^z\}$, where n_C^x, n_C^y, n_C^z are the numbers of C atoms occupying x, y and z site types, respectively.

Z is obtained by calculating the free energy minimum:

$$F = U - TS \quad (2.2)$$

where U is the internal energy and S is the configurational entropy. The internal energy is assumed to depend on the carbon configuration exclusively via elastic interactions. It is given by:

$$U = U_0 + \frac{1}{2} V C_{ijkl} \varepsilon_{ij} \varepsilon_{kl} - \sum_{n_C} P_{ij}^{x,y,z} \varepsilon_{ij} \quad (2.3)$$

where U_0 is the energy of the system excluding elastic interactions. V is the volume of the system, C_{ijkl} is the elastic tensor, ε_{ij} is the deformation tensor and $P_{ij}^{x,y,z}$ are the dipole moment tensors accounting for the tetragonal distortion of C atoms lying in x, y and z site types. $P_{ij}^{x,y,z}$ are given by:

$$P_{ij}^x = \begin{bmatrix} \lambda & 0 & 0 \\ 0 & \lambda' & 0 \\ 0 & 0 & \lambda' \end{bmatrix} \quad P_{ij}^y = \begin{bmatrix} \lambda' & 0 & 0 \\ 0 & \lambda & 0 \\ 0 & 0 & \lambda' \end{bmatrix} \quad P_{ij}^z = \begin{bmatrix} \lambda' & 0 & 0 \\ 0 & \lambda' & 0 \\ 0 & 0 & \lambda \end{bmatrix} \quad (2.4)$$

where the tetragonal distortion constants λ and λ' account for the energy contribution of the dilatation and the contraction of a C atom, respectively. λ and λ' are obtained by inserting one C atom into a pure Fe simulation box and calculating

the potential energy increase due to the presence of this C atom.

The configurational entropy S is given as follows:

$$S = k_B \ln \left[\frac{n_{\text{Fe}}!}{n_C^x!(n_{\text{Fe}} - n_C^x)!} \frac{n_{\text{Fe}}!}{n_C^y!(n_{\text{Fe}} - n_C^y)!} \frac{n_{\text{Fe}}!}{n_C^z!(n_{\text{Fe}} - n_C^z)!} \right] \quad (2.5)$$

where n_{Fe} is the number of Fe atoms.

Assuming that x and y sites are equally populated ($n_C^x = n_C^y$) leaves only one free parameter, namely n_C^z . The free energy is therefore given by (detailed calculations in appendix):

$$F(Z, x_C, T) = F_0(x_C, T) + \lambda_0 n_C x_C \frac{Z^2}{3} - TS(Z, x_C) \quad (2.6)$$

where F_0 is a part of the free energy which is independent of Z , x_C is the atomic concentration of C and the λ_0 is the interaction parameter, which is defined as:

$$\lambda_0 = \frac{(1 + \nu)(\lambda' - \lambda)^2}{v_{at} E} \quad (2.7)$$

where ν is the Poisson coefficient, E is the Young's modulus and v_{at} is the mean atomic volume. It is remarkable to note that for the low concentration limit ($x_C \rightarrow 0$) of the governing equation (eq. (2.6)) is equivalent to the ordering equation of Khachaturyan [Khachaturyan, 1983], later re-demonstrated for the low concentration limit by Zhong *et al.* [Zhong *et al.*, 1995]. To the authors knowledge, the extension of Khachaturyan's equation to high concentrations level had never been proposed.

Physically speaking, λ_0 is a parameter that accounts for the energy difference between an ordered and a disordered state. In this thermodynamical calculation, it is computed from the elastic dilatation due to one C atom and the total energy variation is extrapolated. In appendix, we demonstrate that λ_0 can also be expressed from the internal energy of fully ordered ($U|_{n_C^z=n_C}$) and fully disordered ($U|_{n_C^z=n_C/3}$) systems via:

$$\lambda_0 = 3 \frac{U|_{n_C^z=n_C} - U|_{n_C^z=n_C/3}}{n_C x_C} \quad (2.8)$$

The free energy (*cf* eq. (2.6)) has one extremum at $Z = 0$. It is either a local or the global minimum or a maximum of the free energy. In case this is a

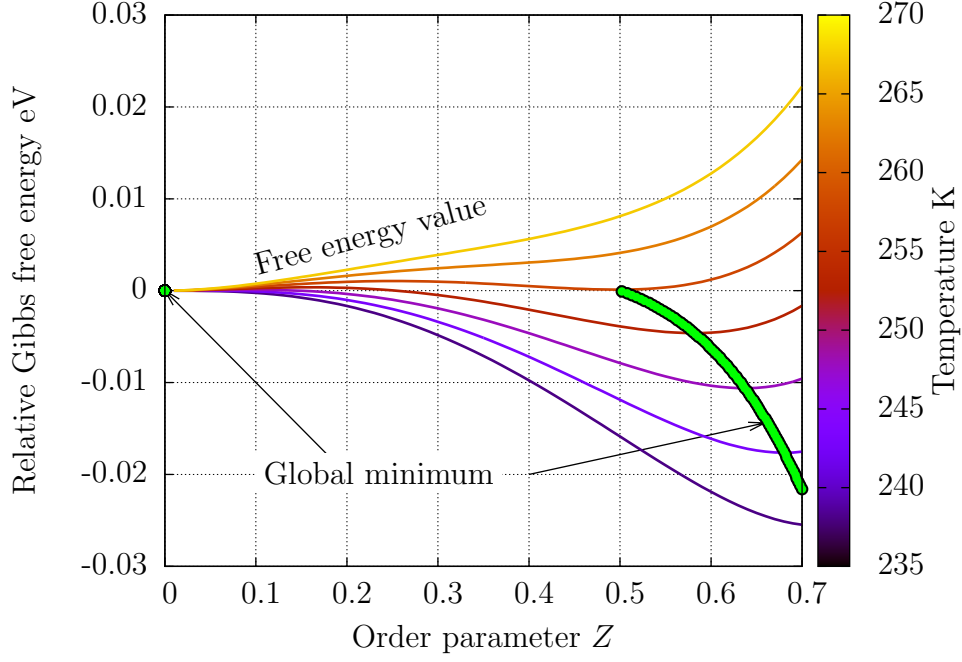


Figure 2.4: Free energy variation as a function of the order parameter for a carbon content of $x_C = 0.02$.

local minimum, there is an order parameter value $Z_{\min} \neq 0$ that gives the global minimum of the free energy F (*cf.* fig. 2.4). The critical temperature T_c , therefore, satisfies the following condition:

$$F(Z_{\min}(x_C, T_c), x_C, T_c) = F(0, x_C, T_c) \quad (2.9)$$

This thermodynamical approach provides a value of the order parameter Z for all temperatures and concentrations, as well as the critical temperature T_c . Note that the critical temperature can also be calculated thanks to MS using eq. (2.8) from the evaluation of the energy of a fully ordered and fully disordered simulation boxes.

Together with the thermodynamical calculation of this study, the critical temperatures given by three different sources are presented in fig. 2.5. The model of Zener was purely derived from the strain-induced elastic interactions of C atoms. The results of Udyansky and Chirkov both employed the MET, combined with MS calculations, for which the EAM interatomic potential was used, which was developed by Lau *et al.* [Lau *et al.*, 2007]. In the study of Udyansky, the energy was calculated from the elastic interactions and pairwise C-C interactions via MS, which depend solely on the distance between C atoms. In the study of Chirkov, the energy difference between an ordered and a disordered state was calculated via

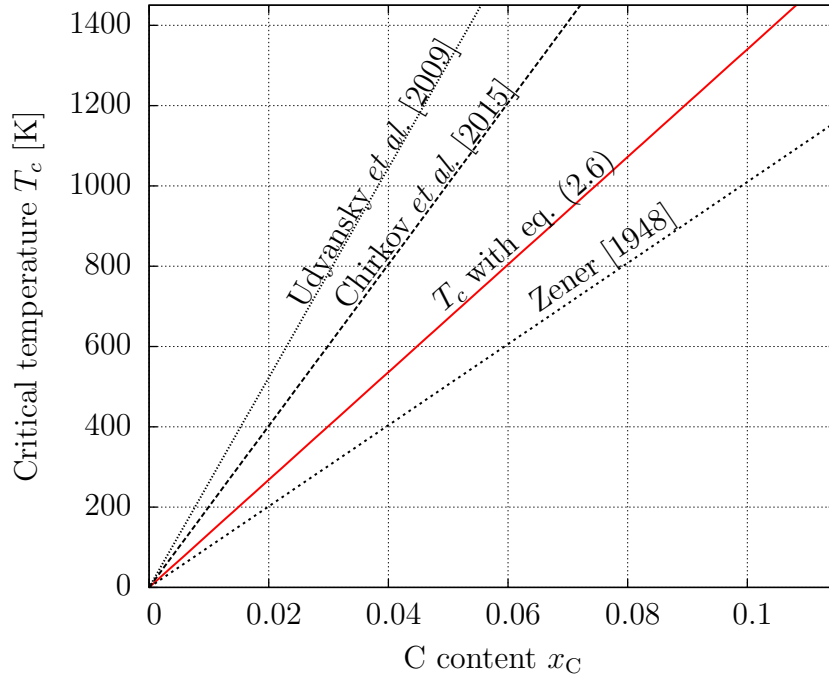


Figure 2.5: Comparison of critical temperature T_c of this study and results from the literature.

MS, although the C atoms were inserted randomly into the octahedral sites of the simulation boxes. In the studies of both Udyansky and Chirkov, the parameter λ_0 (*cf.* eq. (2.8)) was inserted into the MET model. Therefore, all three sources do not go far beyond mean field description.

2.3 Simulation Methodology

2.3.1 Metropolis Monte Carlo

Classical atomistic MMC simulations do not naturally account for elastic distortions. However, to study the order-disorder transition, governed by elastic interaction, and local atomic configurations, it is vital that both elastic and chemical interactions are accounted for. To realize this, a coupled MMC-MS approach is used here [Veiga *et al.*, 2015].

At each MMC step, one carbon atom is randomly selected and displaced to a randomly selected, unoccupied octahedral site, which does not have another C atom within a distance of one lattice parameter. Elastic relaxation is then per-

formed by MS with conjugate gradient (CG) method to avoid unphysical unrelaxed configuration. The energies (i) of the system before moving the carbon atom and, (ii) after its displacement and the subsequent relaxation of the system, are then calculated. The move of the carbon atom is directly accepted if the internal energy change of the system ΔU is negative. Otherwise it is accepted with a probability,

$$P = \exp\left(-\frac{\Delta U}{k_B T}\right) \quad (2.10)$$

It was observed that over several hundred of such exchanges, macroscopic stresses on the box did not change by more than 10-100 MPa. However, to avoid the build up of macroscopic stresses, that could couple to the elastic strain fields of the individual carbon atoms, the box is relaxed via CG to minimize diagonal pressure components. This minimization is performed each 1,000 MMC steps. In this way it is possible to maintain the macroscopic stresses on the box to below 100 MPa and to allow the box to be approximately traction free, thereby allowing the box shape to change according to the distribution of carbon atoms on octahedral sites.

Hereafter a distinction is done between MMC and controlled MMC. In the normal MMC, the site type of the proposed site is randomly chosen. In the controlled MMC, the site type of the proposed site is the same as the site type that the C atom being displaced occupies.

The MMC simulations are performed for temperature ranging from 100 K to 1400 K (every 100 K) and the C content ranging from 1 at.% to 11 at.%C (every 1 at.%).

2.3.2 Molecular Dynamics

The MD simulations are launched for temperatures ranging from 600 K to 1400 K (every 100 K) and the C content ranging from 1 at.% to 11 at.%C (every 1 at.%). Simulations are performed under the NPT conditions during 100 ns (2×10^8 time steps). Given the limited simulation duration, carbon migration cannot be observed at temperatures lower than 600 K. Note that this temperature is significantly lower than the 800 K limit of ref. [Sinclair *et al.*, 2010]. This is due to the specific initial simulation box (*cf.* sec. 2.3.3), for which only a limited number of interstitial jumps could lead to ordered or disordered states.

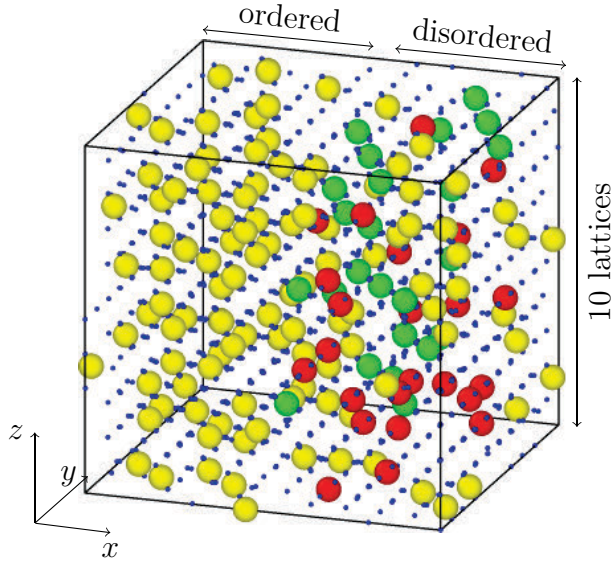


Figure 2.6: Initial configuration. Small blue spheres represent Fe atoms. C atoms are colored according to their site types (x , y and z are each yellow, green and red)

2.3.3 Simulation box

The simulation box contains 2000 Fe atoms ($10 \times 10 \times 10$ lattices) arranged on a bcc lattice. To study the order-disorder transition and to avoid the problem of time-consuming nucleation, the initial simulation box is composed of two zones: the left half of the simulation box contains C atoms located randomly on z -sites whereas the other half of the simulation box contains C atoms located randomly on x , y and z -sites (see fig. 2.6). In order to avoid unphysical configurations, two C atoms are not allowed to sit within a distance of one lattice parameter.

The energy of this system is then minimized using CG, including box size relaxation to minimize the stress (convergence is fulfilled when forces are lower than 10^{-8} eV/Å and stresses are lower than 1 MPa).

In order to relax the simulation box, *i.e.* to avoid high energy configurations of neighboring C atoms, 10,000 steps of controlled MMC are performed in advance for both MMC and MD simulations. To maintain the ordered left half and the disordered right half of the simulation box, C atoms are also forced to remain in the same half of the simulation box during MMC exchanges. This MMC minimization is performed at the same temperature as the subsequent MMC or MD simulation.

In order to calculate the parameter λ_0 with MS (*cf.* eq. 2.8), two simulation boxes containing 2000 Fe atoms are filled randomly with C atoms (following the same exclusion rules) either on z -sites exclusively (ordered configuration) or on random x , y and z -sites (disordered configuration). These boxes are then relaxed with 100,000 steps via controlled MMC.

2.3.4 Radial distribution function

For the investigation of C arrangement, the radial distribution function (RDF) $g(r)$ is employed. It is defined as:

$$g(r) = \frac{1}{r^2 \rho} \left\langle \sum_{i>j} \delta(r - |\vec{r}_i - \vec{r}_j|) \right\rangle$$

$$\approx \frac{1}{r^2 \rho} \sqrt{\frac{\mu}{\pi}} \sum_{i>j} e^{-\mu(r - |\vec{r}_i - \vec{r}_j|)^2} \quad (2.11)$$

where ρ is the C density and μ is the parameter that accounts for the resolution of the RDF. In our case $\mu = 2000 \text{ nm}^{-2}$ was chosen, which gives a smooth curve. The summation goes over all C atoms.

2.4 Results

2.4.1 Convergence of simulations

In order to get reliable results, simulations were launched four times for each set of C concentration and temperature. The calculation of the order parameter is performed by taking the average value over all the simulations, for which the “equilibration” led to a homogeneous system (for non-homogeneous systems, *cf.* subsec. 2.4.5). The order parameter Z of the MMC and MD simulations over the course of the simulations for 8 at.% are presented in fig. 2.7. At the beginning of the simulation, half of the simulation box is ordered whereas the other half is disordered, leading to the initial order parameter of $Z = 1/2$. In most cases the order parameter quickly converged towards either 0 or 1, although near the transition temperature, some fluctuations can be observed. The convergence at lower temperature is slower in MD simulations, since the interstitial migrations rarely take place at lower temperature. The convergence clearly took place before 100,000 MMC steps for the MMC simulations and 50 ns for the MD simulations. The measurement of Z is performed by taking the averages of all the results after convergence ($>100,000$ MMC steps for MMC and 50 ns for MD).

Whereas the measurement of the order parameter is performed for the same C content in fig. 2.7, the transition temperature is clearly not the same in MMC and MD. Together with the thermodynamical calculation, the next two sections are dedicated to the investigation into the origin of the difference between these calculation methods.

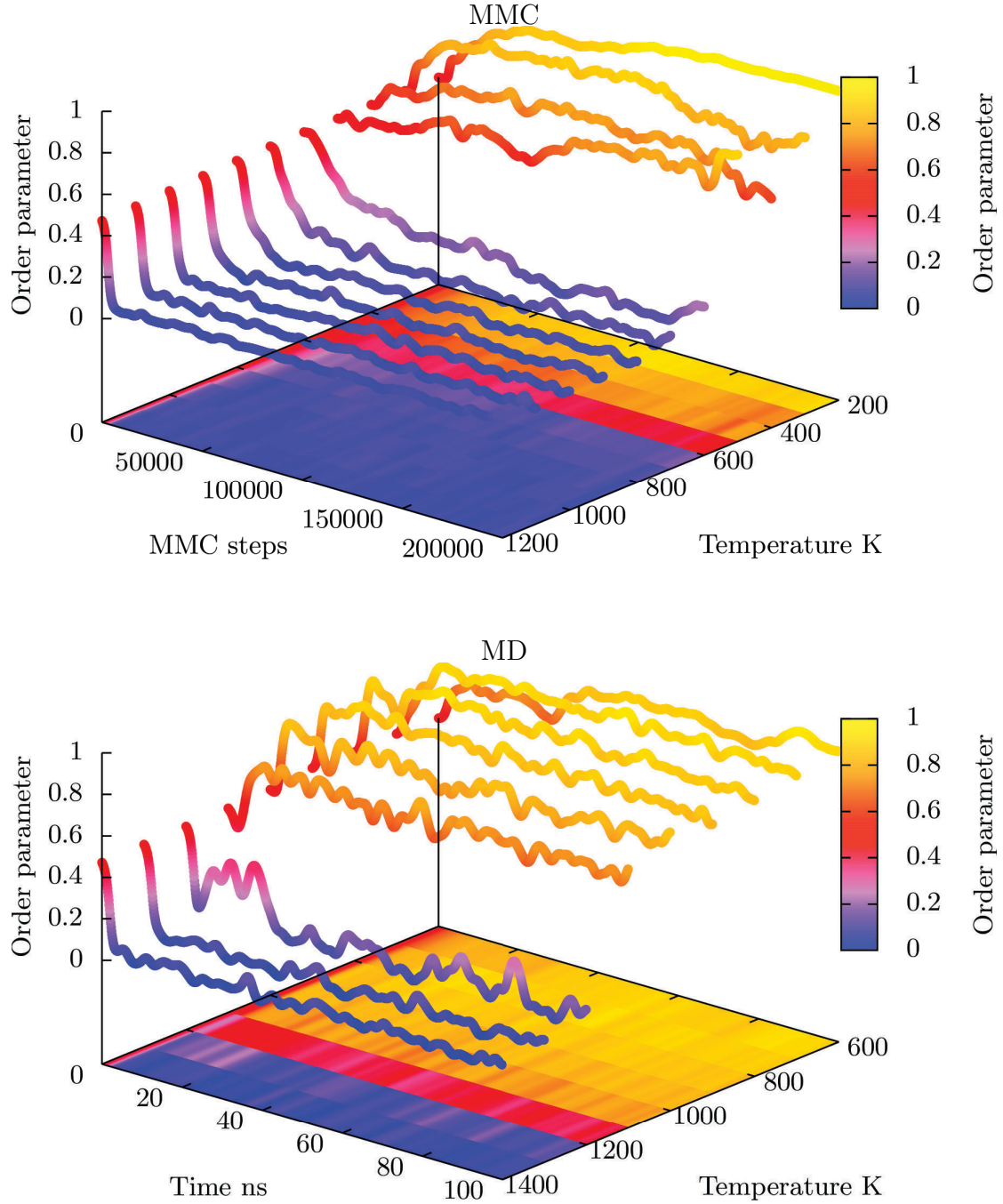


Figure 2.7: Order parameter Z of the MMC and MD simulation results as a function of the temperature with 8 at.%C.

2.4.2 Order-Disorder behaviour given by MMC and thermodynamical calculation

According to the thermodynamical calculation of eq. (2.9), the order parameter does not take any value between 0 and 0.7 (*cf.* fig. 2.8). In order to determine the critical temperature T_c from the MMC simulations, two successive temperatures T_1 and T_2 for which the order parameters fulfill $Z(T_1) > 0.5 > Z(T_2)$ are considered

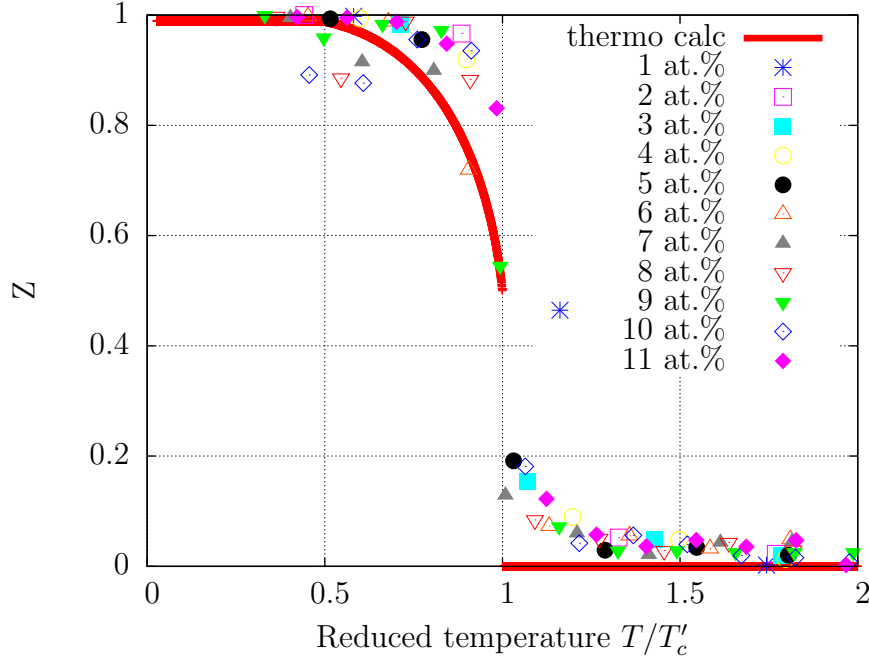


Figure 2.8: Order parameter as a function of the reduced temperature T/T_c . The thermodynamical calculation was taken for the C concentrations ranging from 1 at.% to 11 at.% and for the temperatures ranging from 50 K to 1500 K (for every 100 K).

for each C concentration value. The critical temperature T_c is then determined by interpolation, which is given by:

$$T_c = \frac{T_2 - T_1}{Z(T_1) - Z(T_2)}(Z(T_1) - 0.5) + T_1 \quad (2.12)$$

As given in eq. (2.9), the critical temperature is nearly proportional to the C concentration. Fig. 2.8 shows the order parameter as a function of the reduced temperature, that is defined as T/T_c for each C concentration. The same behaviour for both MMC and the thermodynamical calculation can be observed in the transition from lower temperature, at which the order parameter is near 1 to the critical temperature.

Fig. 2.9 compares the order parameter of MMC and the thermodynamical calculation over a wide range of C contents and temperatures. Although strong agreement for lower C concentrations can be seen, at higher C concentrations, the critical temperature predicted by the thermodynamical calculation is almost twice as high as that of MMC. In the following, the origin of the deviation is investigated.

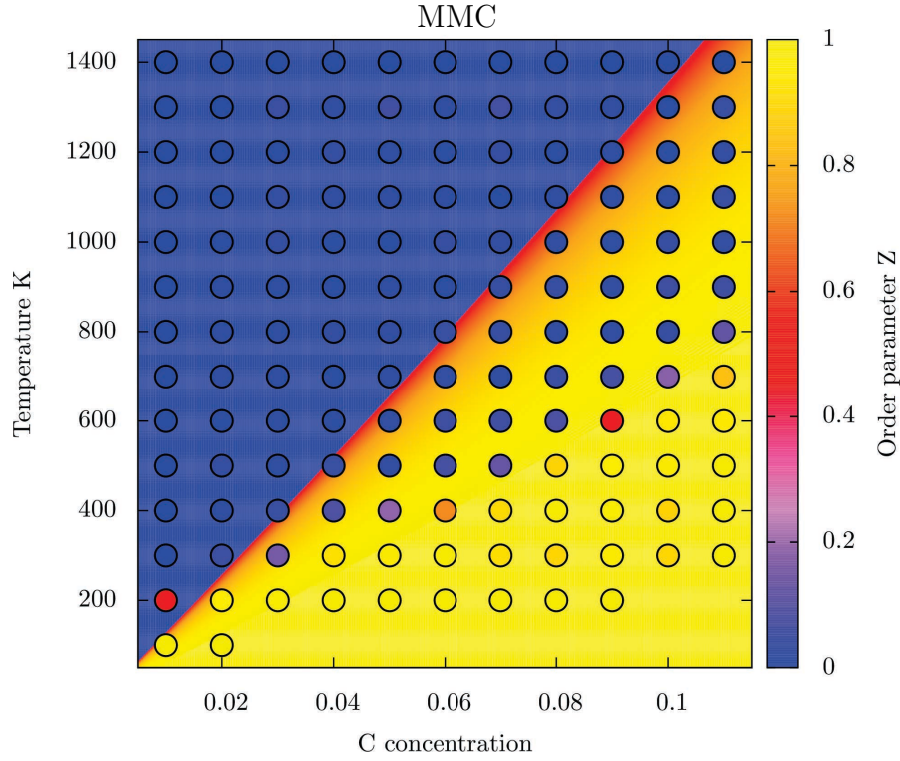


Figure 2.9: Phase diagram for showing the order-disorder transition. Circles: MMC simulation results. Background: thermodynamical calculation

Chemical interactions at high C concentrations

The parameter λ_0 , which accounts for the difference between an ordered and a disordered state, was calculated by considering the elastic distortions due to the C atoms in the thermodynamical calculation (*cf.* eqs. (2.6) and (2.7)). However, λ_0 can be directly obtained from the energy difference between an ordered and a disordered state via interatomic potential (*cf.* eq. (2.8)). λ_0 calculated in this way contains also the direct chemical C-C interactions between the C atoms, which are important at high C concentration. This λ_0 is then inserted into the thermodynamical calculation of eq. (2.9) using the same entropy part. In order to evaluate the critical temperature with the new λ_0 , ordered and disordered states are obtained through three different ways:

1. Low C limit configurations (3 C): Three C atoms are inserted into the simulation box containing only Fe atoms, while these C atoms are sufficiently far away from each other that the direct C-C interactions can be neglected. For the ordered state, the C atoms are in the same site type. For the disordered state, the C atoms occupy three different site types.
2. MD configurations: Ordered and disordered states are obtained from MD for the C contents, for which an order-disorder transition are observed depending

on the temperature. A transition in MD could be observed for 8 at.% and 9 at.%. For the ordered and disordered states, the configurations at 900 K and 1400 K are taken, respectively.

3. MMC configurations: Fully ordered and fully disordered states are created by inserting the C atoms randomly into the pure Fe box. Then a controlled MMC is performed for 10,000 MMC steps (*cf.* sec. 2.3.1 for the concept of controlled MMC).

	C-C interactions	Eq. (2.9)	MMC
3 C configurations (1)		✓	
Thermodynamical calculation		✓	
T_c with MD configurations (2)	✓	✓	
T_c with MMC configurations (3)	✓	✓	✓
MMC results	✓		✓

Table 2.2: Different methods to calculate the critical temperature T_c with respect to their relations to the direct C-C interactions, how T_c is measured (whether eq. (2.9) is used or it is calculated directly from the ordered/disordered states using eq. (2.12)) and whether MMC algorithm is employed or not. The numbers in brackets indicate the three new calculation methods mentioned above.

Tab. 2.2 shows the relation between the different methods to calculate the critical temperature T_c , how the critical temperature was obtained (whether eq. (2.9) or directly by calculating the order parameter) and whether it involved an MMC simulation, in order to take possible computational artefacts of MMC into consideration.

Fig. 2.10 compares the critical temperatures obtained with these methods. It can be clearly seen that all the methods that rigorously include the chemical interactions (T_c with MMC configurations, MMC results, T_c with MD configurations) strongly deviate from the thermodynamical calculation at higher C contents. At lower C contents, all results are consistent with each other, including the case with three C atoms.

There may be two possible factors that may explain the deviation of the MMC results from the thermodynamical calculation:

1. Physical quantities such as Young's modulus, which are considered to be constant in the thermodynamical calculation, may vary depending on the C concentration.

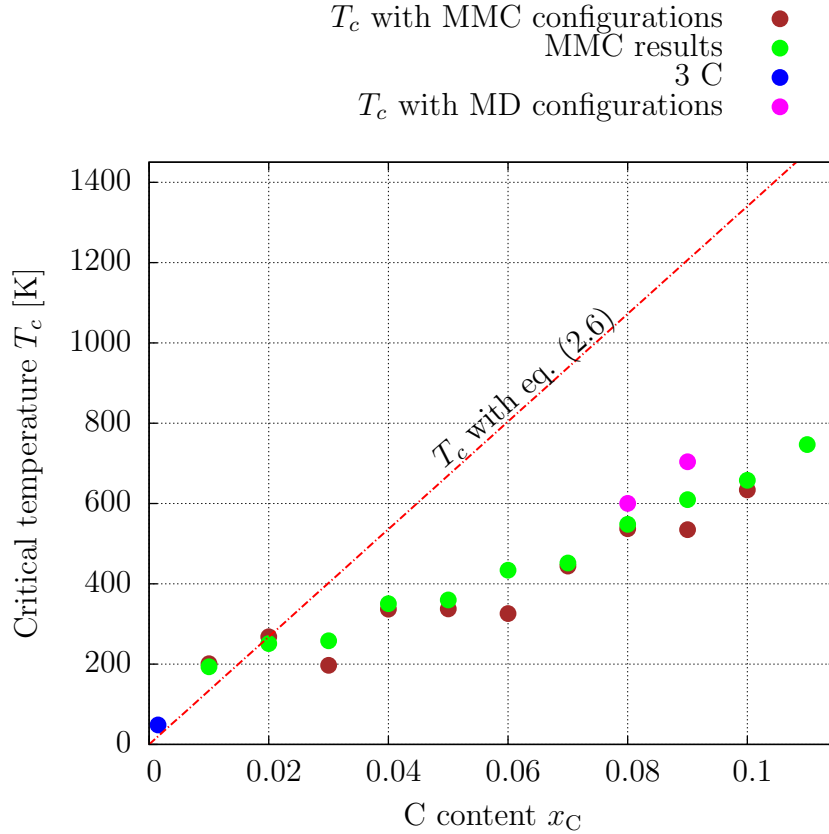


Figure 2.10: Comparison of critical temperature T_c given by MS and MMC simulations.

2. Chemical interactions between C atoms may play an important role.

Concerning the first possibility, it has been previously reported experimentally, that the C content does not play an important role in the variation of Young's modulus [Fukuhara and Sanpei, 1993], which certainly does not explain the difference of 500 K for the critical temperature for 11 at.% in fig. 2.10.

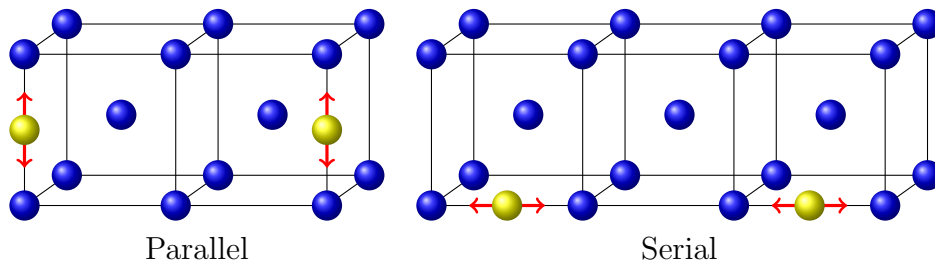


Figure 2.11: Parallel and serial configurations

In the thermodynamical calculation, only a distinction between “same site type” and “different site type” was done. However, there is an important distinction for “parallel” ordering and “serial” ordering within ordered states (*cf.* fig. 2.11). In the serial ordering, two C atoms are in the same site type and the

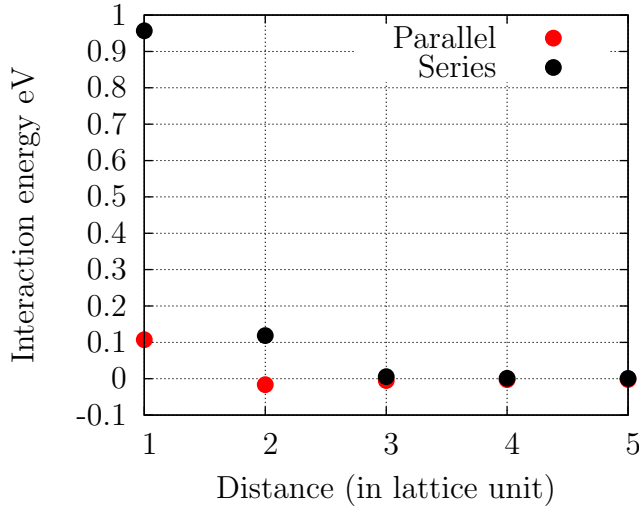


Figure 2.12: Interaction energy variation of parallel and serial configurations (*cf.* fig. 2.11) as a function of distance in lattice units. A positive value of interaction energy means repulsive interaction.

direction of expansion is the same axis as their site type. On the other hand, in the parallel ordering two atoms are in the same site type but the direction of expansion is in a different direction. It can be seen that even if the distance between two C atoms is the same, their interaction energy may be positive or negative (*cf.* fig. 2.12). Since there are two “serial” sites for each interstitial site, each C atom creates two “forbidden” sites of the same type, hence the C atoms may occupy up to three times as many interstitial sites of the same type as they would configurationally require. At high C content, therefore, it is difficult to put all the C atoms in the same site type. This may explain why the mean-field theories deviate from the MMC results for higher C concentrations, at which direct C-C interactions become important.

2.4.3 Order-disorder transition diagram of MD

The MD results deliver critical temperatures which are well higher than the MMC results (*cf.* phase diagram of fig. 2.13). This is possibly caused by the elastic constants λ , λ' and the Young’s modulus E , which are constant in MMC, since MS is performed at 0 K, although they are both expected to drop significantly at higher temperatures [Lawrence *et al.*, 2014; Fukuhara and Sanpei, 1993] (*cf.* fig. 2.14). This probably compensated the effect of C-C interactions and increased the critical temperatures overall.

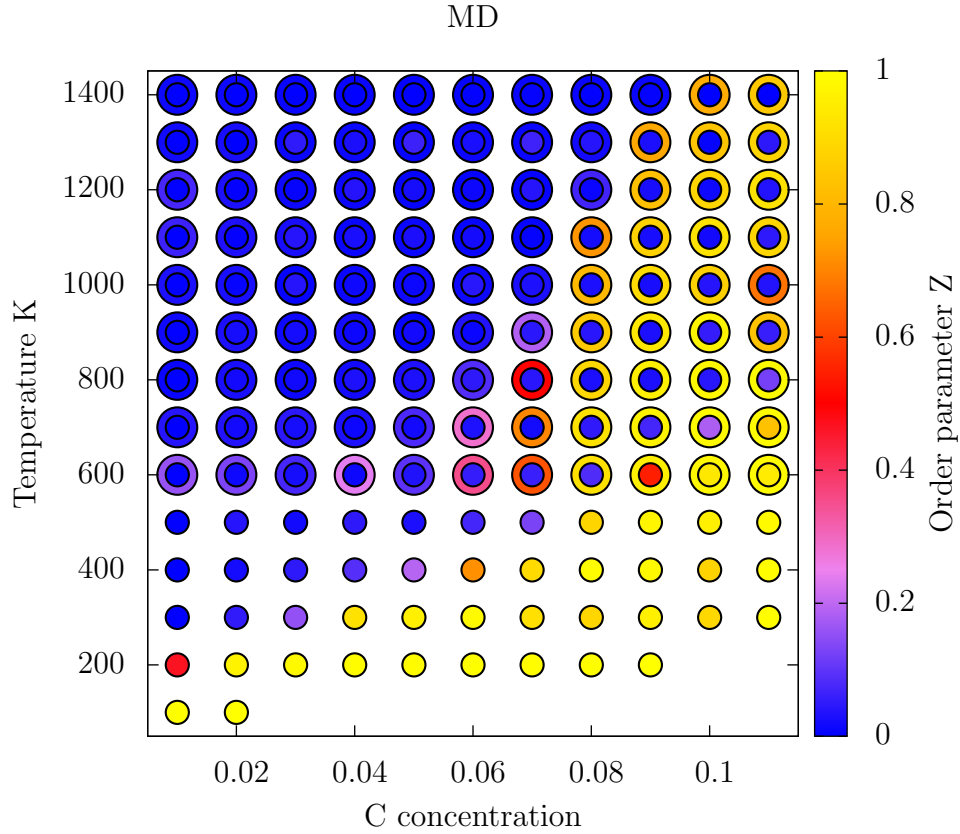


Figure 2.13: Phase diagram for showing the order-disorder transition. Large circles: MD simulation results. Small circles: MMC simulation results

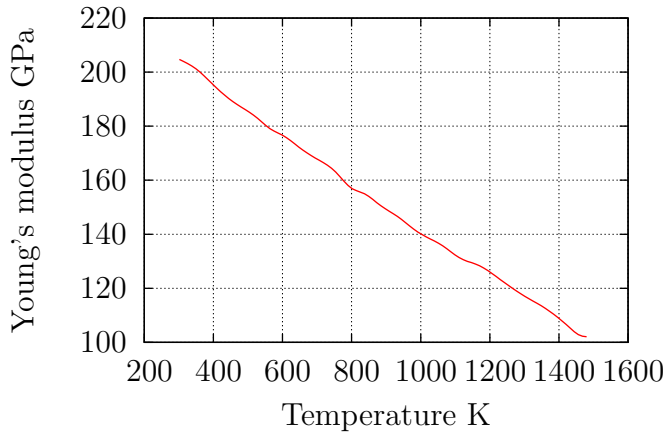


Figure 2.14: Experimental results of Fukuhara *et al.* [Fukuhara and Sanpei, 1993] on the variation of Young's modulus as a function of the temperature.

2.4.4 Interpretation of the order-disorder transition given through thermodynamical calculation, MMC and MD

The phase diagram given through the thermodynamical calculation is based on the free energy minimization, as given in eq. (2.2). For the free energy calculation, the computation of the entropy is performed by counting the number of possible configurations for a given order parameter. The energy variation is given only

through the elastic deformation of bcc iron due to the presence of C atoms. However, a comparison with the MMC results demonstrated the importance of the direct C-C interactions at higher C contents, since due to the C-C interactions the system tends to become disordered.

The variation of certain elastic constants, such as the Young's modulus E or the tetragonal distortion constants λ , λ' , is neglected in MMC, since the configurations given through MS are at 0 K. MD simulations, which take also the variation of these variables into account, gave higher transition temperatures than MMC for higher C contents, since MD takes variation of these elastic constants into account.

2.4.5 Formation of α'' -Fe and twinned martensite

For some concentrations and temperatures, particular structures of ordering have been obtained. First, some of the MMC simulations performed for 11 at.%C systems led to fully ordered α'' -Fe₁₆C₂ structure, as presented and studied in ref. [Sinclair *et al.*, 2010].

The α'' -Fe₁₆C₂ phase is structurally equivalent to the α'' -Fe₁₆N₂ phase. The base vector of C atoms is given by $(0, 0, 0.5a_0)$ and $(a_0, a_0, 1.5a_0)$ (*cf.* fig. 2.15 (a)). This implies that the C atoms are aligned diagonally in the simulation box (*cf.* fig. 2.15 (a) and (b)).

In fig. 2.15 (c) and (d), the final results of MMC simulation at 400 K and MD simulation at 600 K for the C concentration of 11 at.% are presented. In the case of the MMC simulation an α'' -Fe₁₆C₂ is formed. This property is not observed in the MD simulation, even though the C atoms are ordered. This observation is underpinned by the RDF results shown in fig. 2.16, where the lines at the bottom of the figure shows the theoretical distance of C atoms of an ordered system, where the red lines denote the distance between two C atoms in Fe₁₆C₂ configuration. The lines above the figure denote all possible maxima in a bcc iron matrix. Clearly, the peak expected for the second nearest neighbors in the Fe₁₆C₂ can be observed in the MMC simulations at lower temperatures (indicated by a red arrow in fig. 2.16), but is entirely missing in MD simulations.

Most likely, the duration of the simulation was too short for the MD simulation. Indeed, the diffusion coefficient was 4.5×10^{-6} nm²/ns at 600 K. Thus it must have been just enough for the C atoms to jump to a neighboring site within the simulation time. Once a C atom arrives in a site corresponding to the Zener ordering, it likely stayed there regardless of whether it corresponds to a site corresponding to α'' -Fe₁₆C₂ or not, as it requires at least two interstitial jumps to go from one site to another site of the same type. This problem, however, does not

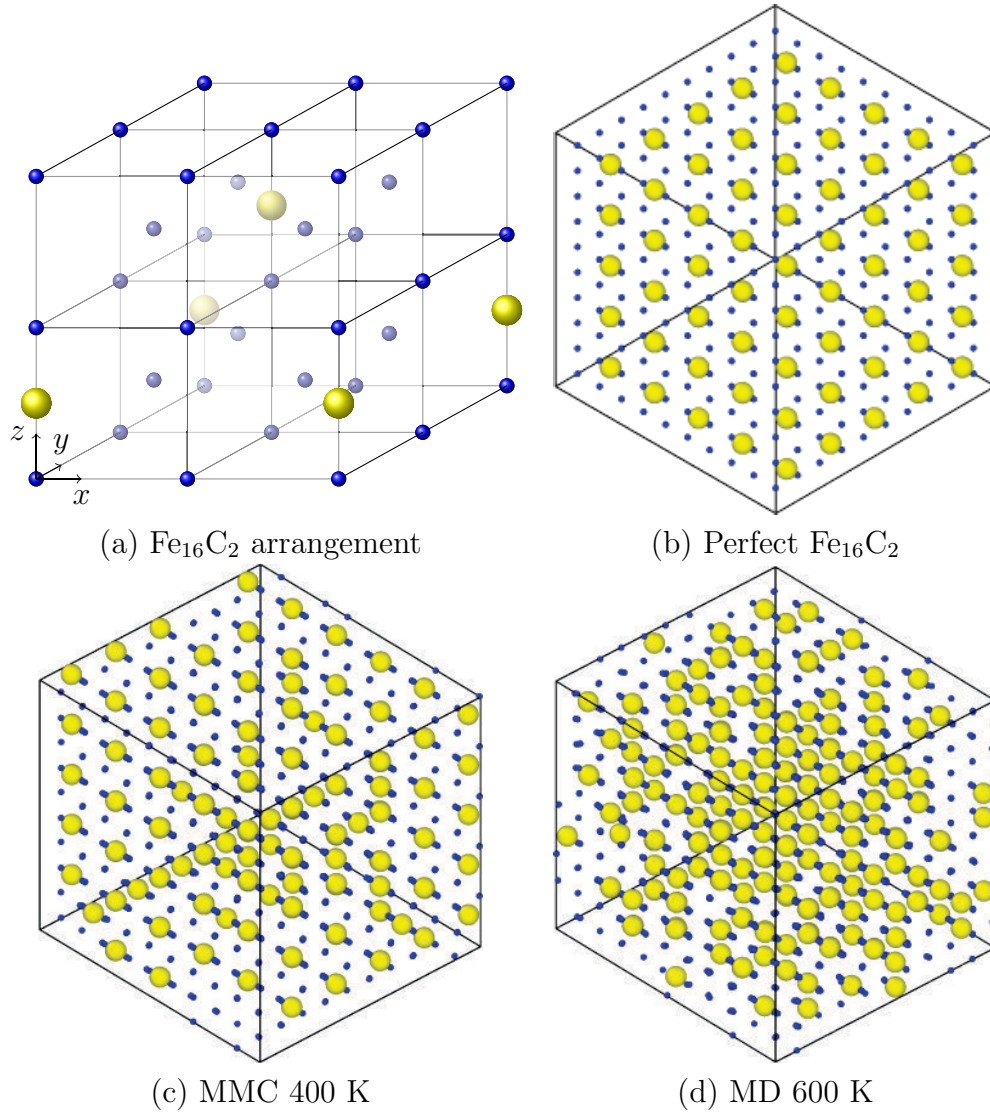


Figure 2.15: (a) Carbon arrangement of Fe_{16}C_2 (yellow spheres). (b) Perfect Fe_{16}C_2 from $[1\ 1\ 1]$ direction. Final state of (c) MMC and (d) MD simulations with 11 at.%. Blue and yellow spheres represent Fe and C atoms, respectively.

occur in MMC simulations, as the C atoms are displaced from any site to any site in the simulation box.

The twinned martensite, which was first suggested by Roitburd *et al.* [Roitburd and Khachaturyan, 1970] was also observed in some cases in both MD and MMC (*cf.* fig. 2.17). Most likely due to the limitations on computation time the simulation remained in this metastable state and did not converge to a fully ordered state. Since directions of the tetragonal distortions of the two zones are perpendicular to each other, the total deformation, which results in the diagonal direction, is smaller than in the case of homogeneously ordered state. From the technical point of view, the order parameter would also be much lower according to the definition given in eq. (2.1), which would be recognized as disordered state.

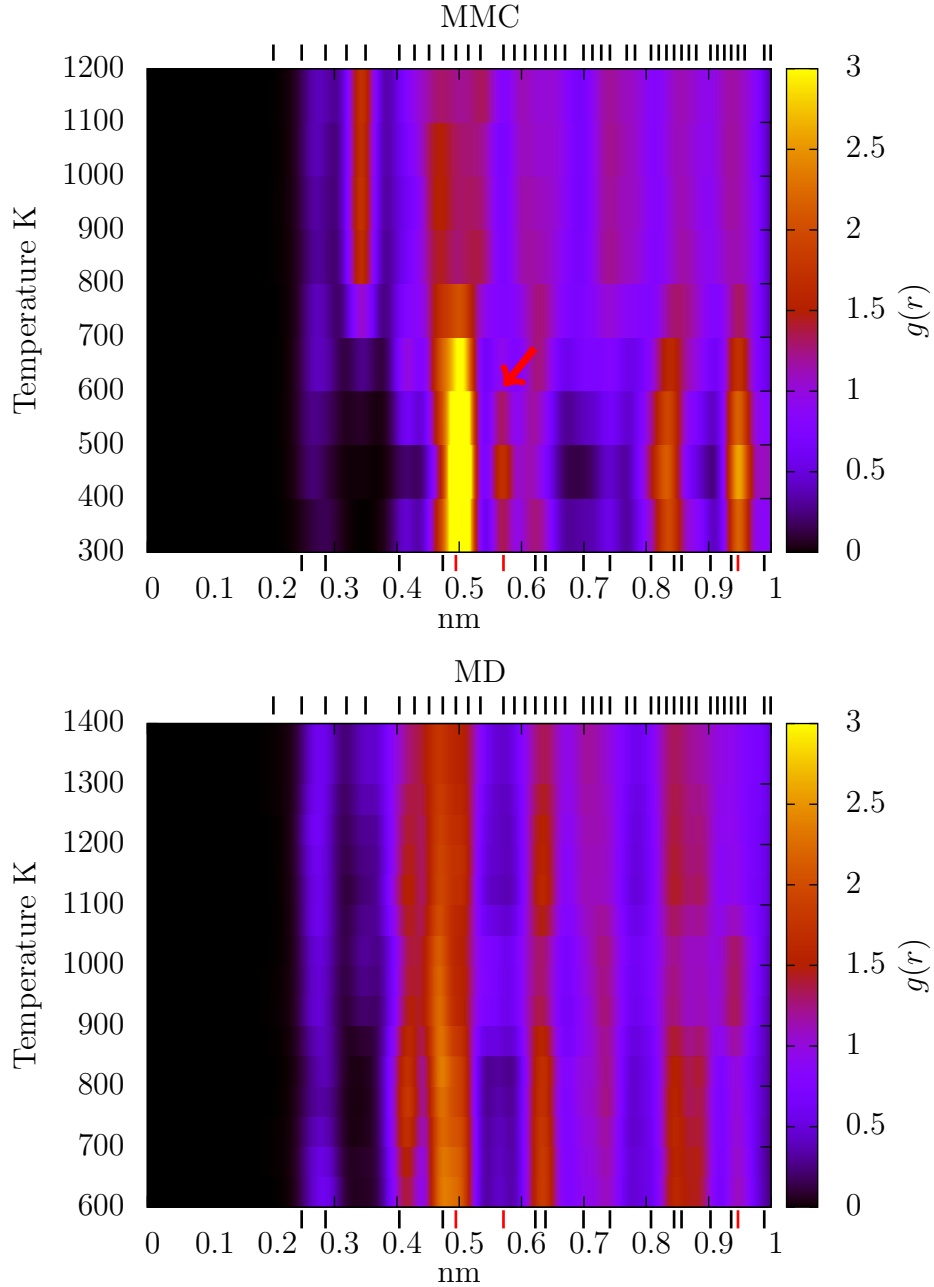


Figure 2.16: Radial distribution function for 11 at.% of MC and MD simulations. The lines below the figure show the theoretical values of all possible interstitial sites in ordered configuration, where red lines show the values for α'' -Fe, where the global distortion of the simulation box is not considered. The lines above the figure show the theoretical values of all possible interstitial sites. The red arrow in the figure for MMC indicates an Fe_{16}C_2 peak that cannot be seen in the MD result.

2.5 Conclusion

In this chapter, the thermal stability of Zener ordering was studied for large temperature and C concentration ranges via atomistic simulations and thermodynamical calculation. The atomistic simulations were performed with the MMC method

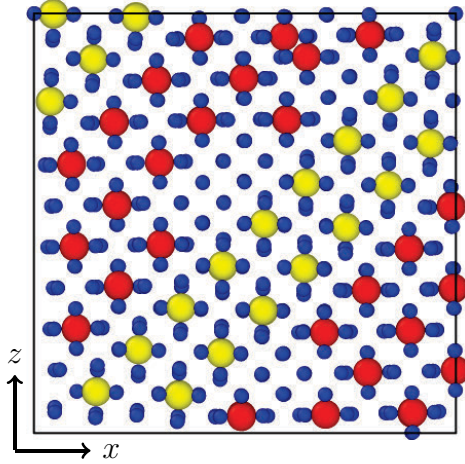


Figure 2.17: Twin ordering. Red and yellow spheres are in x and z sites, respectively. The two zones with red/yellow atoms are connected through periodic boundary conditions.

conjugated with the MS method and MD simulations. In both MMC and MD, convergence was “accelerated” thanks to an initial configuration, where half of the simulation box was already ordered, while the other half was disordered. Using the order parameter, a phase diagram for each method was obtained. Even though at low C concentration the MMC results and the thermodynamical calculation were in a good agreement, at higher C contents, the critical temperatures predicted by MMC were lower than those predicted by the thermodynamical calculation. After performing several independent simulations with different techniques, it was found that it was due to the direct chemical interactions between C atoms that the critical temperatures were lower in MMC than in the thermodynamical calculation.

Yet, the MD simulation results showed critical temperatures at higher C contents which were significantly higher than in MMC. This is probably due to the elastic constants and the Young’s modulus, which are predicted to decline when the temperature or the C content increase, thus preferring ordered states. The exact measurement of the dependence of these variables on the temperature can be performed using MD, which is an important perspective of this study.

In conclusion, the investigation of this chapter showed the importance of chemical interactions between C atoms and the variation of certain thermodynamical quantities such as Young’s modulus due to the temperature difference, all of which have so far been neglected in the theoretical calculations of the stability of the Zener ordering in the previous studies.

The α'' -Fe₁₆C₂ phase, which is structurally equivalent to α'' -Fe₁₆N₂, was observed only in MMC simulations. The difference between MMC and MD is most likely explained by the insufficient calculation time for the MD simulations as the diffusion coefficients were not high enough to allow for interstitial migrations between two sites of the same type, since once a Zener-ordering realized, such a migration would require to pass through an energetically unfavorable interstitial

site.

In some of the simulations, a twinned martensite was observed, which leads to a diagonal distortion of the simulation box. The existence of this state was suggested in a previous study [Kurdjumov and Khachaturyan, 1975], and it is known to be a metastable state. In our study, the simulations were presumably not long enough to converge to a fully ordered state, which was the reason why the simulations ended up in a twinned martensite.

Chapter 3

Formation of carbon Cottrell atmospheres in bcc iron and their effect on the stress field around edge and screw dislocations

Abstract

Biased Metropolis Monte Carlo is employed to build carbon Cottrell atmosphere around an edge dislocation. A novel method involving only local minimisation during the Metropolis scheme allows to deal with a million-atom system within a reasonable computation time. In this study, it is discovered that (i) the carbon atoms occupy interstitial sites not only in the traction zone, but also in the compression zone; (ii) local carbon concentrations of approximately 8 at.% are in good agreement with experimental values; (iii) the saturation of the Cottrell atmosphere does not originate from the stress field around the atmosphere but from repulsive carbon-carbon interactions only.

3.1 Introduction

Over the course of many years, various attempts to probe Cottrell atmospheres have been carried out. Experimental techniques such as spectroscopy [Kamber *et al.*, 1961], thermoelectric power [Massardier *et al.*, 2004] and atomic tomography [Miller *et al.*, 2003; Wilde *et al.*, 2000] witnessed to the carbon segregation in bcc iron, its extent and the rate of atmosphere saturation as a function of the temperature. However, at the atomic level, the distribution of carbon atoms around the dislocation core or the effect of the atmosphere on the stress field around the dislocation cannot be directly derived from these experimental techniques. On the one hand, these experiments suggest that the size of the carbon segregation around the Cottrell atmosphere zone is about 10 nm, which can be treated using atomistic simulations. On the other hand, it takes several months to reach saturation for a Cottrell atmosphere at room temperature [Massardier *et al.*, 2004], which explains the difficulty of describing it at an atomistic level. A number of recent works have investigated the interaction of straight dislocations with a carbon atom using the elasticity theory, molecular statics and dynamics, and *ab initio* calculations [Tapasa *et al.*, 2007; Clouet *et al.*, 2008; Hanlunmyuang *et al.*, 2010; Veiga *et al.*, 2010, 2011]. These researches provide important knowledge about carbon behaviour as it interacts with the dislocation stress field. For instance, it has been proved in ref. [Veiga *et al.*, 2010] that the stress field of an edge and a screw dislocation introduces a bias in the diffusion of a single carbon atom sufficiently close to the line defect. This bias is expected to be the driving force for the atmosphere to grow. However, none of these works offer an insight into the consequences of having more than one carbon atom around a dislocation. In ref. [Veiga *et al.*, 2012], a simple crude estimate of carbon distribution in Cottrell atmospheres was obtained by statistical physics with carbon-dislocation binding energies from Molecular Statics (MS). By performing first-principles calculations, Ventelon *et al.* have recently found that carbon segregation induces the reconstruction of the screw dislocation core [Ventelon *et al.*, 2015]. Furthermore, the effect of Cottrell atmospheres on the mobility of a screw dislocation in low carbon Fe-C alloys has been investigated by molecular dynamics simulations, with the atmospheres themselves being built via on-lattice Metropolis Monte Carlo (MMC) [Veiga *et al.*, 2015]. Molecular Dynamics (MD) simulations performed by Khater *et al.* have shown the role of carbon in solid solution (*i.e.*, randomly distributed in the simulation box) on the glide of an edge and a screw dislocation in bcc iron [Khater *et al.*, 2014].

This chapter presents a framework for creating carbon Cottrell atmospheres

around an edge and a screw dislocation by MMC. With a novel minimization method, the convergence of the MMC simulation is attained in a reasonable amount of time, even considering a large simulation box. This chapter examines the effect of Cottrell atmospheres on the stress field surrounding the line defect. The question addressed in this chapter is whether or not the atmosphere cancels out and saturates the “attractive” stress field of the dislocation.

3.2 Method

3.2.1 Simulation box

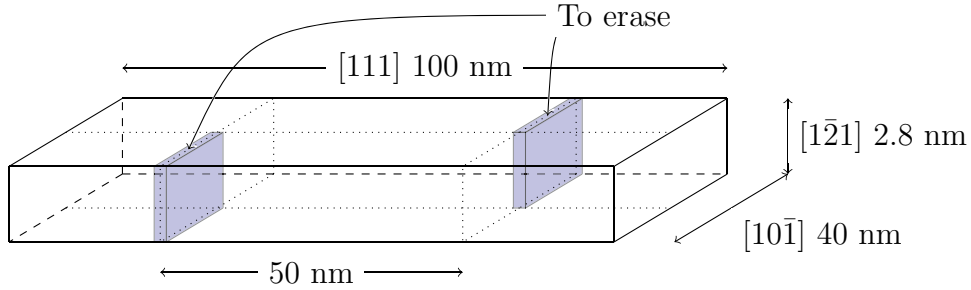


Figure 3.1: Creation of edge dislocations. The Fe atoms in the half planes (blue zones) are removed.

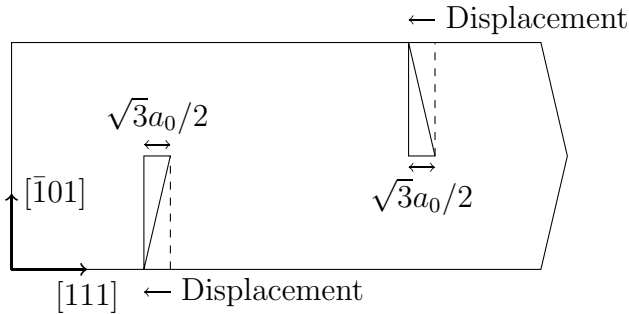


Figure 3.2: Displacement of Fe atoms after removing the half atomic planes depicted in fig. 3.1. The void space is filled after the energy and pressure minimization.

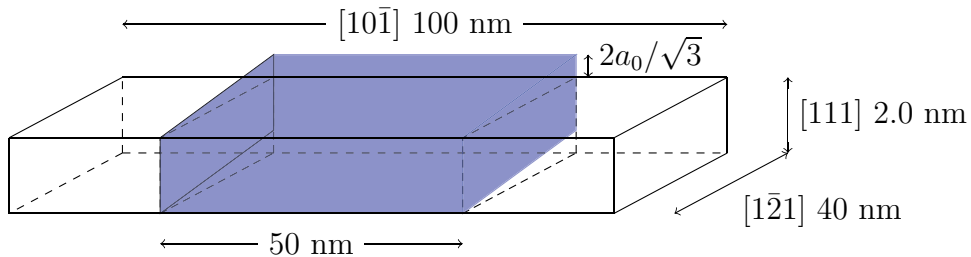


Figure 3.3: Creation of screw dislocations. The atoms in half of the simulation box are displaced as depicted by the blue zone.

The techniques employed to create edge and screw dislocations are depicted in figs. 3.1 and 3.3. Initially, the simulation box is filled with Fe atoms in perfect crystal with periodic boundary conditions in all three directions. For the edge dislocation, the atoms situated in two half atomic planes (*cf.* blue zones in fig. 3.1) are removed. The thickness of the half atomic planes is given by $2a_0/\sqrt{3}$, which corresponds to the distance between two atomic planes in the $[111]$ -direction, where a_0 is the lattice parameter ($a_0 = 0.286$ nm). After the atoms in the two half atomic planes are erased, the remaining atoms are displaced according to fig. 3.2 to avoid to create four dislocations due to the periodic boundary conditions. For the screw dislocation, half of the simulation box is displaced as depicted in fig. 3.3. In both cases, the potential energy and the pressure of the simulation box are then relaxed with the conjugate gradient (CG) method. For the pressure minimization, the box length in each direction is changed and the simulation box is also tilted until each component of pressure tensor is below 1 MPa. The stress fields around the dislocations obtained this way are compared with those given through the anisotropic elasticity theory [Hirth and Lothe, 1968]. It is confirmed that they are in a good agreement (*cf.* appendix B) In both cases, the dislocation cores are created in the positions as depicted in fig. 3.4. The dislocation line goes through the z -direction. The simulation box sizes are $100\text{ nm} \times 40\text{ nm} \times 2.8\text{ nm}$ (9.5×10^5 Fe atoms) for the edge dislocation and $100\text{ nm} \times 40\text{ nm} \times 2.0\text{ nm}$ (6.7×10^5 Fe atoms) for the screw dislocation. For both simulation boxes, the box size corresponds to a dislocation density of $5 \times 10^{14}\text{ m}^{-2}$, which is approximately of the same order of magnitude as for the specimen used in the atom probe tomography of ref. [Wilde *et al.*, 2000]. The distance between the dislocations is half the box size in the x direction and the box size in the y direction.

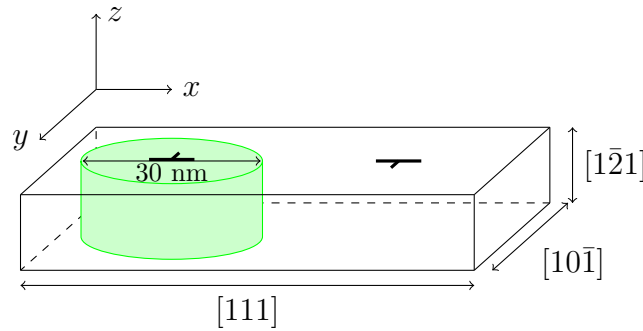


Figure 3.4: Simulation box containing two dislocations with a cylindrical zone (MMC zone) around a dislocation core (depicted in green) for MMC simulation

Initially, C atoms are homogeneously distributed inside the left half of the simulation box ($x < 50$ nm). Two neighbouring C atoms are not allowed to sit

within a distance of one lattice parameter (0.286 nm) in order to avoid overly high energy configurations, which might destabilise the system. The right half of the simulation box ($x > 50$ nm) was created by (i) duplicating the left half of the simulation box, (ii) rotating it by 180 degrees and (iii) mirroring it on the xy -plane. Then the energy and pressure of the whole simulation box were minimised via CG by relaxing both the atomic positions and the simulation box size and shape.

In order for the MMC simulation to converge within a reasonable amount of time, the MMC simulations are carried out only in the cylindrical region, as shown in figure 3.4. In the following, this region is referred to as the MMC zone.

3.2.2 Metropolis Monte Carlo

One MMC step is carried out following these steps:

1. Calculation of the current potential energy of the simulation box E_o
2. Random selection of one C atom inside the MMC zone
3. Selection of an interstitial site
4. Relocation of the C atom to this interstitial site
5. Energy minimization with CG and calculation of the new potential energy E_n
6. Acceptance or rejection of new state with the probability α (*cf.* eq. (3.4))
7. Back to 1

In the basic MMC, the probability of selecting one interstitial site (*cf.* step 3) is the same for all the interstitial sites. Consequently, the segregation of the C atoms around the dislocation line cannot be simulated in a reasonable amount of time. In order to speed up the process, the selection probability was modified by favouring the selection of the interstitial sites near the dislocation core over those far away from the dislocation core. Therefore, the selection of the interstitial site i is done according to the probability w_i , defined as:

$$w_i = \exp(-\lambda r_i) / W \quad (3.1)$$

where r_i is the distance between the interstitial site i and the dislocation core and $W = \sum_j^N \exp(-\lambda r_j)$ with the total number of interstitial sites N (*cf.* fig. 3.5). λ

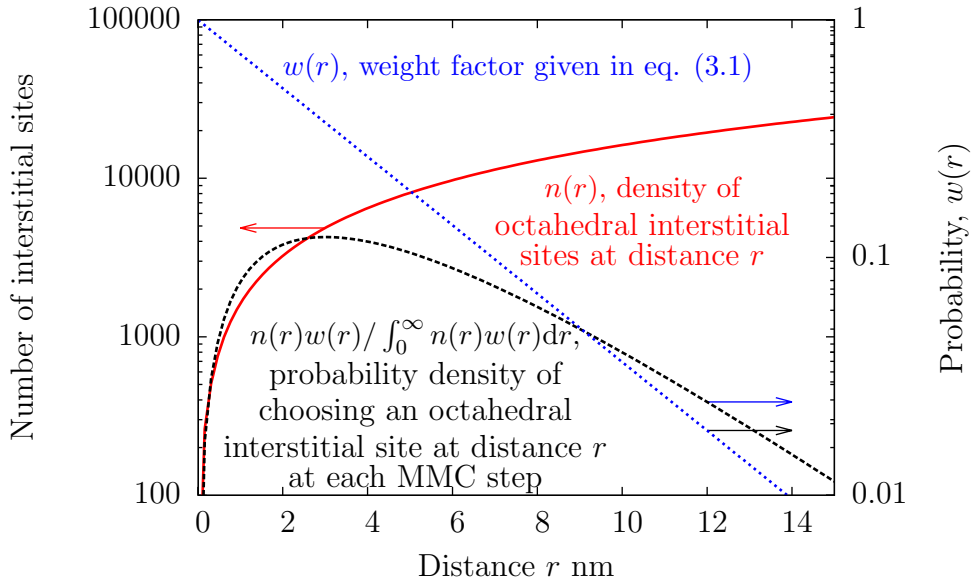
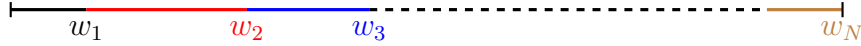


Figure 3.5: Variation of $n(r)$, $w(r)$ and $n(r)w(r)/\int_0^\infty n(r)w(r)dr$. The arrows show the axis to refer to for each curve.

is a weight factor that defines the strength of the bias [Veiga *et al.*, 2015]. For the selection of an interstitial site at each MMC step, a list of probabilities w_i of all the octahedral interstitial sites i is created as follows:



Then a number ξ which is between 0 and 1 is randomly chosen. The octahedral interstitial site i that satisfies the relation $\sum_{j=1}^{i-1} w_j < \xi < \sum_{j=1}^i w_j$ will be the new position of the C atom. If the selected interstitial site has a C atom within a distance of one lattice parameter, it is rejected and the selection process is repeated.

Since there are three interstitial sites for each Fe atom, the density of interstitial site $n(r)$ at the distance r from the dislocation line is given by $n(r) = 6\pi hr\rho$, where ρ is the Fe density and h is the height of the simulation box (*cf.* fig. 3.5). The probability $P(R)$ to choose an interstitial site within a radius R from the dislocation line in a simulation box of radius R_c , which is the radius of the MMC zone (*cf.* fig. 3.4), is:

$$P(R) = \frac{\int_0^R w(r)rdr}{\int_0^{R_c} w(r)rdr} \quad (3.2)$$

$$= \frac{-\lambda R \exp(-\lambda R) - \exp(-\lambda R) + 1}{-\lambda R_c \exp(-\lambda R_c) - \exp(-\lambda R_c) + 1} \quad (3.3)$$

λ is chosen in such a way that in 50 % of MMC steps, an interstitial site within

a radius of 5 nm from the dislocation line is chosen, *i.e.* $P(R = 5 \text{ nm}) = 0.5$. By putting $R_c = 15 \text{ nm}$, we obtain $\lambda = 0.3315 \text{ nm}^{-1}$.

The bias on the selection probability of an interstitial site must be counterbalanced by the acceptance probability α to respect the detailed balance condition. The acceptance probability is therefore calculated by [Veiga *et al.*, 2015]:

$$\alpha = \min \left[1, \frac{w_o}{w_n} \exp \left(-\frac{E_n - E_o}{k_B T} \right) \right] \quad (3.4)$$

where w_o and w_n are the probabilities of choosing the old site and the new site, respectively.

The main contribution of the proposed configuration (*i.e.* $E_n - E_o$ in eq.(3.4)) to the energy difference after energy minimisation is made through the rearrangement of iron atoms in the zones around the old position and the proposed position of the C atom. Therefore, only the cylindrical regions of 2 nm of radius around these positions are minimised in step 5 of the MMC scheme described above, in order to accelerate the simulation.

Since solely local minimizations are performed at each MMC step, it is important to enable the entire simulation box to attain the global energy minimum regularly, especially to deal with the tetragonal deformation of iron atoms around C atoms, which potentially leads to a global deformation of the simulation box. For this reason, at each 10^4 MMC steps, following operations are performed: 1, the carbon concentration outside the MMC zone (*cf.* fig. 3.4) is adjusted such that it corresponds to the concentration of the outer skin (thickness of 1 nm) of the MMC zone in order to achieve a continuous C concentration; 2, the left half of the simulation box is duplicated and rotated (see above); 3, energy and all stress components of the entire simulation box are minimized via CG.

3.3 Results

3.3.1 Convergence of MMC simulations

The simulations are launched for the temperatures of 300 K and 600 K with various numbers of C atoms ranging from 100 to 1,000 inside the MMC zone which correspond to the concentrations ranging from 0.059 at.% to 0.59 at.% for the edge dislocation and from 0.082 at.% to 0.82 at.% for the screw dislocation. 300 K is ambient temperature and 600 K corresponds to the temperature of the vessel of a nuclear reactor in operation.

The convergence of MMC is determined through the convergence of the poten-

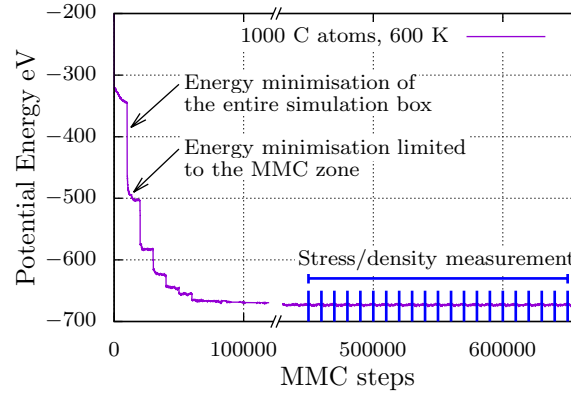


Figure 3.6: Evolution of simulation box energy as a function of MMC steps with 1,000 C for 600 K.

tial energy of the entire simulation box. In the case of a simulation box containing 1,000 C atoms at 600 K, the convergence can be seen at 1.5×10^5 MMC steps (*cf* fig. 3.6), where the major decline in energy is observed at each energy minimization of the entire simulation box. For all the simulations, 5×10^5 additional MMC steps are effectuated after reaching the equilibrium to obtain statistically reliable results for the carbon density and the stress field around the dislocation core. For the estimation of the carbon density and the stress field, the measurement is performed over the final 20 simulation snapshots, each of which were separated by 10^4 MMC steps. While the average values are taken for the C densities, the median values are used for the stress field in order to correctly measure the effect of the atmosphere saturation and not the local stress field of C atoms.

3.3.2 Carbon density distribution of Cottrell atmospheres

When the energy is converged, a large number of the C atoms, which were initially randomly distributed in the simulation box, segregated around the dislocation line (*cf.* figs. 3.7 and 3.8), which is in agreement with the theory of Cottrell and Bilby [Cottrell and Bilby, 1949]. At 300 K, 94 C atoms (94%) were found to sit within a radius of 8 nm from the dislocation line (*i.e.* within the atmosphere) for the system with 100 C atoms around an edge dislocation. This number is 462 (92.4 %) for 500 C atoms and 768 (76.8 %) for 1,000 C atoms. To check the dislocation saturation for the 1,000 C atoms system, an additional simulation was performed with 900 C atoms, where it was found that 745 (83.7%) C atoms were discovered to lie within the atmosphere. The “last 100 C atoms” are then distributed randomly since 23% enter the atmosphere, whereas 77% remain in the rest of the MMC zone, in agreement with the volume ratio of these regions. This repartition proves that the atmosphere has reached saturation (the chemical potential of C is homogeneous

throughout the MMC zone). For the screw dislocation, 440 C atoms were found within a distance of 8 nm of dislocation line for a box containing 600 C atoms. This number rose to 463 for a box with 800 C atoms. With the same logic, we can safely say that the saturation of Cottrell atmospheres for a screw dislocation arrived well below 800 C atoms in the simulation box.

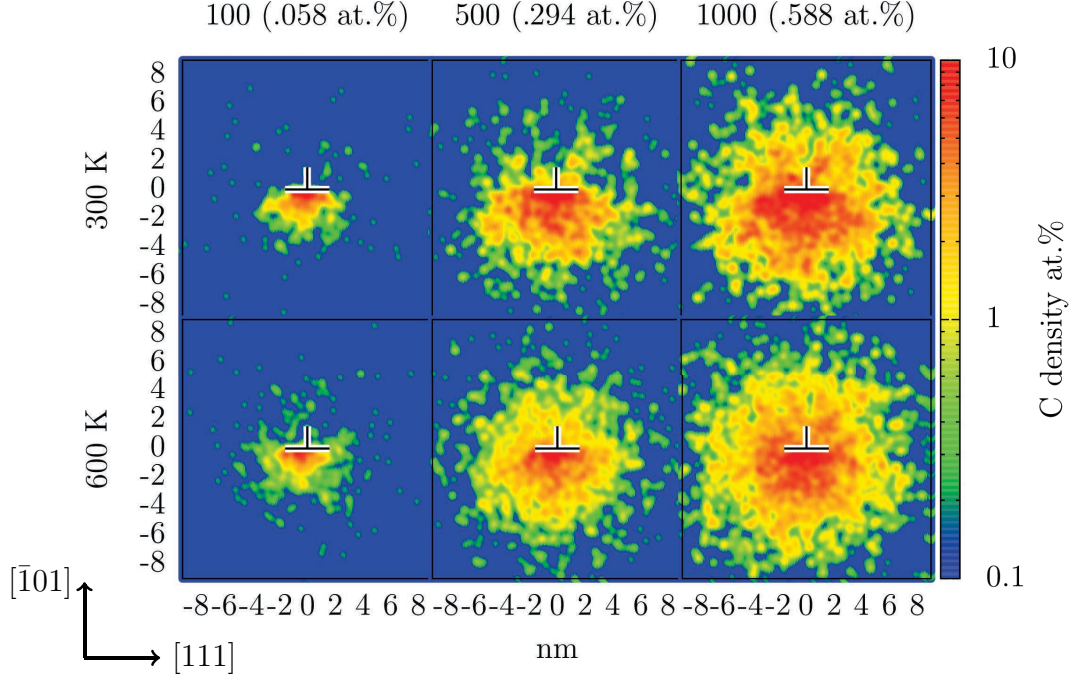


Figure 3.7: Averaged carbon density around an edge dislocation for 100, 500 and 1,000 C atoms (with the carbon concentrations of 0.059, 0.29 and 0.59 at.%) at the temperatures of 300 K and 600 K.

We measured a concentration of 8.84 at.%C within a radius of 1 nm for the simulation box containing 1,000 C atoms at 300 K around an edge dislocation. Around a screw dislocation, this value was found to be 9.02 at.%C for the simulation box containing 800 C atoms (which is higher in concentration than the simulation with an edge dislocation with 1,000 C) at 300 K. In ref. [Sherman *et al.*, 2007], a peak carbon concentration of the atmosphere was found to be of the order of 8 at.%C at room temperature with the atom probe tomography. More recently, Veiga and co-workers estimated the carbon saturation concentration in Fe-C martensite as 10 at.% [Veiga *et al.*, 2012] using a rudimentary Monte Carlo method. Furthermore, atom probe tomography experiments [Wilde *et al.*, 2000] indicate the atmosphere radius to be 7 ± 1 nm, which is also in agreement with figs. 3.7 and 3.8. The analytical calculation carried out in ref. [Cochardt *et al.*, 1955] predicted the C concentration at saturation to be inversely proportional to the distance from the edge dislocation line and a concentration of 7 at.%C at a distance of one Burgers vector from the dislocation line. A C concentration of

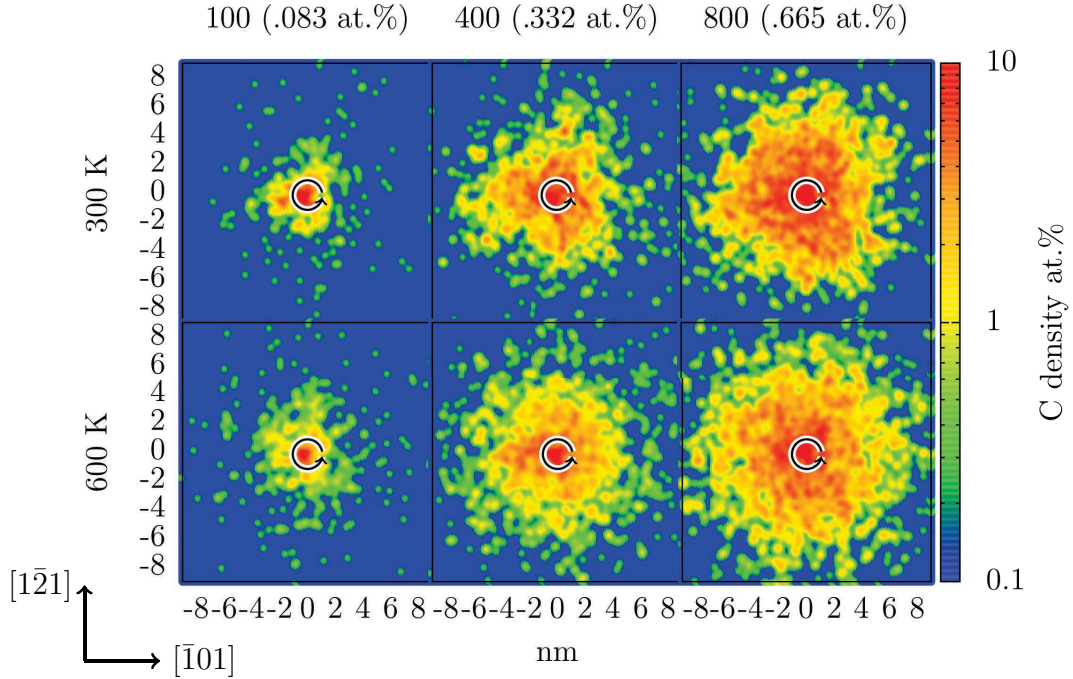


Figure 3.8: Averaged carbon density around a screw dislocation for 100, 400 and 600 C atoms (with the carbon concentrations of 0.083, 0.332 and 0.665 at.%) at the temperatures of 300 K and 600 K.

8.14 at.%C was measured at a distance of one Burgers vector. In the same article, a concentration of 6 at.%C was predicted at a distance of one Burgers vector for a screw dislocation. In our simulation, a C concentration of 5.40 at.%C was obtained. Moreover, within a $10 \times 10 \text{ nm}^2$ region encompassing the dislocation lines, we obtained 144 C atoms per nanometer of dislocation for the simulation box with 1,000 C. This result is in good quantitative agreement with the result of 133 C/nm based on the Fermi-Dirac statistics presented in ref. [Veiga *et al.*, 2012], regarding the same initial carbon content. These comparisons show a remarkable consistency of our computer simulation study with the atom probe tomography and a theoretical calculation.

It was also observed that at lower carbon concentrations, the C atoms tend to occupy interstitial sites within the traction zone around an edge dislocation, whereas at higher carbon concentration, interstitial sites in both traction and compression zones were occupied.

The C concentration far from the dislocation drops from a nominal concentration of 0.059 at% to 0 at%, from 0.29 at% to 0.0094 at% and from 0.59 at% to 0.021 at%, for systems of 100, 500 and 1,000 C atoms. This demonstrates a massive C depletion due to the presence of dislocations, which is in agreement with [Wilde *et al.*, 2000].

Finally, as expected, a comparison of the average C densities obtained at 300 K

and 600 K indicates the extent of the Cottrell atmosphere is larger at higher temperatures than at lower ones.

3.3.3 Evolution of stress field

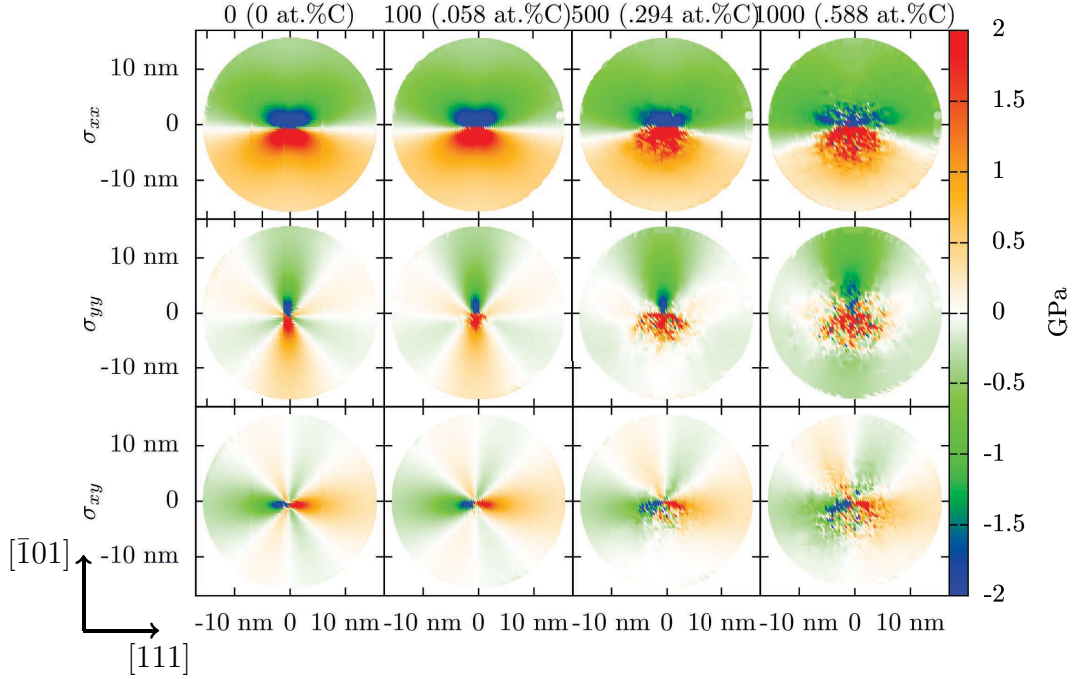


Figure 3.9: Stress around an edge dislocation for 0, 100, 500, 1,000 C atoms inside the MMC zone for 300 K for the stress components of σ_{xx} , σ_{yy} and σ_{xy} which are non zero according to the isotropic elasticity theory.

The stress components σ_{xx} , σ_{yy} and σ_{xy} around an edge dislocation, which are non-zero according to the isotropic elasticity theory, for 300 K are shown in fig. 3.9. The increase in the number of C atoms in the Cottrell atmosphere does not give a visible variation in the amplitude of stress field for the most prominent component σ_{xx} . The contrast between the compression and traction zones for the σ_{yy} component below the dislocation, that was clearly visible in the simulation box without C atoms, disappeared for 1,000 C atoms (0.59 at.%C). The stress components σ_{xz} and σ_{yz} around a screw dislocation, which are non-zero according to the isotropic elasticity theory, at 300 K are shown in fig. 3.10. Over the evolution of Cottrell atmospheres, these stress components do not show a particular evolution pattern.

The stress at a distance between 14 nm and 15 nm from the dislocation line was measured as a function of the investigated angle θ (*cf.* figs. 3.13 and 3.12). Also, while the stress magnitude in the compression zone of σ_{xx} shrank, the stress in the traction zone increased when adding more C atoms. For the two other

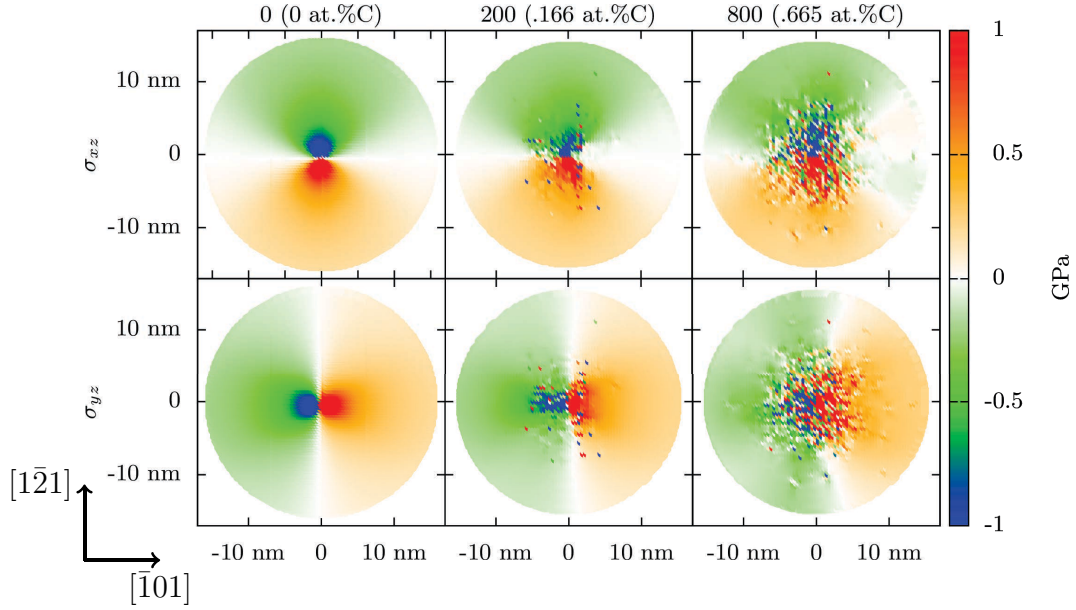


Figure 3.10: Stress field around a screw dislocation for 0, 200, 800 C atoms inside the MMC zone for 300 K for the stress components of σ_{yz} and σ_{xz} which are non zero according to the isotropic elasticity theory.

components σ_{yy} and σ_{xy} , no clear convergence could be observed. In general, for all of the stress components, the stress around the dislocation is not reduced after the formation of Cottrell atmospheres, which implies that with the growth of a Cottrell atmosphere, its stress induced “attraction force” does not diminish. This result is in good agreement with a previous calculation [Cai *et al.*, 2014], which was performed with the isotropic elasticity theory; following this calculation, it was concluded that the presence of interstitial atoms around a dislocation does not have a global effect on its stress field.

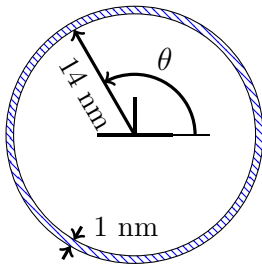


Figure 3.11: Definition of the angle θ for the results in figs. 3.12 and 3.13. The stress of the Fe atoms in the hatched zone is taken for the measurement.

Therefore, the implication of this result is that Cottrell atmospheres around an edge or a screw dislocation reach their saturation not because of the decrease in stress, but because of the chemical interactions between C atoms, which become more important than the elastic interaction between the C atoms and the dislocation. According to refs. [Becquart *et al.*, 2007] and [Sinclair *et al.*, 2010], the repulsive interaction energy between two C atoms in neighbouring positions in the iron matrix is mostly due to chemical interactions (rather than mechani-

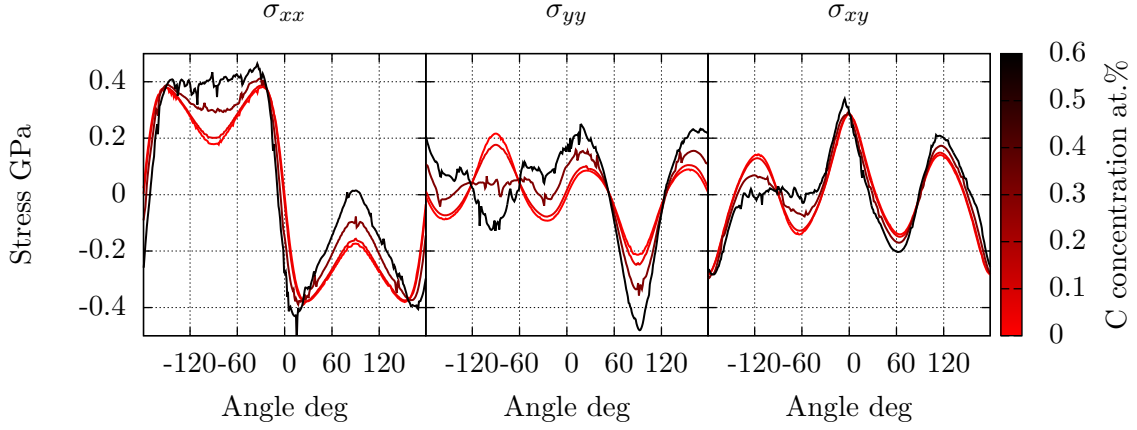


Figure 3.12: Stress around an edge dislocation at the distance of 14 nm as a function of the angle around the dislocation (*cf.* fig. 3.11).

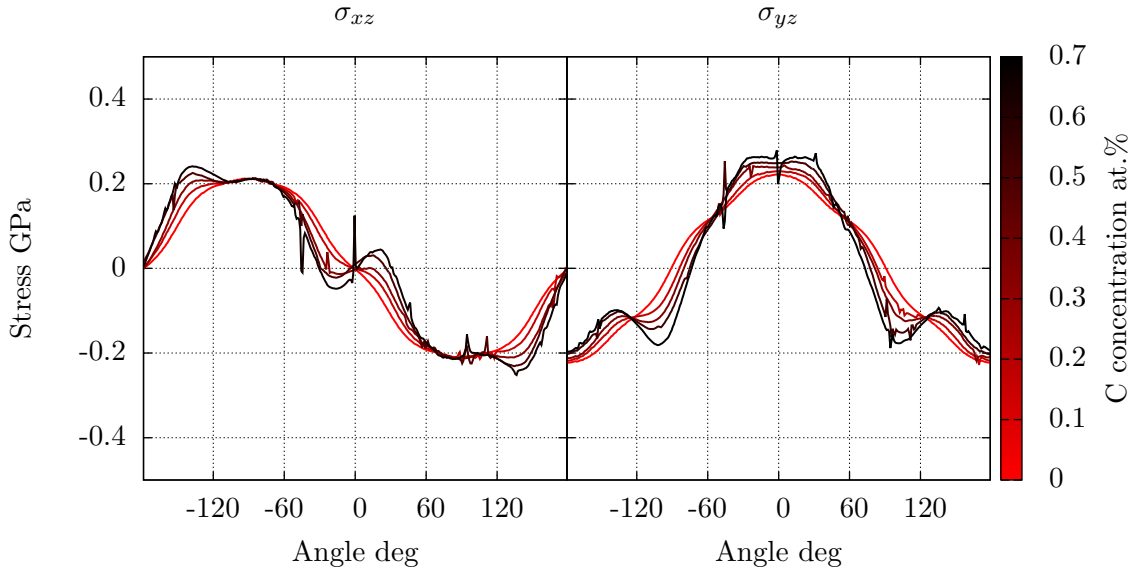


Figure 3.13: Stress around a screw dislocation at the distance of 14 nm as a function of the angle around the dislocation (*cf.* fig. 3.11).

cal interactions) and can be as high as 0.67 eV. When the Cottrell atmosphere reaches a certain size, the thermal energy compensates for the long-range elastic interactions of dislocations and the evolution of the atmosphere stops.

3.3.4 Carbon ordering around dislocations

In the previous chapter, the C ordering was investigated starting from a small bulk simulation box in which C atoms in half of the simulation box were already

ordered and in the other half of the simulation box they were disordered. However it is an energetically unstable configuration and would not exist in reality. On the other hand, as C ordering is provoked by elastic interactions with the iron matrix, one may think of dislocations which play an initiator role for the C ordering. In this section, therefore, the ordering state of C atoms in the Cottrell atmospheres is investigated for both edge and screw dislocations at equilibrium. The three site types for both edge and screw dislocations have the normalized directions of dilatation that are given by:

$$\vec{v}_{[100]} = \left(\frac{1}{\sqrt{3}}, -\frac{1}{\sqrt{2}}, \frac{1}{\sqrt{6}} \right), \vec{v}_{[010]} = \left(\frac{1}{\sqrt{3}}, 0, -\frac{2}{\sqrt{6}} \right), \vec{v}_{[001]} = \left(\frac{1}{\sqrt{3}}, \frac{1}{\sqrt{2}}, \frac{1}{\sqrt{6}} \right) \quad (3.5)$$

A comparison between the site type distribution and the binding energy distribution around an edge dislocation (*cf.* fig. 3.14) shows a clear correlation. This tendency is less pronounced in the case of a screw dislocation (*cf.* fig. (3.15)).

Fig. 3.16 shows the number of C atoms in each site type for various C contents at 300 K and 600 K. For both edge and screw dislocations, it can be seen that the C atoms occupy preferably the sites of type [100] and [001] at 300 K, which is somewhat less marked for 600 K. Clearly, the [010]-type sites are less occupied for both edge and screw dislocations, even though in the case of a screw dislocation, the amplitude of the binding energy was reported to be about the same for all three site types (*cf.* fig. (3.15)). This is probably related to the length of the component of $\vec{v}_{[010]}$ in the direction along the dislocation line (*cf.* discussion in chap. 2 sec. 2.4.2), which is two times as large as the z components of $\vec{v}_{[100]}$ and $\vec{v}_{[001]}$ (*cf.* eq. (3.5)). This means that a C atom in a [010]-type site creates an elastic dipole that would dilate the surroundings in the direction of the dislocation line more strongly than the two other site types. Having several C atoms in the [010]-type sites simultaneously would give a group of elastic dipoles in “series” along the dislocation line, which is less favorable than having elastic dipoles in parallel from the energetic point of view. Accordingly, the C atoms avoided the [010]-type sites and took [100]- and [001]-type sites instead.

3.3.5 Evaluation of λ and comparison with the model of Cottrell

The value of the parameter λ (*cf.* eq. (3.1)), that determines the amplitude of MMC bias, was selected such that the probability of choosing an interstitial site

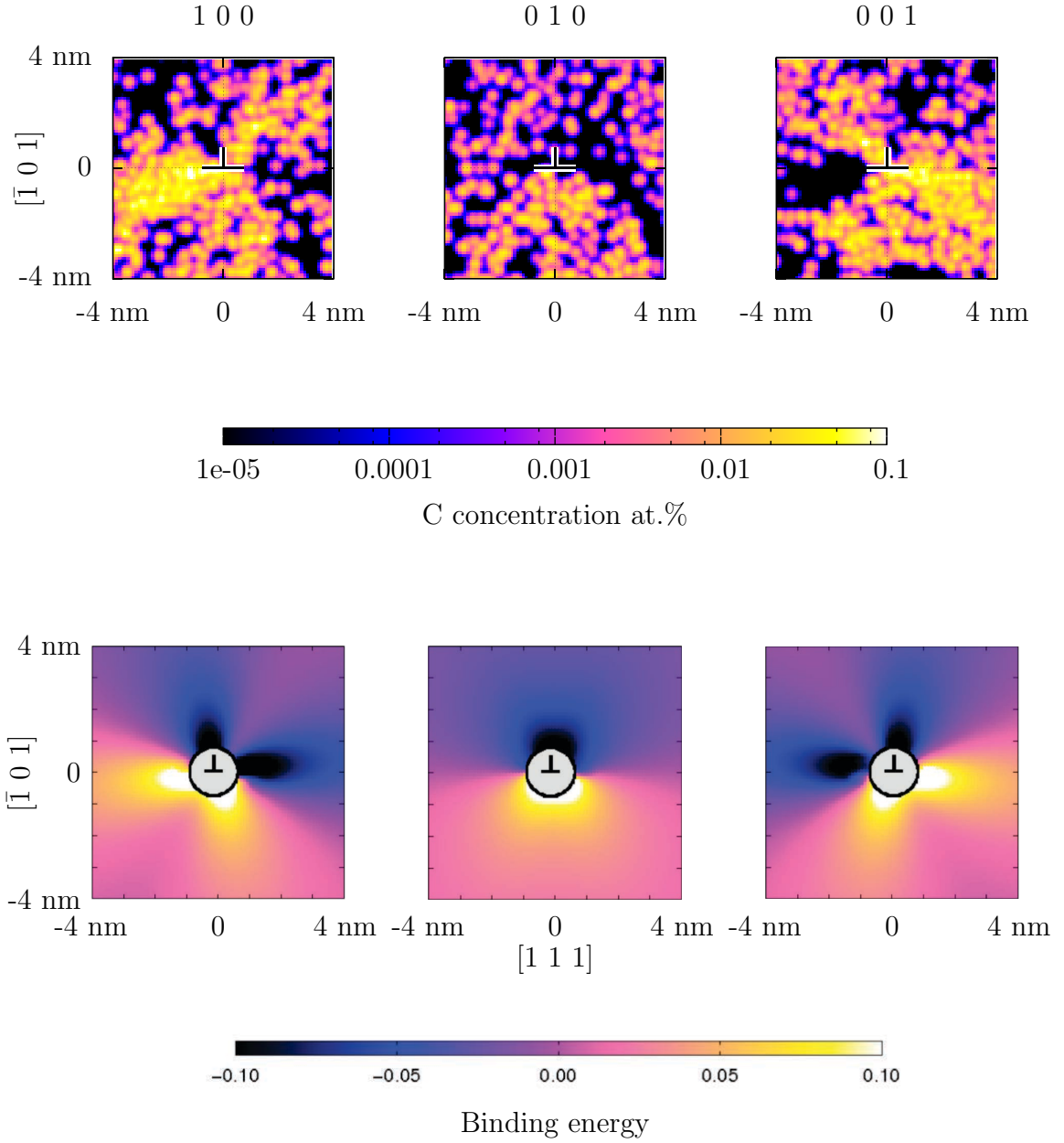


Figure 3.14: Top: C distribution around an edge dislocations with 1,000 C at 300 K. Bottom: Binding energy around an edge dislocation reproduced from [Veiga, 2011]

within a radius of 5 nm from the dislocation line is 50 % at each MMC step. This criterion, however, is not based on the distribution of C atoms around a dislocation line. In this section, λ is calculated from the C distribution around edge and screw dislocations to compare with the value that was used for the simulations $\lambda = 0.3315\text{ nm}^{-1}$. For this, the number of C atoms was counted as a function of the distance from the dislocation line and spatially normalized.

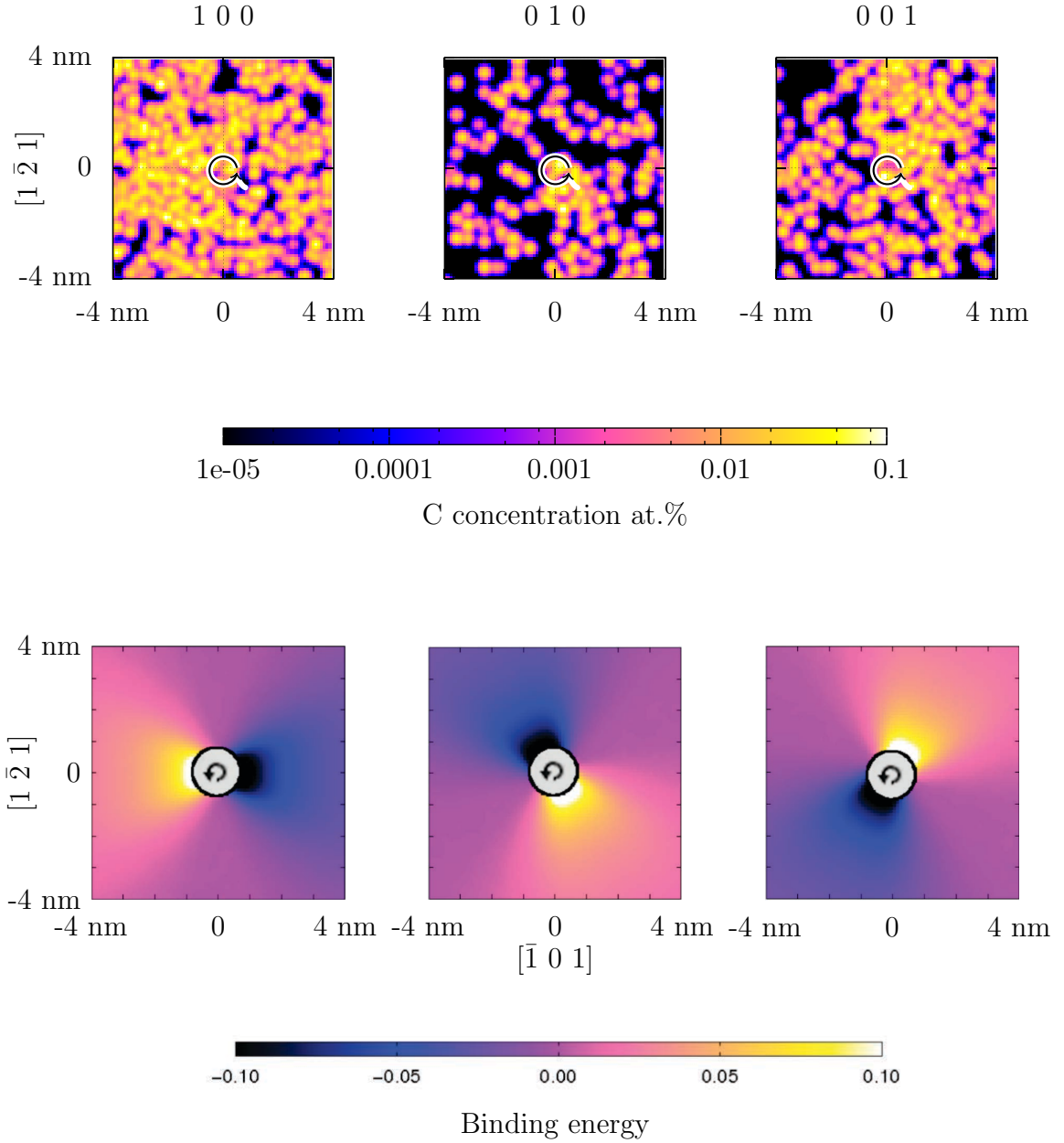


Figure 3.15: Top: C distribution around an screw dislocations with 800 C at 300 K. Bottom: Binding energy around an screw dislocation reproduced from [Veiga, 2011]

Model of Cottrell

The exponential decline of C concentration with the distance from the dislocation line can be well observed for all simulations (*cf.* fig. 3.17). Despite the clear deviation of distribution for different C contents in the zone far from the dislocation line, the concentration at the core is of about the same order for all C contents, meaning the core region is strongly binding and the rest of the simulation box is gradually occupied with the growing number of C atoms. It can be somewhat seen that when the temperature is low, the C atoms are concentrated in a smaller

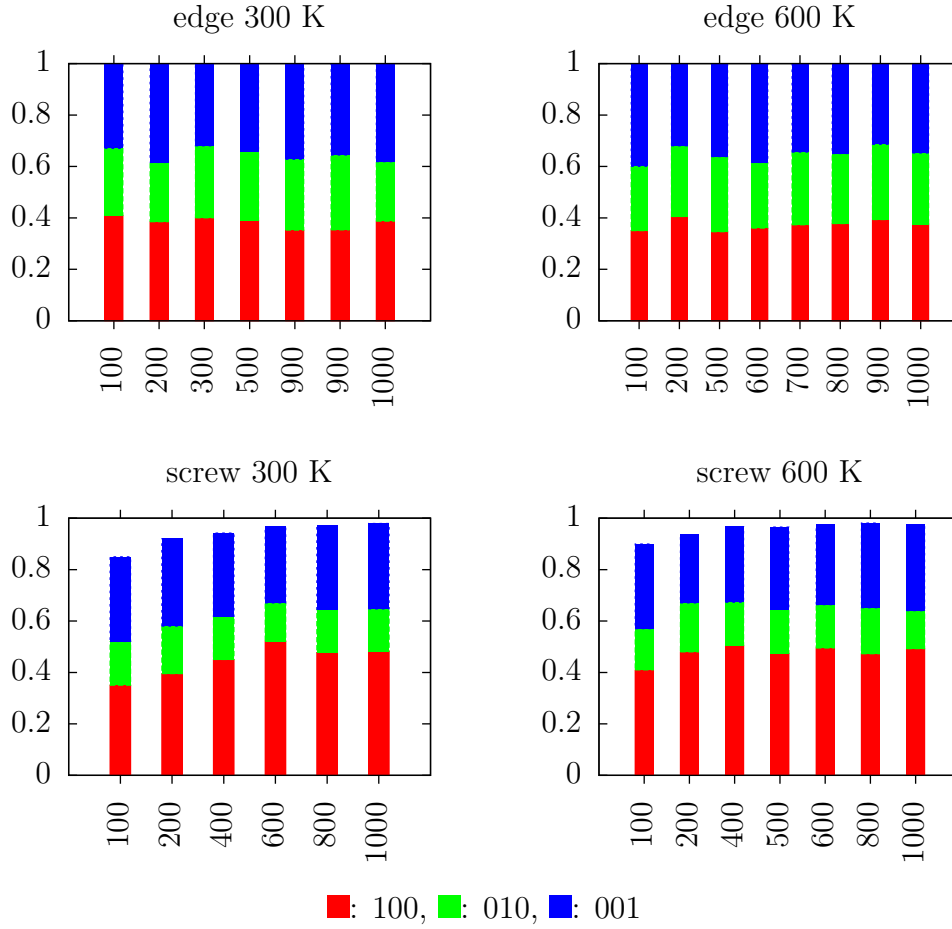


Figure 3.16: Carbon fraction in different site types around an edge and a screw dislocation for 300 K and 600 K with various C contents ranging from 100 to 1,000 C atoms inside the MMC zone.

region around the dislocation line. This temperature effect, however, is obviously rather insignificant and at higher C concentrations, it is almost invisible.

The value $\lambda = 0.3315 \text{ nm}^{-1}$ was generally smaller than the value that would give the real C concentration distributions. An alternative method to choose λ would be to use the anisotropic elasticity theory presented by Hirth *et al.* [Hirth and Lothe, 1968], since it has been reported that the binding energy calculated using this theory is well comparable with the binding energy calculated from the interatomic potential of this study.

The exponential variation of the C concentration profile as a function of the distance from the dislocation line slightly deviates in the region near the dislocation core in fig. 3.17. According to the theory of Cottrell [Cottrell, 1948], the C distribution around an edge dislocation is given in the form:

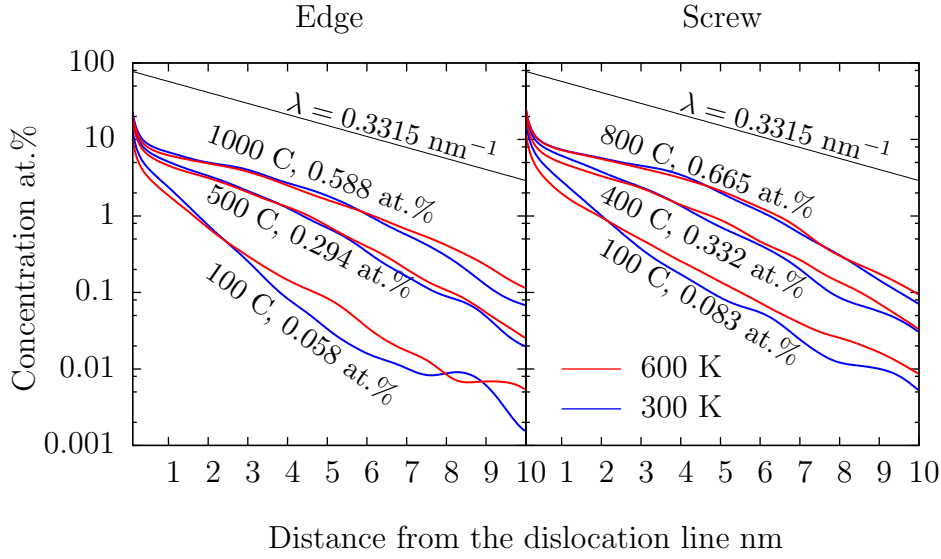


Figure 3.17: Concentration profile around an edge dislocation for various temperature and concentration values. Blue and red lines are for 300 K and 600 K, respectively. The black line represents the C distribution slope given by the weight factor $\lambda = 0.3315 \text{ nm}^{-1}$, *i.e.* $c(r) = c_0 \exp(-\lambda r)$, where $c(r)$ is the distribution and c_0 is the C concentration at the core.

$$c(r, \theta) = c_0 \exp\left(-\frac{A \sin \theta}{r k_B T}\right) \quad (3.6)$$

where A is a constant that can be calculated from the material property, r is the distance from the dislocation line and θ is the angle around the dislocation line (defined in fig. 3.11). Looking at the C distribution in the previous section, the dependence on θ does not hold for higher C contents. Taking this into consideration, we can safely assume that $\sin \theta$ takes some constant value between 0 and -1, which means the binding energy is positive near the dislocation line and does not depend on the angle for higher C contents. Then eq. (3.6) turn into the form:

$$c(r) = c_0 \exp\left(\frac{B}{rT}\right) \quad (3.7)$$

where B is a positive constant that does not depend on the temperature and the distance from the dislocation line. Eq. (3.7) indicates in particular, that the variation of the logarithm of the C concentration is inversely proportional to the distance from the dislocation line, *i.e.*

$$\log \left(c \left(\frac{1}{r} \right) \right) - \log(c_0) = \frac{Br}{T} \quad (3.8)$$

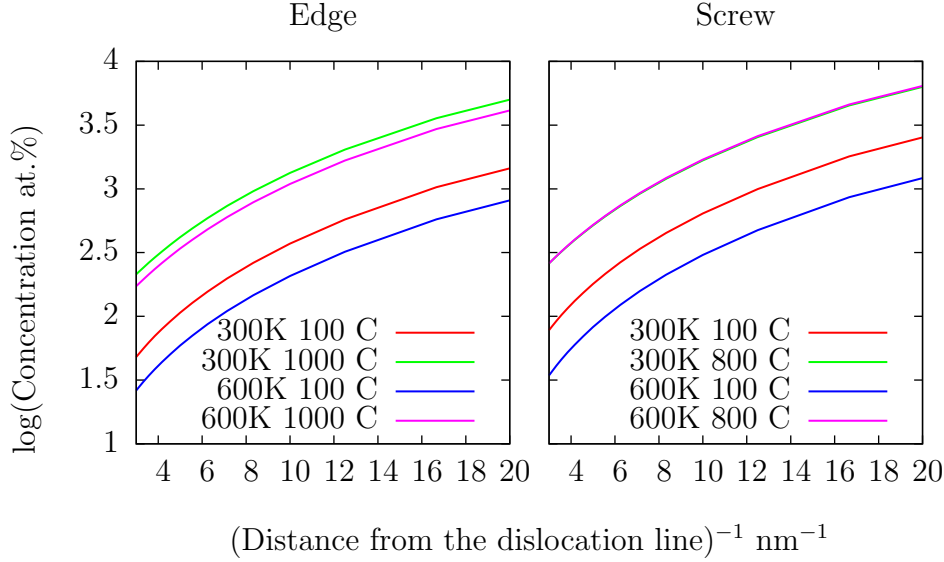


Figure 3.18: Concentration profile around an edge dislocation for various temperature and concentration values in logarithmic scale as a function of inverse distance.

Edge dislocation				Screw dislocation			
	100 C	500 C	1,000 C		100 C	500 C	1,000 C
300 K	-0.0320	-0.0301	-0.0297	300 K	-0.0327	-0.0297	-0.0300
600 K	-0.0322	-0.0305	-0.0298	600 K	-0.0335	-0.0309	-0.0301

Table 3.1: Slopes of the function $\log(c(1/r))$ in nm^{-1} (*i.e.* B/T of eq. (3.7)) calculated from the region shown in fig. 3.18.

$\log(c(1/r))$ is shown in fig. 3.18 for 300 and 600 K with various C contents and the values of the slopes are given in tab. 3.1. The linear variation of $\log(c)$ on $1/r$, which is predicted in the theory of Cottrell, can be observed in the region near the dislocation line (higher values in abscissa). However, whereas the slopes for 300 K would be twice as much as for 600 K according to the model of Cottrell, this cannot be observed in any case. This is probably due to the C-C interactions that were not taken into account in the original model.

3.4 Conclusion

In this chapter, MMC with atomistically informed energies and configurations were used to build carbon Cottrell atmospheres around edge and screw dislocations at 300 and 600 K for various carbon contents. The speed-up of MMC was undertaken by performing local energy minimization at each MMC step and by biasing the selection probability of an interstitial site. The carbon density of Cottrell atmospheres and the corresponding stress field around the dislocation were measured. Within the limits of the potential, carbon concentrations around the dislocation line were in good agreement with experimental results and theoretical calculations. For both edge and screw dislocations, minor change in stress field could be observed with the existence of the Cottrell atmospheres, but globally, the stress did not decline. Overall, the dislocation stress field was not saturated with the growing number of C atoms in the Cottrell atmosphere, indicating that the saturation of Cottrell atmospheres is not triggered by a decline in the attraction force as a consequence of the shrinking stress, but by the chemical interactions between C atoms that become important after a certain number of C atoms reach the region around the dislocation.

The investigation on the distribution of C atoms at different site types around edge and screw dislocations showed that the C atoms do not assume the different sites homogeneously. A comparison with a previous study that calculated the binding energy around an edge dislocation showed a clear relation of the binding energy and the distribution of site types.

An investigation into the distribution of C atoms showed no dependence of the density of C atoms as a function of the distance from the dislocation line on the temperature. This contradicts the first model of Cottrell [Cottrell, 1948], likely due to the C-C interactions, which were not taken into account in the model of Cottrell.

Chapter 4

Formation kinetics of carbon Cottrell atmospheres

Abstract

In this chapter, the formation kinetics of Cottrell atmospheres via Atomistic Kinetic Monte Carlo (AKMC) method is presented, which employs Linear Combination of Stress State (LinCoSS) method to calculate the activation energy. Firstly, the extent of the zone in which LinCoSS gives correct activation energies, is investigated around an edge and a screw dislocation. For the treatment of the core region, the Cottrell atmospheres are replaced by those which are prepared in advance via Metropolis Monte Carlo, presented in the previous chapter. Since the direct interactions between C atoms cannot be calculated via LinCoSS, a library of chemical interactions for two C atoms is created, which is integrated into AKMC. Those which are outside the AKMC zone perform a random walk and may also enter the AKMC zone. Lastly, the scheme to integrate these methods is presented, in order to calculate the time required to attain different stages of atmosphere formation. It gives a saturation behaviour, which is comparable with experimental results.

4.1 Introduction

While it is possible to construct saturated Cottrell atmospheres for any C concentration via Monte Carlo Metropolis (MMC), the time that is required for the Cottrell atmospheres to attain saturated states and the pathways of C atoms remain unknown. With the knowledge of the interstitial jump paths and their associated activation energies, the evolution kinetics from the initial state of homogeneous carbon distribution to the saturated stages can be calculated with AKMC (*cf.* chap. 1 sec. 1.4). While the paths of the interstitial jumps in bcc iron are easy to detect, their associated activation energies vary in a complex manner depending on the position of the C atom with regard to the dislocation core and to the configuration of C atoms in the vicinity. Standard activation energy calculation methods include Climbing Image Nudged Elastic Band (CI-NEB)) [Henkelman *et al.*, 2000; Henkelman and Jónsson, 2000] or Activation Relaxation Technique (ART) [Barkema and Mousseau, 1996]. In these methods, a C atom is forced to go through the trajectory of an interstitial jump and the energy barrier at 0 K is calculated via MS. However, the iterative computation with MS requires a lengthy calculation, which is impossible to perform at each AKMC step for each C atom to know the saturation kinetics of Cottrell atmospheres from the technical point of view. In the Ph.D thesis of R. Veiga [Veiga, 2011], the activation energies of all possible interstitial paths were calculated using modified ART for a simulation box containing a dislocation without C in advance. Then an AKMC simulation was performed using these activation energy values to evaluate the effect of the existence of a dislocation on the kinetics of the C atoms. However, it took neither the evolution of stress field over the course of the atmosphere saturation nor carbon-carbon interactions into account, which means the sole possible saturation comes from C depletion in the whole matrix, which is not very realistic, since an important part of C can remain in the matrix after saturation [Wilde *et al.*, 2000]. Also, C interactions and the evolution of stress field are both predicted to evolve over the course of atmosphere saturation [Cottrell and Bilby, 1949]. In order to take them into account, the activation energy calculation is performed through Linear Combination of Stress State (LinCoSS) method, which translates the local stress field around each C atom into their activation energies [Tchitchekova *et al.*, 2014]. The activation energy E of LinCoSS for a given stress σ_{ij} with $i, j = x, y, z$

is given through an ensemble of equations given in the form:

$$\begin{aligned}
 \underbrace{E(\sigma_{xx}, \sigma_{yy}, \sigma_{zz}, \sigma_{xy}, \sigma_{yz}, \sigma_{xz})}_{\text{Activation energy due to variation of all stress components}} &= \underbrace{E(\sigma_{xx}, 0, 0, 0, 0, 0)}_{\text{Activation energy due to variation of } \sigma_{xx}} + E(0, \sigma_{yy}, 0, 0, 0, 0) \\
 &+ E(0, 0, \sigma_{zz}, 0, 0, 0) + E(0, 0, 0, \sigma_{xy}, 0, 0) \\
 &+ E(0, 0, 0, 0, \sigma_{yz}, 0) + E(0, 0, 0, 0, 0, \sigma_{xz}) \\
 &- 5E(0, 0, 0, 0, 0, 0)
 \end{aligned} \tag{4.1}$$

where E is a polynomial of order 2 of each component of the local stress around the C atom σ_{ij} $i, j = x, y, z$. As it can be seen from this equation, it is assumed that the activation energy is additive, *i.e.* the total activation energy can be given by adding the activation energy obtained from each stress component. A detailed description is given in chap. 1, sec. 1.4.2. LinCoSS itself does not require iterative methods such as MD or MS. This makes the calculation of diffusion kinetics of C atoms around dislocations feasible from the point of view of computation time. Yet there are two main problems with the choice of LinCoSS. Firstly, the linear decomposition and the polynomial expansion up to the order 2 of LinCoSS (*cf.* eq. (4.1)) is not valid in the region near the dislocation line, as the stress is too high for LinCoSS to give correct activation energy values [Tchitchekova *et al.*, 2014]. Regarding this problem, the limit of LinCoSS was not given in a way that is relevant to the purpose of our research in the original article, as the limit of LinCoSS with regard to the stress was measured in a bulk and the quantitative limit around dislocations was not measured. Secondly, the carbon-carbon chemical interactions are not accounted for in LinCoSS, as the activation energies are solely obtained through the local stress around each C atom.

This chapter is composed of the following sections: firstly, the limit of LinCoSS around edge and screw dislocations is investigated thoroughly by comparing the results of LinCoSS with those of CI-NEB. Then a method to treat the carbon-carbon interactions is proposed. Lastly, the final scheme and the result of AKMC are presented for the investigation of the formation kinetics of Cottrell atmospheres.

4.2 Limit of LinCoSS

From the original article presenting LinCoSS, it is known that in the vicinity of a dislocation core the activation energy values calculated through LinCoSS deviate from those calculated through CI-NEB (*cf.* chap. 1 sec. 1.4.1), which is considered

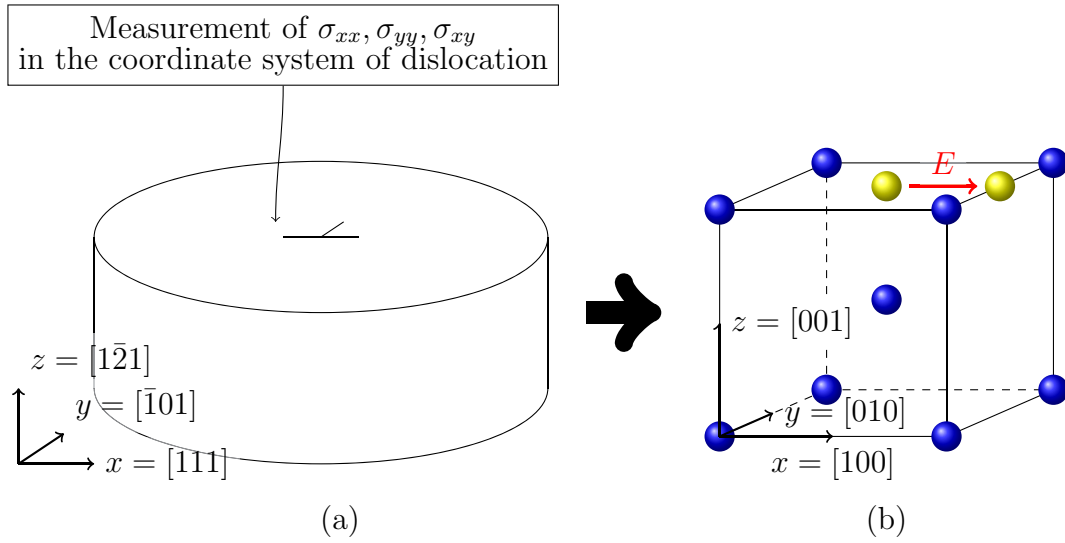


Figure 4.1: In the original article of LinCoSS [Tchitchekova *et al.*, 2014], the error of LinCoSS was measured by taking the stress field around an edge dislocation (*cf.* (a)) in the coordinate system of the dislocation. This stress field was reproduced in the bulk in the coordinate system of the bulk without performing a coordinate transformation (*cf.* (b)).

to deliver the correct values. In the original paper, the limit of LinCoSS was calculated as follows: 1. The stress around an edge dislocation is obtained in the coordinate system of the dislocation, *i.e.* the z -axis coincides with the dislocation line, making σ_{xx} , σ_{yy} and σ_{xy} the only one non zero stress components. 2. The stress is reproduced in a bulk in the coordinate system of bulk without performing a coordinate transformation. 3. An interstitial jump from a z -type site to a y -type site is performed via CI-NEB and this activation energy was compared with that of LinCoSS. A schematic representation is given in fig. 4.1. In this procedure, there were mainly two problems: firstly, since the coordinate system of a simulation box containing an edge dislocation ($[111]$, $[\bar{1}01]$, $[1\bar{2}1]$) is not the same as the coordinate system of the bulk employed ($[100]$, $[010]$, $[001]$), the local stress field affects the activation energy differently. Secondly, the information on the stress gradient around the dislocation is lost in a bulk. These arguments give rise to the need of investigating the exact extent of the region in which LinCoSS is not valid around an edge and a screw dislocation.

In this section, the energy values calculated by LinCoSS around an edge and a screw dislocation are compared with those calculated with CI-NEB. Since the interest of AKMC is to investigate the kinetics of carbon diffusion, the error is evaluated in terms of diffusion coefficient at the temperature of 300 K instead of the activation energies themselves, considering the diffusion coefficient follows the

Arrhenius law:

$$D = D_0 \exp\left(-\frac{E}{k_B T}\right) \quad (4.2)$$

where E is the activation energy. The prefactor D_0 can be calculated via *ab initio*, MD at higher temperature or from experiments. From various experimental results, we estimate it as $D_0 = 5.0 \times 10^{-7} \text{ m}^2/\text{s}$ (*cf.* appendix C).

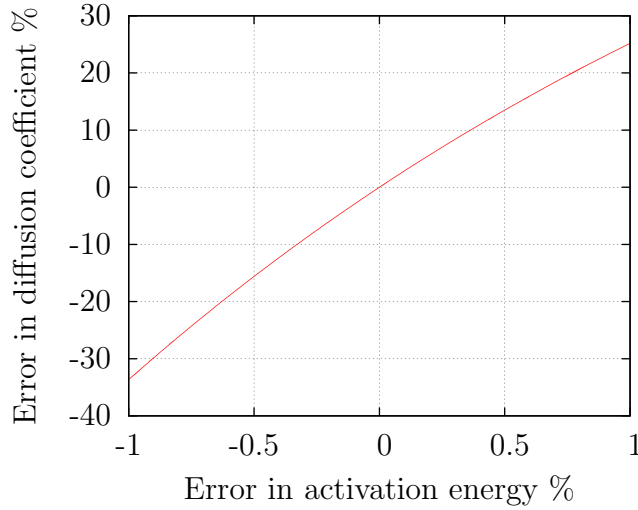


Figure 4.2: Error in diffusion coefficient as a function of the error in activation energy at the temperature of 300 K. The activation energy in stress free state $E_0 = 0.8153 \text{ eV}$ and the associated diffusion coefficient are taken as the reference values

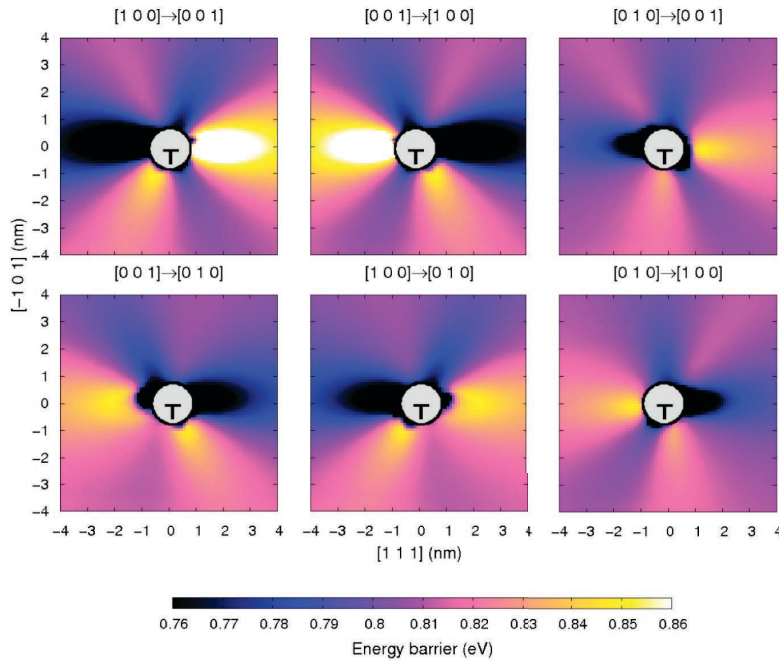


Figure 4.3: Activation energy variation around an edge dislocation calculated from all possible interstitial jumps, reproduced from [Veiga, 2011]

The relative error in terms of diffusion coefficient at 300 K as a function of the relative error in activation energy is shown in fig. 4.2. It can be seen that the error

in diffusion coefficient surpasses 10 % for an error of the activation energy of 0.5 %. And if the activation energy is underestimated by 1 %, the error in diffusion coefficient surpasses 30 %. This result indicates that a small error in activation energy translates to a very large error in diffusion coefficient and the error in diffusion coefficient grows exponentially with the error in activation energy (*cf.* eq. (4.2)). Yet around a dislocation (*e.g.* edge dislocation *cf.* fig. 4.3), it can be seen that the variation of activation energy is much larger than 1 %, which implies the importance to perform a precise calculation of activation energy.

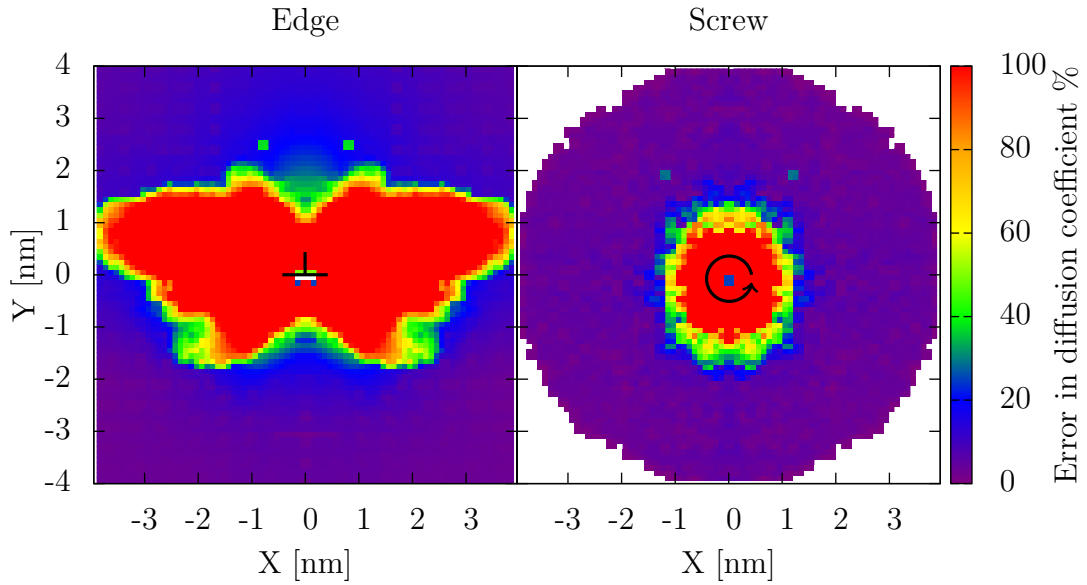


Figure 4.4: Error in diffusion coefficient around an edge and a screw dislocation for 300 K. The measurement is performed only in the region $X > 0$ due to the symmetry of the stress field. To better visualize the results the results are mirrored on the other side. Within each square of $0.04 \text{ nm} \times 0.04 \text{ nm}$, the maximum error value is shown.

In order to determine the zone around dislocations, in which LinCoSS delivers correct activation energy values, CI-NEB calculations are effectuated for one C atom in the simulation box containing an edge or a screw dislocation for all possible interstitial jumps. The results are compared with the activation energies calculated with LinCoSS. The relative errors in diffusion coefficient at 300 K around an edge and a screw dislocation are shown in fig. 4.4. In this figure, the maximum error of the calculation results within each square cylinder of $0.1 \text{ nm} \times 0.1 \text{ nm}$ is presented. As expected, the error near the dislocation line is particularly large. Whereas the high error region is circular around the screw dislocation, it is rather elliptic around the edge dislocation and more pronounced in the compression zone (upper half of the simulation box). In order to better understand this result, we look at

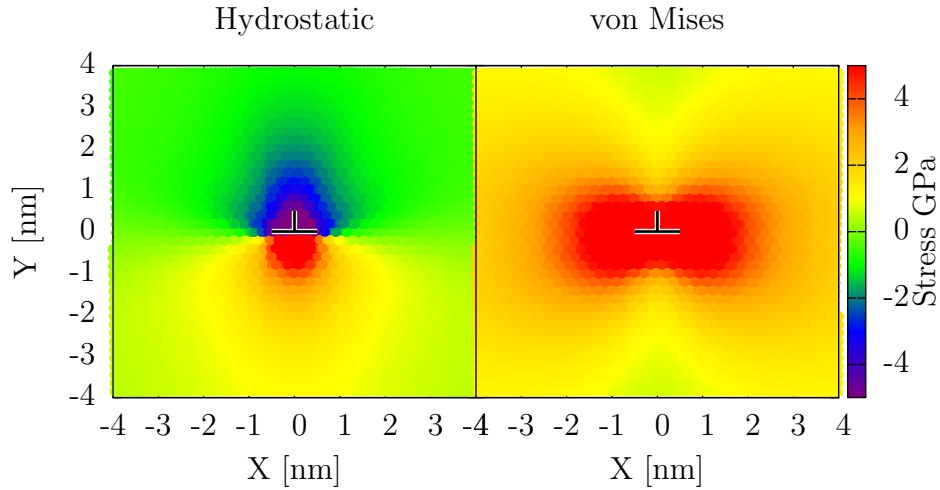


Figure 4.5: Hydrostatic and von Mises stress around an edge dislocation.

the hydrostatic stress σ_h and the von Mises stress σ_v , which are defined as:

$$\sigma_h = \frac{\sigma_{xx} + \sigma_{yy} + \sigma_{zz}}{3} \quad (4.3)$$

$$\sigma_v = \left(\frac{(\sigma_{xx} - \sigma_{yy})^2 + (\sigma_{yy} - \sigma_{zz})^2 + (\sigma_{zz} - \sigma_{xx})^2}{2} + 3(\sigma_{xy}^2 + \sigma_{xz}^2 + \sigma_{yz}^2) \right)^{\frac{1}{2}} \quad (4.4)$$

σ_h and σ_v each accounts for the uniaxial stress and the shear stress, respectively. σ_h and σ_v around an edge dislocation are shown in fig. 4.5. Comparing the figs. 4.5 and 4.4, we can see that the error is particularly high in the zone with high shear stress and strong compression.

As so far no sufficiently fast computational technique has been found to calculate activation energies that can be incorporated into AKMC for the investigation of Cottrell atmosphere formation, it is crucial to possibly lower the error of LinCoSS. There are three possible explanations that are suggested for the origin of the error.

1. The stress gradient was not taken into account in the conception of LinCoSS, whereas it may affect the activation energy around dislocations.
2. It was assumed that the activation energy given by CI-NEB is a continuous function. The reliability of the values obtained, however, has not been examined for strong matrix deformation.
3. LinCoSS is based on the approximation of the Taylor expansion of degree 2,

i.e. of the form

$$E(\vec{\sigma}) = E(0) + \sum_i \frac{\partial E}{\partial \sigma_i}(0) \sigma_i + \sum_i \frac{\partial^2 E}{\partial \sigma_i^2}(0) \sigma_i^2$$

with $i = xx, yy, zz, xy, xz, yz$. However, cross terms such as $\sum_{i,j} \frac{\partial^2 E}{\partial \sigma_i \partial \sigma_j}(0) \sigma_i \sigma_j$ ($i \neq j$) are not taken into account.

An investigation into these three possible sources of problems leads to the conclusions (A detailed description can be found in appendix D):

1. The stress gradient does not play an important role.
2. CI-NEB gives a small number of irregular activation energies, but it is unlikely that this explains the entire error regions around an edge and a screw dislocation.
3. As a function of certain combinations of two stress components, the Raulot-Becquart interatomic potential (RB-potential) gives a non-smooth behaviour in a high stress region \implies This behaviour cannot be taken into account by a polynomial approximation.

A further investigation into the possibility to take the third point into account (non-smooth behaviour), by calculating a polynomial approximation by region showed that the error in activation energy calculated through LinCoSS is reduced near the dislocation line. Yet, the error zones given in fig. 4.4 are not reduced. Therefore, the original LinCoSS is used for the activation energy calculation in the AKMC calculations in the zones parametrized by:

$$\left(\frac{x}{4}\right)^2 + \left(\frac{y}{2}\right)^2 > 1 \text{ nm} \quad \text{Edge} \quad (4.5)$$

$$x^2 + y^2 > 1 \text{ nm} \quad \text{Screw} \quad (4.6)$$

These zones (*cf.* fig. 4.6) are still smaller than the fully saturated Cottrell atmospheres presented in the previous chapter (*cf.* figs. 3.7 and 3.8). The zones, in which LinCoSS is not used to calculate activation energies are called “Ecto-LinCoSS” zone hereafter.

4.2.1 Treatment of the ecto-LinCoSS zone

The ecto-LinCoSS zone has following aspects:

1. It is a relatively small region (3.6 % of entire AKMC zone for edge dislocation and 0.4 % for screw dislocation).

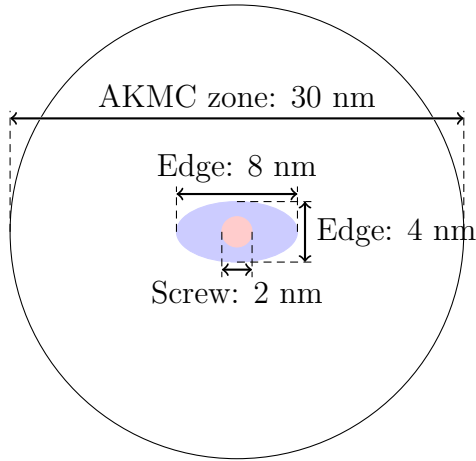


Figure 4.6: Zones for edge (blue) and screw (red) dislocation in which LinCoSS is considered to not be able to deliver a correct activation energy. The size proportion of the simulation box to the two zones is factual. Parametrizations are given in eqs. (4.5) and (4.6)

2. Attractive force of the dislocation is particularly strong \implies the C atoms are absorbed quickly into the core in this zone and it is not very likely that they come out of this region.

These points lead to the assumption, that the C atoms that arrive in the ecto-LinCoSS zone can be considered “trapped” in this zone and therefore it has no effect on the saturation kinetics of the Cottrell atmosphere anymore. It is, however, important at each stage of atmosphere evolution that the C atoms within the atmosphere affect elastically and chemically, *i.e.* they should alter the global stress field and interact with C atoms in AKMC. Therefore, the C atoms that arrived should be placed around the dislocation according to the Boltzmann distribution. This can be realized via MMC from the previous chapter. In particular, whenever the atmosphere reaches the level of saturation that corresponds to an atmosphere that was created via MMC, the core region is replaced by the core that is prepared in advance. The entire scheme is given by the following steps:

1. Start AKMC.
2. Whenever a C atom arrives in the ecto-LinCoSS zone, remove this C atom from the simulation.
3. When the number of C atoms inside the core region¹ surpasses the number of C atoms in the same area of the atmosphere prepared in advance, insert this atmosphere to replace the old core.

were the stress field is calculated in the MMC simulation is used after the insertion of the core, *i.e.* the stress field created by the atoms, which are in the AKMC zone but not in the core region, is omitted.

¹The core region corresponds to the ecto-LinCoSS zone at first, and grows along with the evolution of the Cottrell atmosphere. The precise definition of the core zone is to be determined for every stage of atmosphere evolution.

4.3 Chemical correction

LinCoSS calculates the activation energy using the local stress field, but does not take the direct chemical interactions between C atoms into account. During the Cottrell atmosphere formation, however, the C concentration will be high enough for C atoms to be within short distances even far from the dislocation line. This prompts to calculate the activation energies considering also the C-C interactions. In the current form, the calculation of chemical interaction cannot be directly integrated into LinCoSS. However, supposing LinCoSS accounts for the mechanical interaction, it is reasonable to consider that the difference between the activation energies calculated via CI-NEB and LinCoSS corresponds to the chemical interaction, since CI-NEB takes both chemical and mechanical interactions into account. We further assume that the chemical interactions solely depend on the arrangement of C atoms and not on the local stress. Since there is only a limited number of possible configurations for two C atoms within a short distance of chemical interaction reach, the calculation all of their activation energies in a bulk is viable, which are then saved in a library. Then, whenever there are two C atoms during an AKMC simulation, the chemical interactions can be looked up from this library and added to the activation energies calculated through LinCoSS. The creation of this library is performed following these steps:

1. Create a simulation box with $15 \times 15 \times 15$ lattices.
2. Insert two C atoms C_0 and C_1 into the simulation box.
3. Calculate activation energies E^{NEB} for C_0 via CI-NEB.
4. Remove C_0
5. Calculate the local stress around $C_0 \implies$ calculation of activation energies E^{Lin} by LinCoSS.
6. Save the difference $\Delta E^{\text{chem}} = E^{\text{NEB}} - E^{\text{Lin}}$

This procedure is repeated until all the configurations for two C atoms within a distance of 1.43 nm (= 5 lattices) are tested, which is the cutoff distance of the potential employed [Becquart *et al.*, 2007], while the symmetric configurations are taken into account (*cf.* fig. 4.7). A more precise description of this procedure is given in appendix E.

It is, however, possible that over the course of an AKMC simulation one C atom finds two or more neighboring C atoms within a distance of 1.43 nm. In this

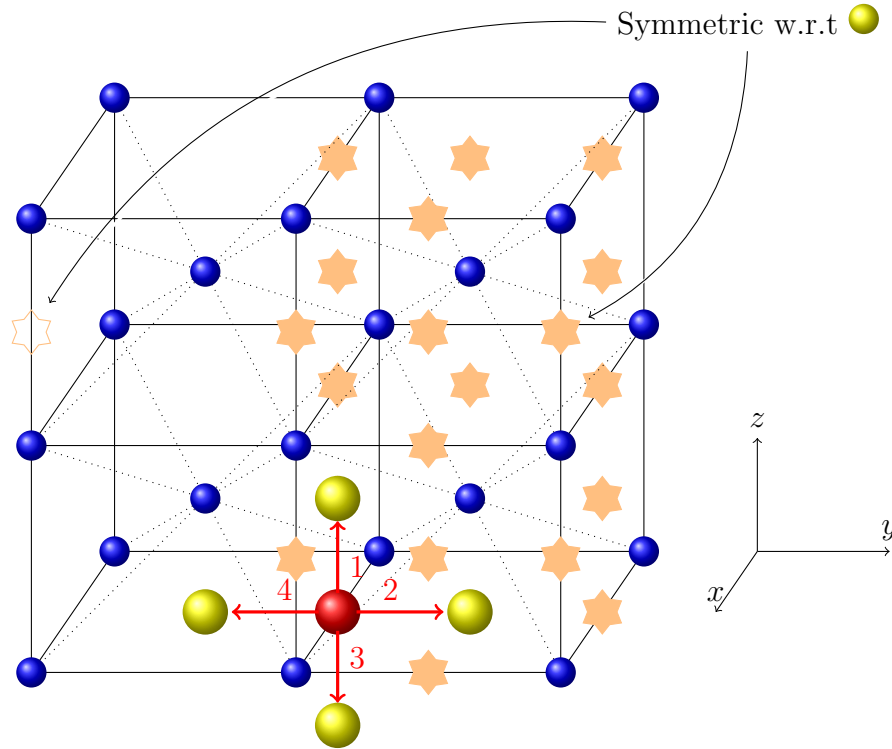


Figure 4.7: How the library of chemical interactions is created. For the different positions of the neighboring C atom (yellow stars), the four activation energies of the C atom (in red) are calculated and saved in an array.

case, the sum of chemical corrections is used as the total chemical interaction. It is, however, not known whether the chemical correction is additive or not. In order to examine the additivity of chemical interactions, in an Fe bulk of $10 \times 10 \times 10$ lattices containing 3 C atoms C_0 , C_1 and C_2 is created. The chemical corrections are then obtained for C_0 for three cases: 1, only with C_1 . 2, only with C_2 . 3, with both C_1 and C_2 . Then the sum of the chemical corrections of the first two cases is compared to the chemical correction of the third case. In particular, it is performed by following steps:

1. Insert atom C_0 for which the activation energy is to calculate.
2. Insert the first neighboring C atom C_1
3. Calculate the difference between the activation energies of CI-NEB and Lin-CoSS $\Delta E_1^{\text{chem}} = E_1^{\text{NEB}} - E_1^{\text{Lin}}$
4. Delete C_1 and insertion of the second neighboring C atom C_2
5. Calculate the difference between the activation energies of CI-NEB and Lin-CoSS $\Delta E_2^{\text{chem}} = E_2^{\text{NEB}} - E_2^{\text{Lin}}$

6. Re-insert C_1
7. Calculate the activation energies of CI-NEB and LinCoSS $\Delta E_{\text{tot}}^{\text{chem}} = E_{\text{tot}}^{\text{NEB}} - E_{\text{tot}}^{\text{Lin}}$.
8. Comparison of $E_{\text{tot}}^{\text{NEB}} - (E_{\text{tot}}^{\text{Lin}} + \Delta E_1^{\text{chem}} + \Delta E_2^{\text{chem}})$ =(error with correction) and $E_{\text{tot}}^{\text{NEB}} - E_{\text{tot}}^{\text{Lin}}$ =(error without correction)

This calculation is performed for all possible configurations within a distance of 1 nm, except for distances less than 0.3 nm in order to avoid unrealistic configurations.

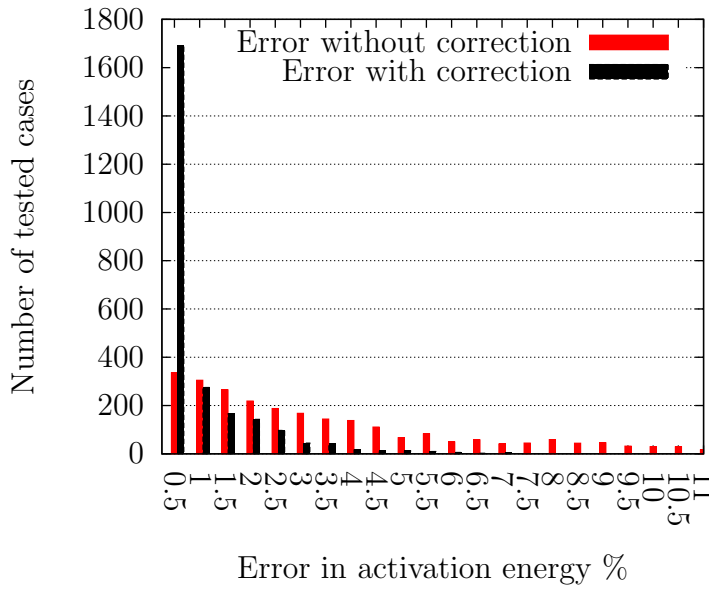


Figure 4.8: Histogram showing the activation energy errors of LinCoSS with and without chemical correction.

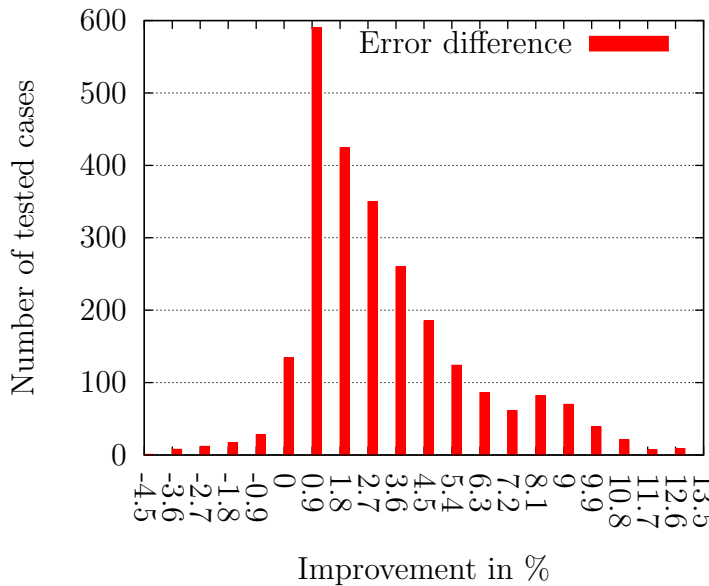


Figure 4.9: The improvement of the activation energy with chemical correction with reference to the activation energy without correction.

After eliminating configurations due to symmetry, there are 2521 possible configurations. In 67 % of the cases (1690 cases out of 2521, *cf.* fig. 4.8), the error of LinCoSS is smaller than 0.5 % with the chemical correction, which corresponds to an error of less than 20 % in diffusion coefficient at the temperature of 300 K (*cf.* fig. 4.2). Without the chemical correction, on the other hand, only in 13 % of the cases (336 out of 2521) the error of LinCoSS in activation energy is within 0.5 %. Besides, in 92 % of the configurations (2318 out of 2521), the activation energy with chemical correction is better than without chemical correction (*cf.* fig. 4.9). This means, even if the error in activation energy is higher than 0.5 %, it is still better to apply the chemical correction.

In conclusion, the library of chemical interactions, which has been developed for the interaction between two C atoms, significantly lowers the errors made by LinCoSS even with three C atoms. Even with the correction there exist configurations where activation energy error is not entirely corrected, but it is a minority of cases. Therefore, the contribution of this error to the carbon diffusion kinetics is limited.

4.4 Elastic correction

The correction described in the previous section takes only the chemical interactions into account. However, whenever there is a neighboring C atom, it does not have only a chemical effect, but it has also an elastic effect. The elastic effect, however, cannot be treated separately as it was done in the previous section, because it adds stress to the existing stress created by the dislocation. Therefore, as in the case of the chemical correction, the stress of all the possible configurations of two carbon atoms within a distance of 1.43 nm is measured.

The principle is the same as in fig. 4.7. Instead of measuring activation energies, however, solely the stress around the C atom is measured. The stress field created by one C atom is calculated and saved according to the following procedure:

1. Create a simulation box of Fe with $15 \times 15 \times 15$ lattices.
2. Put a C at (x_0, y_0, z_0) which is a z -type site \implies Relaxation of simulation box.
3. Measure stress field $\sigma_{n_x n_y n_z}^{ij}$ after relaxation, where x, y, z stand for the position of neighboring octahedral interstitial sites and $i, j = x, y, z$ in the array $(2(x - x_0)/a_0, 2(y - y_0)/a_0, 2(z - z_0)/a_0) = (n_x, n_y, n_z)$, where a_0 is the lattice parameter ($a_0 = 0.285531$ nm).

As in the case of chemical correction, it is assumed that the elastic correction is additive, *i.e.* if there is more than one neighbouring C atom or a dislocation around a C atom, the sum of the stresses is taken as the total stress. In contrast to the chemical correction, errors made through this assumption cannot be evaluated straightforwardly, since the elastic correction (additivity of the stresses of the dislocation and the neighbouring atoms) does not translates to activation energy directly. Instead of evaluating the errors in a bulk as in the case of chemical correction, therefore, it is done directly during the AKMC simulations: the activation energy of the interstitial jump that is performed at every 1,000,000 AKMC steps is compared with the activation energy calculated through CI-NEB.

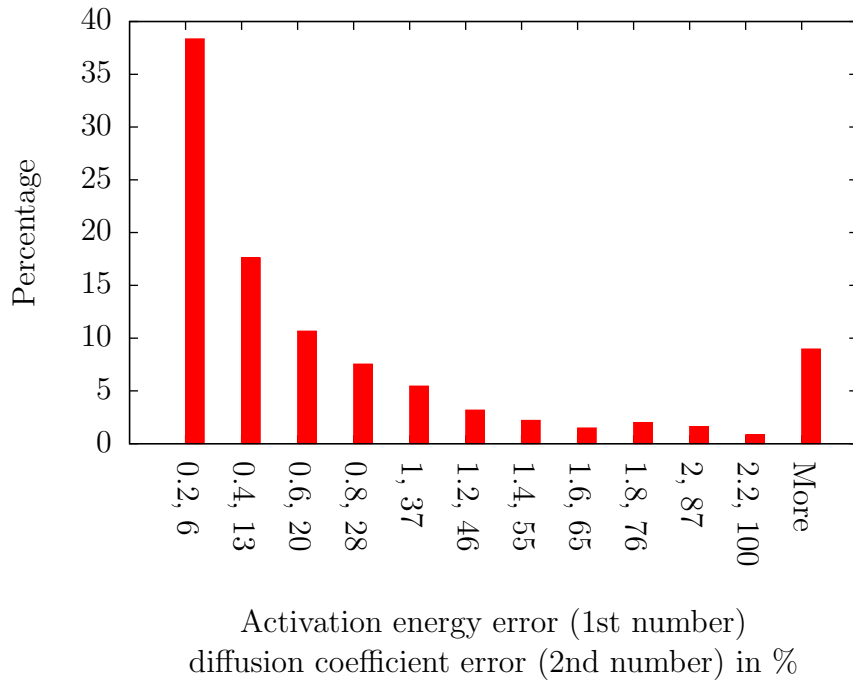


Figure 4.10: Distribution of errors in activation energy (first number of the abscissa) and in diffusion coefficient at 300 K (second number of the abscissa) as proportion of all cases. Activation energy errors of AKMC are calculated by taking the difference between CI-NEB and LinCoSS with elastic and chemical corrections (*cf.* $E_{\text{Lin}}(\sigma_i + \sum_j \Delta\sigma_j) + \sum_j \Delta E_j^{\text{chem}}$ in tab. 4.3 2. (a)).

In total, 1 000 cases were investigated. The errors in activation energy as well as in diffusion coefficient at 300 K are shown in the form of a histogram in fig. 4.10. It can be seen that in more than one third of the cases, the error of the activation energy in AKMC is less than 0.2 %, which is merely 6 % of error in diffusion coefficient. There is a substantial number of cases where the errors were significantly high. These cases, however, may have been caused through irregularity of CI-NEB that was observed in sec. 4.2.

4.5 Treatment of carbon atoms outside AKMC boundary

The activation energy calculation method involving LinCoSS, chemical correction and elastic correction that are presented in the previous section are incorporated into the AKMC. Over the course of the evolution of Cottrell atmospheres, the core region of the simulation box is replaced by the Cottrell atmospheres that are prepared in advance, in order to overcome the limit of LinCoSS. So far, however, the boundary conditions of the simulation box have not been discussed. The MMC zone of the simulation boxes that are treated in chap. 3, have a radius of 15 nm with one dislocation inside. This makes a dislocation density of $1.4 \times 10^{15} \text{ m/m}^3$, which roughly corresponds to martensite [Pešička *et al.*, 2003; Morito *et al.*, 2003; Takebayashi *et al.*, 2010]. A lower dislocation density than this, thus larger simulation box, is significantly more time-consuming for the MS and therefore it is significantly more difficult to create Cottrell atmospheres in advance via MMC. On the other hand, the stress outside this region is relatively small, so that we can consider that the carbon diffusion is not strongly affected by the dislocation core. This gives rise to the creation of a space outside the AKMC zone which C atoms can enter when they step out of the simulation box and start to perform a random walk.

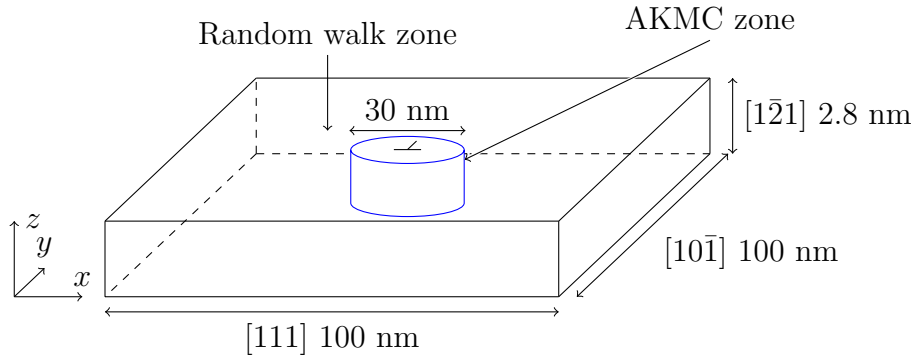


Figure 4.11: AKMC zone and random walk zone for a simulation box with 10^{14} m/m^3

Therefore, for AKMC, the simulation box is extended outside the initial cylindrical region to adjust to the desired dislocation density with periodic boundary conditions in all directions (*cf.* fig. 4.11). There is no Fe atom in the extended zone. The C atoms in this zone, therefore are not in interstitial sites of Fe matrix and therefore do not have an activation energy. For this reason, instead of displacing the C atoms through AKMC, in a regular interval, each C atom i in this

extended zone are displaced by:

$$\vec{r}_i = R(t)(\cos(\phi_i(t))\vec{e}_x + \sin(\phi_i(t))\vec{e}_y) \quad (4.7)$$

where the angle $\phi_i(t)$ is chosen randomly between 0 and 2π at each step for each atom and the $R(t)$ gives the amplitude of displacement at the time point t . There is no displacement in the z -direction, since the movement in the z -direction in the random walk zone has no contribution to the formation of Cottrell atmospheres. The amplitude R has to be determined in such a way that the timescale in the random walk zone is the same as inside the AKMC zone. According to the diffusion equation, the mean square displacement $\Delta r_i(t)^2$ of atom i at the time point t is given through:

$$\Delta r_i(t)^2 = 4Dt \quad (4.8)$$

where D is the diffusion coefficient. AKMC gives discrete time steps, namely $t = \sum_j t_j$. Since $\phi_{ij} = \phi_i(t_j)$ is taken randomly between 0 and 2π , we calculate $\Delta r_i(t)^2$ via:

$$\Delta r_i(t)^2 = \left\langle \left| \sum_j R(t_j)(\cos(\phi_{ij})\vec{e}_x + \sin(\phi_{ij})\vec{e}_y) \right|^2 \right\rangle \quad (4.9)$$

$$= \frac{\int \cdots \int \left(\sum_j R(t_j)(\cos(\phi_{ij})\vec{e}_x + \sin(\phi_{ij})\vec{e}_y) \right)^2 d\phi_{i1} \cdots d\phi_{in}}{\int \cdots \int d\phi_{i1} \cdots d\phi_{in}} \quad (4.10)$$

$$= \sum_j R(t_j)^2 \quad (4.11)$$

By inserting eq. (4.11) into eq. (4.8) we obtain

$$\sum_j R(t_j)^2 = 4D \sum t_j \quad (4.12)$$

Therefore, the amplitude $R(t_j)$ at each step can be given by $R(t_j) = \sqrt{4Dt_j}$. The random displacement of C atoms in this random walk zone is performed with a frequency of $4D/(1 \text{ nm}^2)$.

To verify this method, a simulation box with $20,000 \times 20,000 \times 1 \text{ nm}^3$ is created and 1.7×10^6 particles are inserted in one side of the box randomly (*cf.* fig. 4.12 $t = 0$). Then the particles are displaced according to eq. (4.8) with eq. (4.12), where $D = 1.0 \text{ nm}^2/\text{s}$ was chosen. The behavior of the concentration profile $c(x, t)$

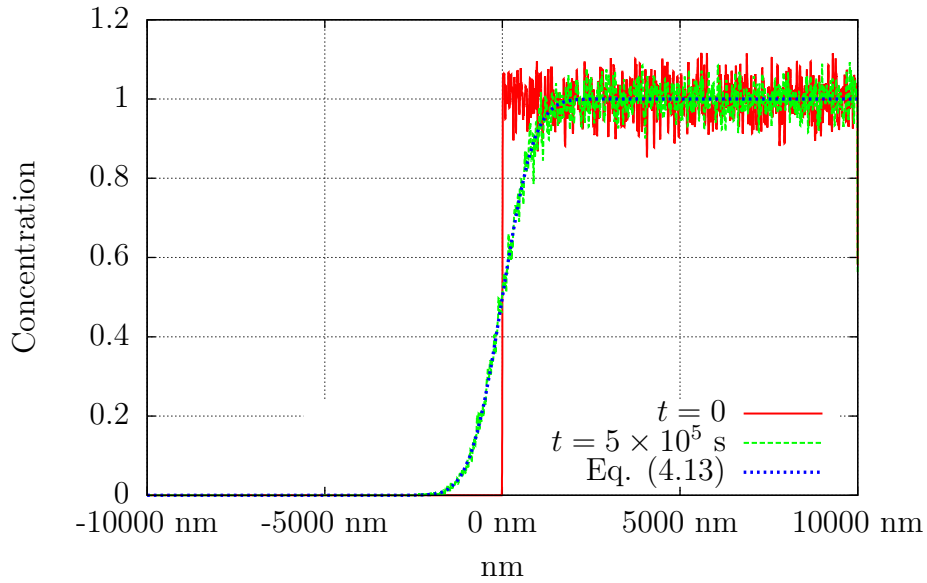


Figure 4.12: Distribution of C atoms before and after diffusion in a simulation box in which C atoms perform a random walk.

is known to be:

$$c(x, t) = c_0 \left(1 + \operatorname{erf} \left(-\frac{x}{\sqrt{4Dt}} \right) \right) \quad (4.13)$$

where erf is the error function. Fig. 4.12 shows that this analytical calculation perfectly corresponds to the concentration profile given through simulation.

4.6 Final scheme of AKMC

In tabs. 4.1 and 4.2 the different zones and the lists are presented, that sum up the discussions given so far in this chapter and allow to understand the global scheme of the AKMC simulation. The zones are defined with respect to the box dimension. The AKMC zone and the Core zone overlap, if the atmosphere surpasses the dimension of the ecto-LinCoSS zone. For the sake of simplicity, the core region is defined as a cylinder of 4 nm in radius up to the concentration of 0.059 at.% (which corresponds to 100 C inside the AKMC zone for the edge dislocation) and for higher C contents, it is a cylinder of 8 nm in radius. The AKMC list and the RW list are defined according to their zones. The atoms that arrive in the ecto-LinCoSS zone do not interact with other atoms anymore. The atoms in the pre-atmosphere list, on the other hand, may interact with the atoms in the AKMC list, but regardless of where the atoms in the pre-atmosphere list are, they are not included in the AKMC list and therefore do not move.

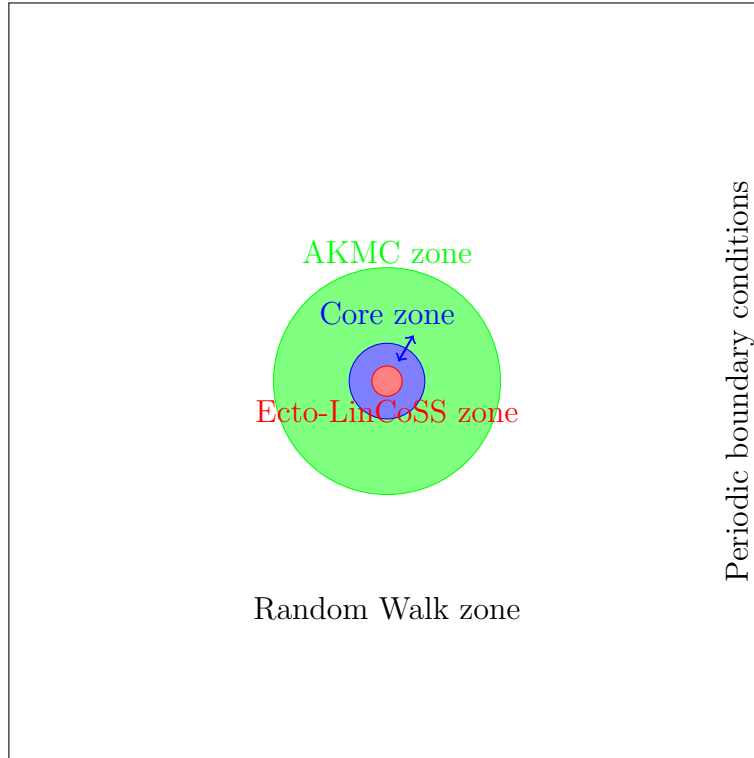


Figure 4.13: Different zones listed in tab. 4.1.

AKMC zone	Zone in which activation energies can be calculated and therefore AKMC is performed.
Core zone	Cylindrical region considered to be the core of the atmosphere, for which the radius changes following the atmosphere evolution. The number of C atoms that arrived in this region is counted for the replacement of the core with the ones prepared in advance through MMC.
Random Walk (RW) zone	Zone in which atoms perform random walks.
Ecto-LinCoSS zone	Zone in which LinCoSS does not deliver a correct activation energy. C atoms that arrive in this zone are removed from the AKMC list. This zone is included inside the core zone.
Neighbor zone of atom i	A spherical zone of 1 nm around the atom i .

Table 4.1: List of zones during the AKMC simulation

The final scheme is given in tab. 4.3.

AKMC list	Atoms in AKMC
Ecto-LinCoSS list	Atoms that arrived in the ecto-LinCoSS zone
RW list	Atoms in the RW zone
Pre-atmosphere list	Atoms that are inside the Cottrell atmosphere, that are inserted over the course of the atmosphere evolution
Update list	Atoms for which current activation energies must be updated/calculated

Table 4.2: List of lists during the AKMC simulation

4.7 Results

The AKMC simulations are launched for an edge dislocation with the thermodynamic parameters (temperatures, C contents, dislocation densities) that are found in the work of Lavaire *et al.* [Lavaire *et al.*, 2001] on thermoelectric power, and the work of De *et al.* [De *et al.*, 2000] on yield stress increase. The parameters are given in tab. 4.4. For each measurement, 16 simulations are launched and the average is taken.

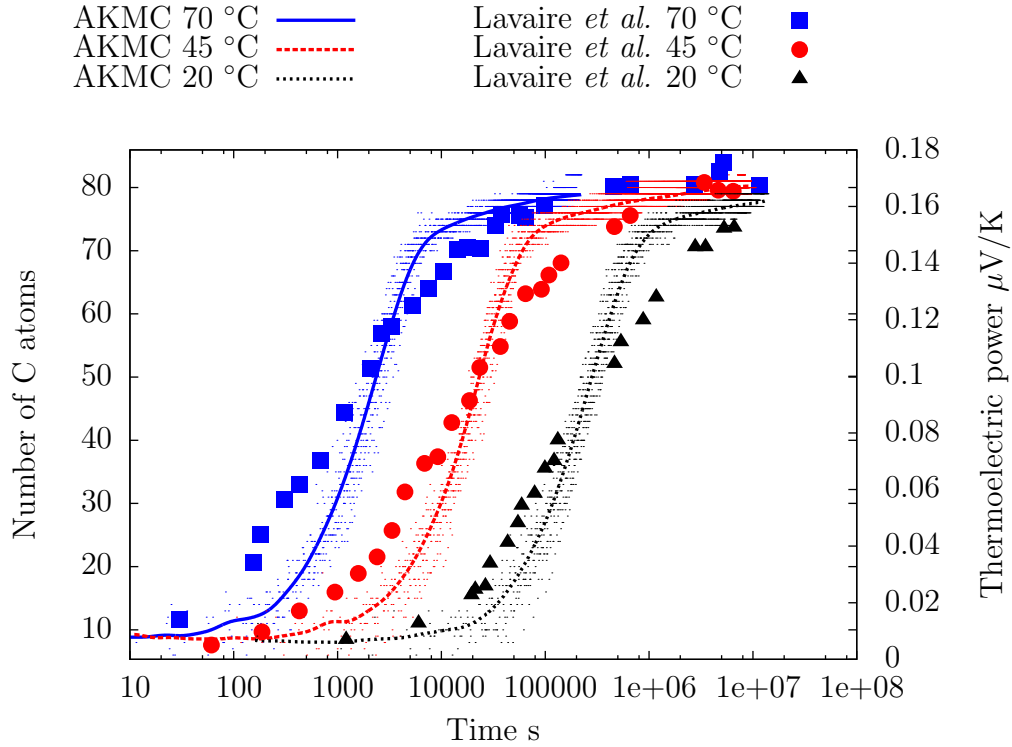


Figure 4.14: Evolution of number of C atoms that arrived in the core zone (left axis) and the evolution of thermoelectric power [Lavaire *et al.*, 2001] (right axis) as a function of time.

1. Initialization
 - (a) Creation of simulation box and insertion of C atoms at random positions
 - (b) Allocation of C atoms into different lists
 - (c) All atoms in the AKMC list added to the update list
2. Calculation of activation energies E_i , $i \in \{\text{AKMC list}\}$
 - (a) if $\exists \vec{r}_j \in \{\text{Neighbor zone of } i\} \implies E_i = E_{\text{Lin}}(\sigma_i + \sum_j \Delta\sigma_j) + \sum_j \Delta E_j^{\text{chem}}$
 - (b) else $E_i = E_{\text{Lin}}(\sigma_i)$
3. AKMC
 - (a) Choose $k \in \{\text{update list}\}$, which performs an interstitial jump
 - (b) Calculate time increment Δt via AKMC
 - (c) Displace $\forall m \in \{\text{RW list}\}$
4. Listing
 - (a) Treatment of atom k
 - i. If $\vec{r}_k \in \{\text{Ecto-LinCoSS zone}\} \implies k$ to the Ecto-LinCoSS list
 - ii. Else if $\vec{r}_k \in \{\text{RW zone}\} \implies k$ to the RW list
 - iii. Else k to the update list
 - (b) If $\exists \vec{r}_l \in \{\text{Neighbor zone of } k\} \implies k$ to the update list
 - (c) If $\exists m \in \{\text{RW list}\}$ with $\vec{r}_m \in \{\text{AKMC zone}\} \implies m$ to the AKMC list and the update list
5. Convergence check
 - (a) if $\# \text{ C atoms} \in \{\text{Core region}\} = N_{\text{Convergence}} \implies \text{Change core}$
 - i. Remove all C atoms within radius r_c
 - ii. Insert C atoms from the prepared atmospheres
 - iii. Add all inserted atoms into the pre-atmosphere list
 - (b) if $\# \text{ C atoms} \in \{\text{AKMC list}\} = 0 \implies$ iteratively increment time by $t = a_0^2/4D$ and displace atoms in the RW list, until one of them arrive in the AKMC zone
6. Back to 2

Table 4.3: Final scheme of AKMC. \exists stands for “there is”. \forall stands for “for all”.

Fig. 4.14 shows the evolution of number of C atoms that arrived in the core region via AKMC and the evolution of thermoelectric power (*cf.* Lavaire *et al.* [Lavaire *et al.*, 2001]). Since the total number of C atoms in this simulations

	Lavaire [Lavaire <i>et al.</i> , 2001]	De [De <i>et al.</i> , 2000]
Temperature	20, 45 and 70 °C	50, 75, 100 and 140 °C
C content	0.004 wt.%	0.002 wt.%
Dislocation density	10^{15} m^{-2} [Lavaire, 2001; Khatirkar <i>et al.</i> , 2012]	10^{14} m^{-2} [De <i>et al.</i> , 1999]

Table 4.4: Parameters of the materials used in the works of Lavaire *et al.* [Lavaire *et al.*, 2001] and De *et al.* [De *et al.*, 2000]. The dislocation densities are estimated following the indicated references.

was 89 (among the atmospheres prepared in advance, the one with the smallest number of C atoms in the simulation box for an edge dislocation was 80), the replacement of the core is not performed. Obviously, this affected the saturation stage of the atmospheres, which arrives earlier in the AKMC simulations than for the thermoelectric power measurement, since the C atoms that arrive in the ecto-LinCoSS zone in the AKMC simulations cannot leave this zone, whereas this would most likely occur in reality. At the same time, it can be seen that the rise of the thermoelectric power starts faster than in the AKMC simulations. This is probably due to the difference in what thermoelectric power and AKMC consider as “evolution of ageing”: the thermoelectric power rises as soon as there is an aggregate of C atoms. This implies that the effect of ageing in the early stages is provoked through the C atoms that were in the direct vicinity of the dislocation core, with a very small number of C atoms. In the case of AKMC, on the other hand, the number of C atoms that arrive in a certain area is considered for the evolution of ageing. This means that it cannot investigate the effect that might be created inside this area, since the number of C atoms within this area does not change. Therefore, the effect of ageing in the early stages in AKMC is provoked only by the C atoms that are near the dislocation line, but not in its direct vicinity. Globally, however, the variation of the number of C atoms in the core region roughly corresponds to the variation of the thermoelectric power.

As the total number of C atoms in the simulation box is higher (223) for the case of a comparison with the work of De *et al.* [De *et al.*, 2000], the core was replaced when there were 80, 100 and 150 C atoms inside the core zone. The results are given in fig. 4.15. This obviously had an effect on the saturation behavior of the Cottrell atmospheres, since the evolution slows down significantly when the core is replaced with 150 C atoms inside (indicated by the uppermost green line in fig. 4.15).

Since the fluctuations of the experimental results are very strong, it is difficult

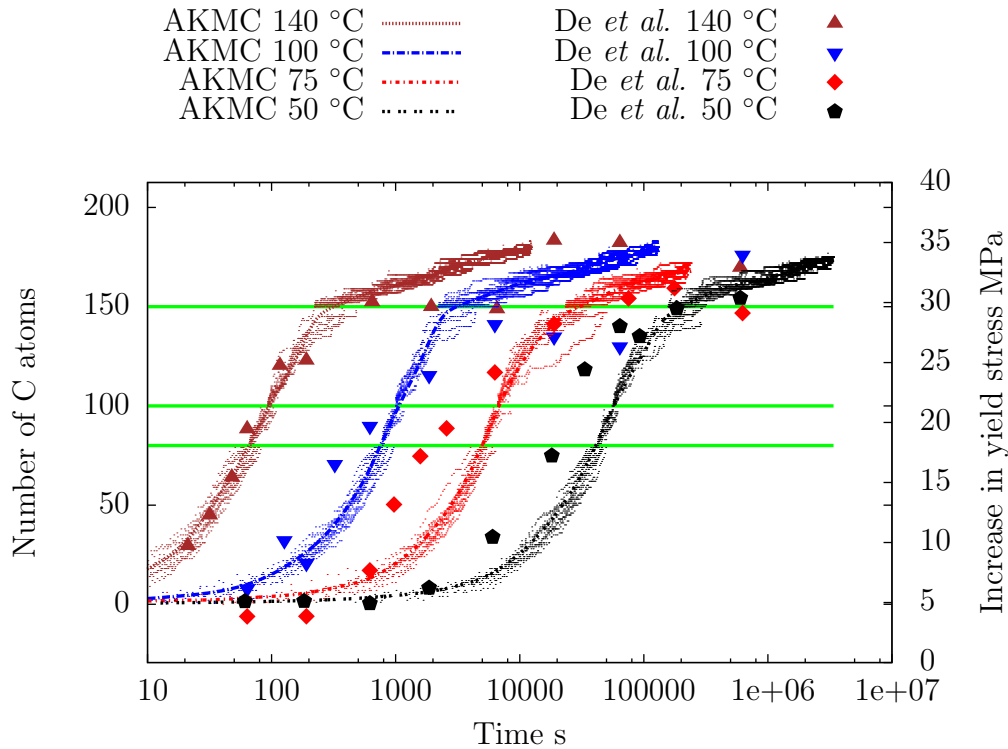


Figure 4.15: Evolution of number of C atoms that arrived in the core zone (left axis) and the evolution of yield stress [De *et al.*, 2000] (right axis) as a function of time. With 80, 100 and 150 C atoms in the core zone (indicated by green lines) the atmospheres are replaced.

to make an assertive claim on the results, but overall, the AKMC results followed well the experimental results. For lower temperatures, the atmosphere evolution is slightly slower for AKMC. This may be because the assumption of linearity between the number of C atoms inside the Cottrell atmosphere and the yield stress is not correct, since it has been previously shown that the number of C atoms required to lock the atmosphere is very low [Veiga *et al.*, 2015; Wilson and Russell, 1960]. Hence the yield stress variation may not be proportional to the variation of the number of C atoms inside the Cottrell atmosphere. For this, a further investigation of yield stress measurement *e.g.* through MD would be desirable.

4.8 Conclusion

In this chapter, the kinetic aspect of the Cottrell atmosphere evolution was studied using AKMC. AKMC requires the knowledge of the activation energy for all diffusion paths. This was done using LinCoSS [Tchitchekova *et al.*, 2014], that translates the local stress of each C atom into activation energy modification through

simple equations. LinCoSS, however, contained two main problems. Firstly, it does not give correct activation energies in the vicinity of a dislocation, where the stress is significantly high. Secondly, it is not capable of calculating direct C-C interactions. Since the exact region around a dislocation, in which LinCoSS is not valid, was not known, the activation energy of all interstitial paths was calculated using CI-NEB and LinCoSS. In order to improve LinCoSS, the origin of the error was discussed by suggesting a few possible explanations. In the end, it turned out that the activation energy landscape given by CI-NEB using the RB-potential was not a smooth surface when certain combinations of two stress components are simultaneously present. Whereas an improved version of LinCoSS that takes this into account improves the results, the size of the zone in which the error is significantly high did not particularly become smaller. Also, it is not known whether this rather irregular energy landscape is an artifact of the RB-potential. Therefore, the original form of LinCoSS is employed for the calculation of activation energies in the AKMC simulations. In order to cope with the zone, in which LinCoSS does not deliver correct activation energies (Ecto-LinCoSS zone), it was assumed that the binding energy in the vicinity of the dislocation line is so strong that the C atoms do not come out of this zone. Thus, the C atoms that arrive in this region are removed from the AKMC simulation. In order to have Cottrell atmospheres that correspond to the ongoing saturation level, the core region is replaced through the Cottrell atmospheres that were created through MMC in the previous chapter. For the direct C-C interactions, it was assumed that the difference between the activation energy calculated through CI-NEB and that of LinCoSS corresponds to the chemical interaction. It was also assumed that the C-C interactions depend only on the configuration of C atoms and not on the local stress. Therefore, the activation energies of all possible configurations for two C atoms were calculated through LinCoSS and CI-NEB in a bulk independently from the AKMC simulations. The differences between CI-NEB and LinCoSS (chemical corrections) were saved in the form of a library, which can be later used in the AKMC simulation whenever there is a C atom that has a neighboring C atom. Since a C atom may have more than one neighboring atom, it was examined whether the sum of chemical corrections of two C atoms corresponds to the chemical correction calculated with two C atoms at the same time. It turned out that in most of the cases a good agreement could be observed. Since the C atoms interact with each other also via local stress, a library of the same type for elastic interactions was also created.

As it is not possible to create a simulation box of an arbitrary size from the computational point of view, the simulation box is extended to give the dislocation density without containing Fe atoms in the extended zone. The C atoms in this

zone did not sit in interstitial sites but performed random walks. The magnitude of displacement is determined through the diffusion coefficient and the discrete time intervals given from AKMC, in order to synchronize the diffusion behavior in this region with the AKMC zone.

Lastly, AKMC simulations were launched with the parameters given in the experiments using thermoelectric power [Lavaire *et al.*, 2001] and yield stress measurement [De *et al.*, 2000]. As the total number of C atoms in the simulation box is lower for the former case than the number of C atoms that any of the simulation boxes prepared in advance contained, the core region is not replaced throughout the entire AKMC simulation. Therefore, the speed of saturation declines only due to the C depletion in the matrix. Assuming there is a proportionality between the thermoelectric power variation and the variation of the number of C atoms in the bulk, a comparison with the experimental results showed a good agreement at the beginning of the simulation, whereas the atmosphere is slightly more rapidly saturated in this work than in the experiment. As for the comparison with the yield stress, the core region is replaced over the course of the atmosphere evolution, which gave a better convergence behavior overall.

Since this model reproduced the saturation behaviour of Cottrell atmospheres observed in experiments using a simulation box containing an edge dislocation, further investigations are to be performed for a screw dislocation as well. It is also important to put in perspective to investigate how the number of C atoms inside a Cottrell atmosphere is related to the experimental values, such as thermoelectric power or the yield stress increase. Then, the dependence of the saturation behaviour on the C contents and the dislocation density is also to be investigated.

Chapter 5

Grain boundary stabilization by solute segregation in nanocrystalline Ni

Abstract

In this section, the Metropolis Monte Carlo scheme that was developed in the previous chapters is further applied to the investigation on the solute atom segregation of Mo or W around grain boundaries inside nanocrystalline Ni. The thermal stability of grains is then studied using Molecular Dynamics. It is shown that due to the solute atom segregation the grain boundaries are thermally stable.

5.1 Introduction

The interest in nanocrystalline materials rose in recent years for their mechanical [Bringa *et al.*, 2005; Bitzek *et al.*, 2008; Vepřek *et al.*, 1998], electrical [Wang *et al.*, 2012], magnetic and corrosion [Afshari and Dehghanian, 2009; Boylan *et al.*, 1991; Erb, 1995] properties, even further in biology [Hamad-Schifferli *et al.*, 2002; Parak *et al.*, 2003]. Nanocrystalline nickel is made by electrodeposition [El-Sherik and Erb, 1995], or consolidation of nanocrystalline powder [Weissmüller, 1996]. Despite the industrial interests, the high mechanical misfit of the grain boundaries makes pure nanocrystalline materials thermally unstable. Recently, as a way to stabilise the nanocrystal structure, it was proposed to insert immiscible solute atoms. The mismatch of crystal structure of the two elements is believed to help each other in order to compensate the configurational mismatch inside the grain boundaries [Weissmüller, 1993; Kirchheim, 2002]. Liu *et al.* [Liu and Kirchheim, 2004] showed an empirical model based on thermodynamics that describes the stability of nanocrystals due to solute atoms for Fe-P and Ni-P. Most importantly, this work showed a relation between the composite concentration and the grain size in thermal stability. The first investigation into the thermal stability of nanocrystalline materials with solute atoms by means of atomistic simulation was proposed in ref. [Detor and Schuh, 2007]. In their work, it was shown via Metropolis Monte Carlo (MMC) method by swapping Ni and W atoms that the W atoms segregate in the grain boundaries of the Ni matrix. And the thermal stability is deduced from the grain boundary energy, but they did not investigate the dynamics of grain growth. This was done in the work by Pun *et al.* [Pun *et al.*, 2015], in which they demonstrated a scheme combining MMC and MD simulations, where simulation boxes with grain boundaries with minimal energy were created with MMC, which are then heated up with MD. It showed a thermal stability of nanocrystalline systems with segregation of solute atoms in the grain boundaries. From the point of view of computational efficiency, Veiga *et al.* [Veiga *et al.*, 2015] proposed an MMC simulation scheme for the segregation of C atoms around a screw dislocation in the bcc iron, where the selection probabilities of new sites for solute atoms are biased by the distance from the dislocation core. This essentially exploited the binding energy difference of C atoms that is lower near the dislocation core. This scheme made it possible for the time-consuming MMC simulations to converge within a reasonable amount of time.

In this chapter, we propose a scheme, that applies the MMC method developed in chap. 3 to the investigation of the grain boundary segregation of small number of W or Mo atoms in nanocrystalline Ni. An accelerated MMC scheme is developed

to allow the simulations to converge within a reasonable amount of time. After attaining the equilibrium state, the thermal stability of the grains of the simulation boxes obtained through MMC is studied using MD at the temperature of 1,000 K up to 1 μ s. It is shown that from a certain amount of solute concentration, the grains stay thermally stable.

5.2 Computational approach

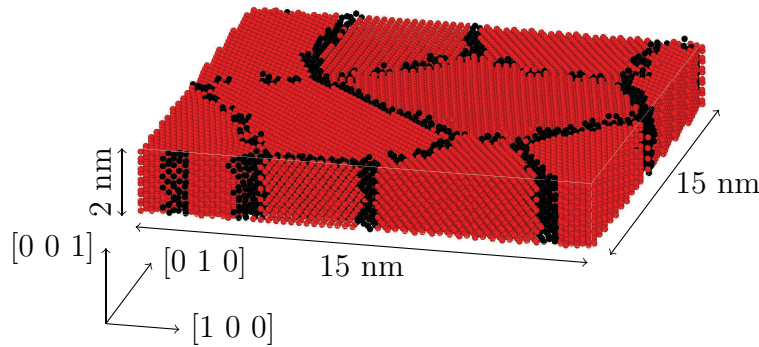


Figure 5.1: Simulation box with grain boundaries. Red spheres represent atoms in FCC structures. Atoms in grain boundaries are in black.

The simulation box used in this work consists of nanocrystalline fcc Ni with a volume of approximately $15 \times 15 \times 2 \text{ nm}^3$ containing 42024 atoms in periodic boundary conditions in all three direction. Six columnar grains with a [001] texture are generated with a Voronoi tessellation approach (*cf.* fig. 5.1). The alloying elements (Mo, W) are then distributed randomly in the simulation box by replacing the existing Ni atoms. Then the pressure of the entire simulation box is minimized using the conjugate gradient (CG) method. The simulations are launched for solute atom concentrations ranging from 0.1 at.% to 1 at.% with 0.1 at.% step for both Mo and W. In this work, we considered Ni alloys with concentrations of the alloying elements below 1 at.%, since the corresponding equilibrium diagrams of Ni-W and Ni-Mo, these concentrations are given in a single phase for which W and Mo are in solid solution.

5.2.1 Interatomic potential

The interatomic potential used for Ni-Mo was developed by Zhou *et al.* [Zhou *et al.*, 2004]. This potential was fitted to basic material properties such as lattice constants, elastic constants, bulk moduli, vacancy formation energies, and sublimation energies. The interactions for the Ni-W system was modelled through a Finnis-Sinclair potential optimized for Ni-W [Kong *et al.*, 2002]. This potential has been used previously to investigate the grain growth inhibition by the W

atoms in Ni nanocrystal [Detor and Schuh, 2007] and showed a good segregation energy of W atoms in the grain boundaries.

5.2.2 Metropolis Monte Carlo

An MMC step is performed according to following scheme: 1. Measurement of the potential energy of the current state E_o . 2. Random selection of one alloying atom. 3. Selection of one Ni atom according to the selection probability w_i . 3. Swapping of the selected atoms. 4. Energy minimization and calculation of the new potential energy E_n . 5. Acceptance or rejection of the new state according to the acceptance probability p . 6. Back to the step 1.

The selection probability w_i of selecting the Ni atom i is calculated as $w_i = \exp(\mu|E_i^{int}|)/W$, where μ is the parameter that determines the strength of the bias, E_i^{int} is the interaction energy of the atom i and $W = \sum_j \exp(\mu|E_j^{int}|)$. The interaction energy E_i^{int} for atom i is calculated by taking the difference of potential energy between the pure Ni simulation box with grain boundaries (*cf.* fig. 5.1) and the simulation box from which the atom i is removed. This makes the probability of choosing an Ni atom in the grain boundaries higher, since the interaction energy with the neighbouring atoms is higher for those which are in the grain boundaries. This bias is compensated at the acceptance/rejection step, as the probability p to accept the new state n is calculated as follows:

$$p(o \rightarrow n) = \min \left[1, \frac{w_o}{w_n} \exp \left(-\frac{E_n - E_o}{k_B T} \right) \right] \quad (5.1)$$

where w_o and w_n are the selection probabilities of the new and old positions, respectively.

5.2.3 Molecular Dynamics Simulation

After the convergence of the potential energy of the MMC simulations, the MD simulations are launched, for which the initial configuration is taken from the last MMC simulation snapshot. All MD simulations are performed for 500 ns (5×10^8 steps) at the temperature of 1,000 K in NPT system while the pressure in each direction is maintained at 0. For the simulation boxes containing 1 at.%Mo and 1 at.%W, the simulations were performed up to 1 μ s. At every 20 ns, a snapshot of the system was taken, which is then relaxed in order to determine the state of the grains.

5.2.4 Calculation of orientation angle

In this study, the grains are characterized through their orientation angles. For this, the tilt of the lattice associated to each atom was calculated. The frame for each atom is calculated according to following scheme. 1, Detection of 12 neighbouring atoms, where atoms within the distance of $\sqrt{3}a_0/2$ are counted as neighbours. 2, Calculation of lattice frame from the positions of the neighbouring atoms. 3, The orthonormal vectors \vec{x} , \vec{y} and \vec{z} of the frame are determined. 4, For a given lattice, the Euler angles are calculated by

$$\alpha = \arccos\left(\frac{x_2}{\sqrt{1.0 - x_3^2}}\right), \beta = \arccos(x_3), \gamma = \arccos\left(\frac{z_3}{\sqrt{1.0 - x_3^2}}\right)$$

where x_i, y_i, z_i $i \in \{1, 2, 3\}$ are the components of $\vec{x}, \vec{y}, \vec{z}$, respectively. Since grains were created by rotating around $[0\ 0\ 1]$ axis (*cf.* fig. 5.1), \vec{z} always coincides with the $[0\ 0\ 1]$ -direction. Since the fcc-lattice is symmetric with respect to a rotation of 90° , there are four possibilities to define \vec{x} . Therefore, it is taken as the vector which has the largest component in the $[0\ 1\ 0]$ -direction (*cf.* fig. 5.1). This would determine \vec{y} automatically. The atoms not having 12 neighbouring atoms are counted as being in the grain boundaries.

5.3 Results and Discussion

5.3.1 Metropolis Monte Carlo

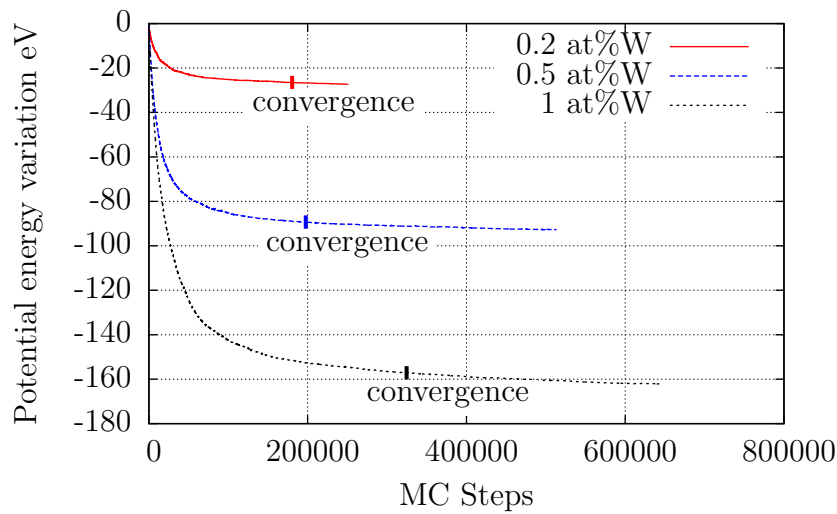


Figure 5.2: Energy convergence of MC simulations

The energy evolution of the simulations for 1, 0.5 and 0.2 at.% are shown in

figure 5.2 with the point of convergence marked for each figure, that is determined via eq. (5.2). The energy value is given with respect to the initial configuration.

It can be observed that the potential energy of the system converges exponentially, which means that the potential energy difference ΔE with respect to the initial configuration evolves as a function of MC steps N according to:

$$\Delta E(N) = E_0(1 - \exp(-kN)) \quad (5.2)$$

where E_0 and k are parameters that are obtained by fitting the function to the results via least square method. E_0 should be the difference in potential energy between the initial state and the fully converged state. We defined the energy convergence as N_{conv} which satisfies $\exp(-kN_{\text{conv}}) < 10^{-6}$. For all simulations, the MD simulation is launched once this criterion is fulfilled.

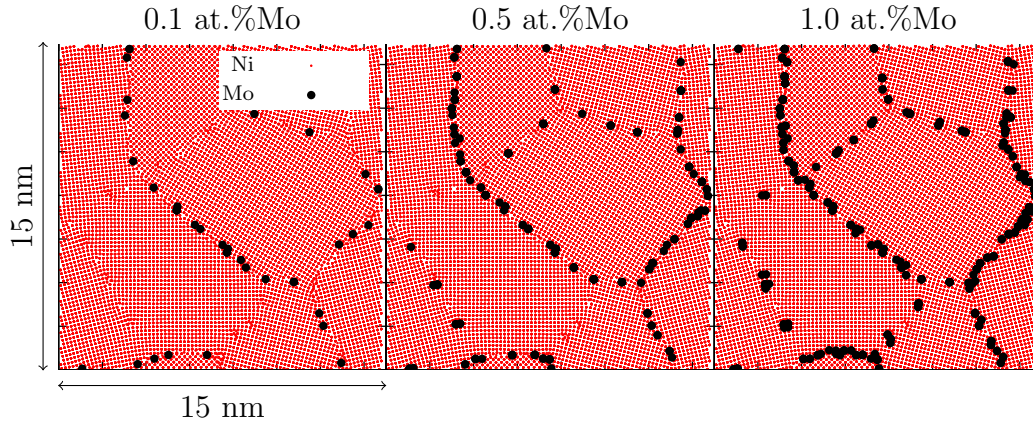


Figure 5.3: Distribution of Mo atoms in nanocrystalline Ni for 0.1, 0.5 and 1 at.%

The Mo distributions for different Mo contents are shown in fig. 5.3. The initially homogeneously distributed Mo atoms are seen to have segregated around the grain boundaries. There are grain boundaries, that are occupied preferably by the Mo atoms, and that are not.

5.3.2 Molecular Dynamics

The MD simulation results of pure nickel at 1,000 K are presented in figure 5.4. As expected, the initially clearly separated grains rapidly turned into a larger grain at 100 ns, leaving only a small slice. Eventually, the grain boundaries entirely disappeared at 200 ns.

The simulation boxes containing a certain amount of solute atoms, however, showed thermal stability over the course of the MD simulations (*cf.* figs. 5.5 and

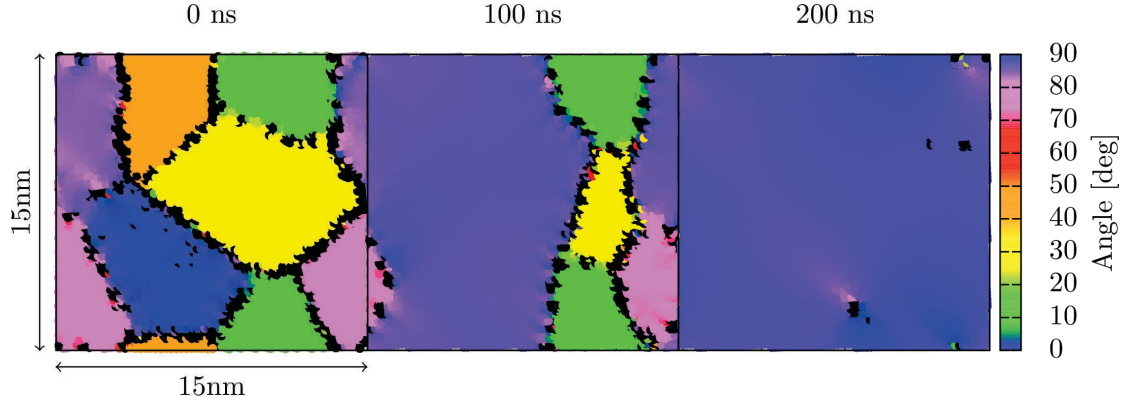


Figure 5.4: Snapshots of MD simulation results for 0, 100 and 200 ns for pure Ni.

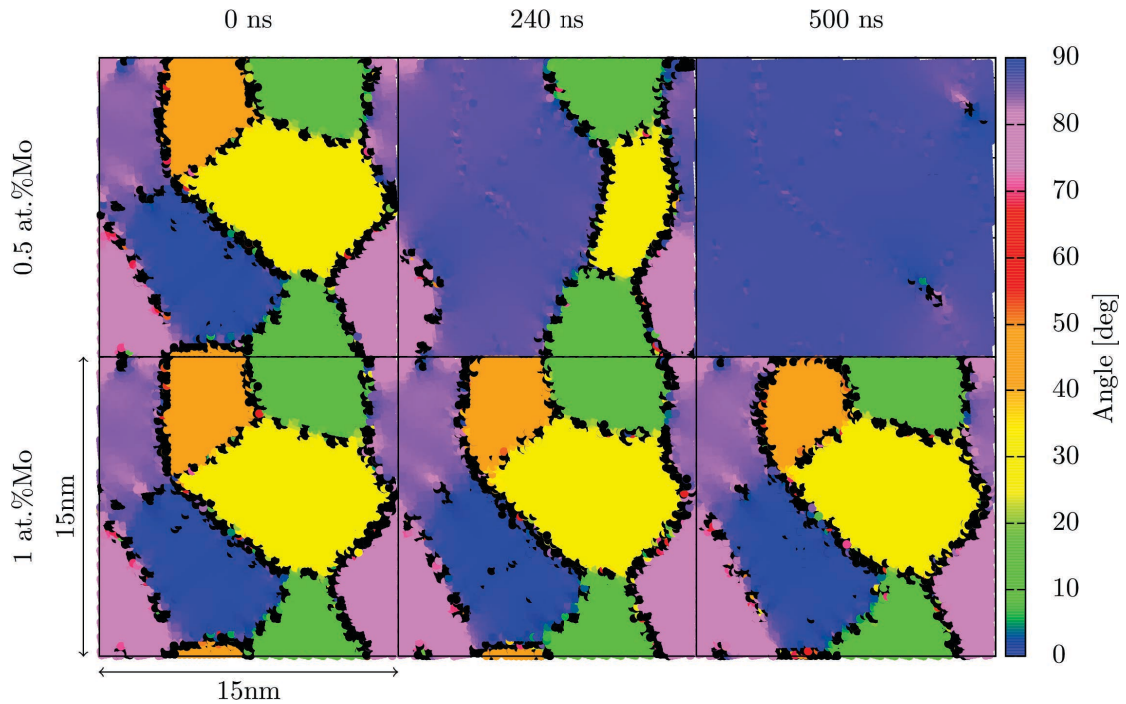


Figure 5.5: Snapshots of MD simulation results for 0, 240 and 500 ns for 0.5 and 1 at.% Mo.

5.6). The thermal stability study of both Mo and W at 1 at.% up to $1 \mu\text{s}$ showed that the grains were still stable.

The time evolution of the grains were observed taking the histogram of the angle distribution for each atom. The histogram $H(t, \theta)$, where $\theta = \alpha, \beta, \gamma$, is defined as:

$$H(t, \theta) = \left\langle \sum_i \delta(\theta - \theta_i) \right\rangle \approx \sum_i \frac{1}{\sigma\sqrt{\pi}} \exp\left(-\frac{(\theta - \theta_i)^2}{\sigma^2}\right) \quad (5.3)$$

where $\sigma^2 = 0.1$ was chosen, which gives a smooth distribution. Figs. 5.7 and 5.8 show the distribution of frame angle α of the final states of MD simulations as

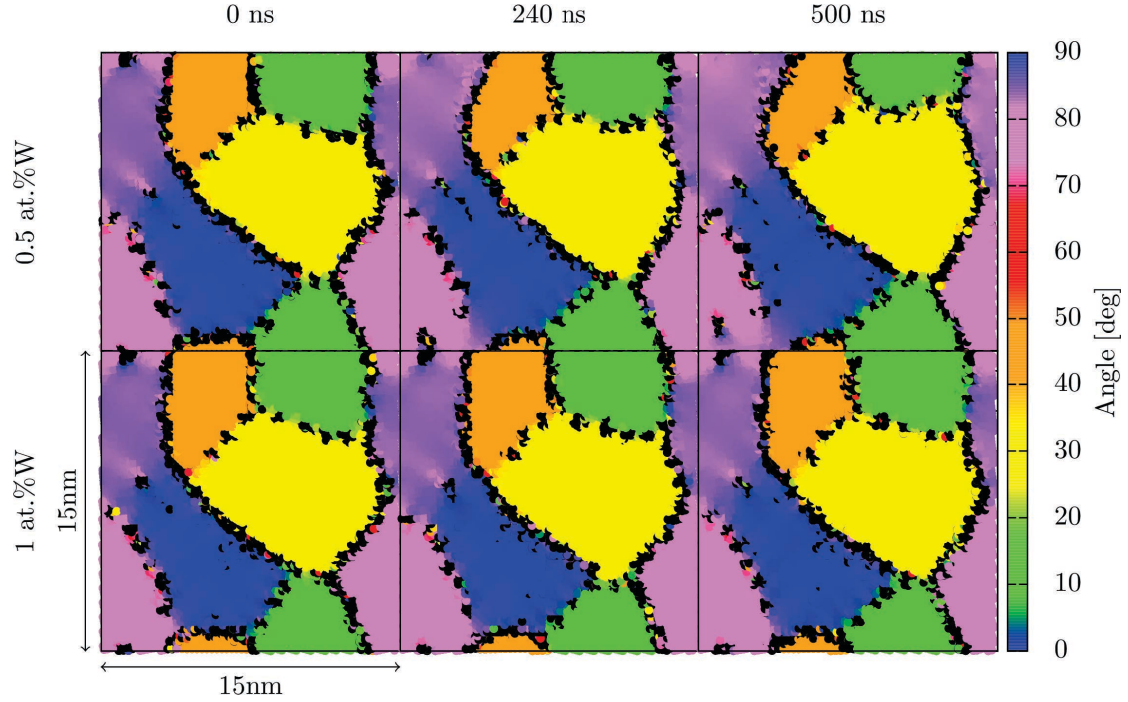


Figure 5.6: Snapshots of MD simulation results for 0, 240 and 500 ns for 0.5 and 1 at.%W.

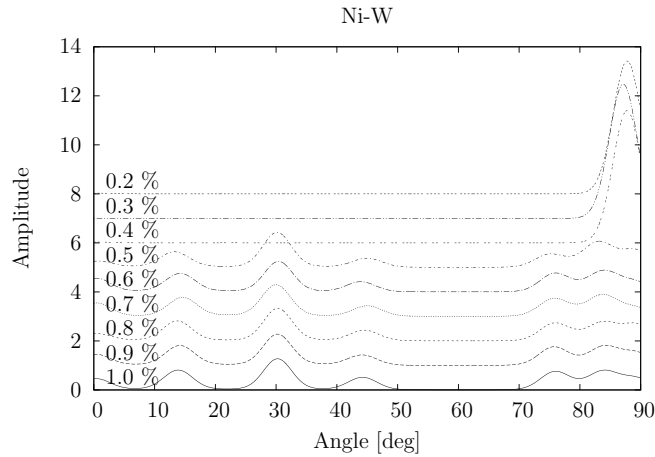


Figure 5.7: Evolution of the angle distribution of the final states of MD simulation for Ni-W.

a function of the Mo/W concentration. As expected, at higher solute contents, where the grain boundaries are thermally stable, several maxima can be seen. Below a certain solute content, only one peak can be seen. For Ni-W, the grains are stable from 0.5 at% and for Ni-Mo, it is from 0.7, showing the stronger pinning effect of W atoms in nanocrystalline Ni.

Depending on the temperature, the solute atoms are believed to move with the grain boundaries (dragging) [Gleiter, 2000]. In the simulation boxes with low solute atom concentrations, where the grain boundaries disappear, the solute atoms are found not to move far with the grain boundaries for the temperature (1,000 K) used for this study (*cf.* fig. 5.9).

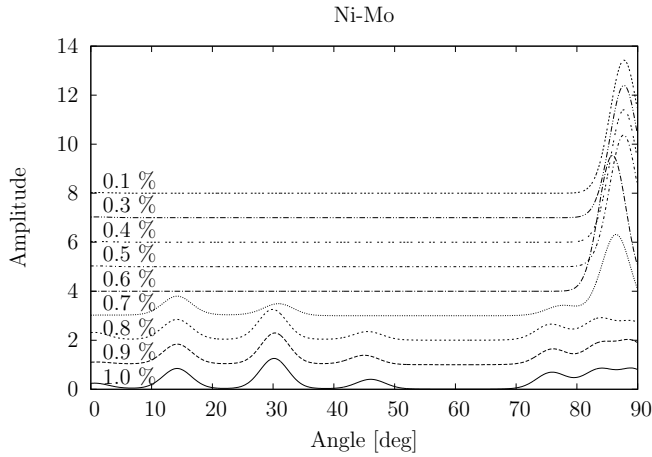


Figure 5.8: Evolution of the angle distribution of the final states of MD simulation for Ni-Mo.

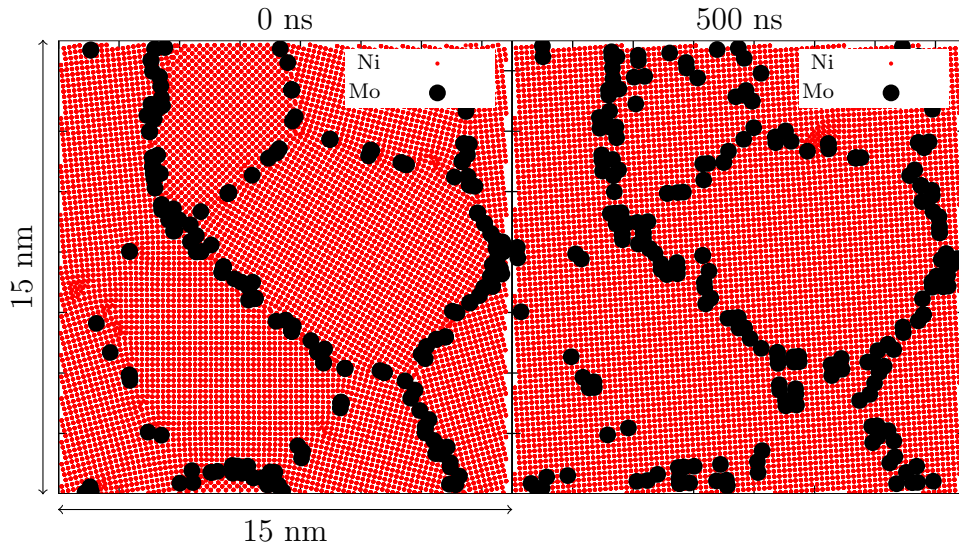


Figure 5.9: Distribution of Mo atoms for 0.6 at.% before and after the MD simulation.

5.4 Conclusions

We reported the results of a combined MC+MD simulation protocol applied to the study of grain boundary segregation and its effect on the stability of nanocrystalline Ni. An fcc Ni sample with six $[0\ 0\ 1]$ columnar grains was constructed by Voronoi tessellation. Two alloying elements, W and Mo were substitutionally added in concentrations ranging from 0.1 to 1 at.%, being initially distributed at random in the simulation box (solid solution). Energy biased on-lattice Metropolis Monte Carlo simulations performed at 350 K (typical in electro-deposition experiments [Meyers *et al.*, 2006]) were then employed to obtain segregated model alloys, in which an MMC step consisted of swapping an Ni atom and a solute atom. A segregation of solute atoms was observed through MMC simulations. This configurations were subsequently taken as the initial structures for MD simulations. MD simulations of pure Ni nanocrystal at 1,000 K revealed rapid grain growth;

the grains grew into one grain at $0.2 \mu\text{s}$. Carried out again at 1,000 K for up to $0.5 \mu\text{s}$ with solute atoms, the MD simulations showed that grain boundary segregation inhibited grain growth in the model alloys; with both Mo and W, the nanocrystalline structures were stabilized from certain solute atom concentrations, which were 0.5 at.% for Ni-W and 0.7 at.% for Ni-Mo. For simulation boxes with 1 at.%Mo and 1 at.%W, the MD simulations were performed up to $1 \mu\text{s}$ and it could be observed that the grains were still stable.

Numerical modeling at the atomic scale may become a useful and cost-effective tool in the process of tailoring materials properties, eventually guiding the experimental work. The main challenge still lies in the development of accurate interatomic potentials, which lack for many systems of interest in engineering applications.

So far, to the knowledge of the author, no experimental result has been delivered so far on the quantitative analysis of thermal stability of Ni-Mo study. After a potential comparison with experimental results, it is important to investigate the dependence of the thermal stability on the structure of nanocrystalline materials and nanocrystal size, since it is known to vary significantly [Gleiter, 2000]. In the study of this section, the same initial structure was used for all simulations, but further investigations are desired to establish a relation between the geometrical properties and the thermal stability of the systems studied in this section.

Chapter 6

Conclusion and perspectives

The investigation into steels on the microscopic level has been moving forward very rapidly with the advancement in computer technology and numerical methods. In this thesis, several numerical methods such as Metropolis Monte Carlo (MMC), Atomistic Kinetic Monte Carlo (AKMC), Molecular Statics (MS) or Molecular Dynamics (MD) have been employed, using Raulot-Becquart interatomic potential (RB-potential) [Veiga *et al.*, 2011]. After presenting the methodology in the first chapter, the thermal stability of the Zener ordering was investigated in the second chapter. This was compared with MD results and a thermodynamical calculation. The physical quantities taken into account were different for these three methods. The thermodynamical calculation takes only the elastic strain-field interactions of C atoms into consideration. MMC further takes also chemical interactions between C atoms into account. In addition to these effects, MD takes also vibrational/anharmonic effects into account. The critical temperatures given by MMC and the thermodynamical calculation were in good agreement at lower C contents, but at higher C contents, the critical temperatures given through MMC were significantly lower. By “including” the chemical interactions into the thermodynamical calculation, it could be indeed explained that the direct C-C interactions make ordered states less favorable. However, the critical temperatures given through MD were higher than those given through MMC. This effect was most likely compensated by other physical quantities such as the Young’s modulus or elastic coefficients, which are known to vary according to the temperature only if vibrational effects are also taken into account.

In the third chapter, the structure of the Cottrell atmospheres around dislocations and the effect of the Cottrell atmospheres on the stress field were investigated. For this, a simulation box containing an edge or a screw dislocation was created, in which a certain number of C atoms were inserted. These atoms were displaced according to the MMC scheme, where the box dimensions were modified

in a regular interval in order to minimize the effect of the box size. The Cottrell atmospheres corresponded to the size and maximum C density reported from experimental results. A minute investigation into its structure showed that over the saturation of Cottrell atmospheres, the stress field around the dislocation is not reduced, contrarily to the prediction made by Cottrell in his original paper. This answers one important and fundamental question about the Cottrell atmospheres, namely how a Cottrell atmosphere becomes saturated, since if the stress does not diminish, it means that the attractive force of the dislocation is still present. This makes the C-C interactions the only one possibility for the atmosphere saturation. This may slightly alter our understanding of why C atoms migrate around a dislocation: indeed, the C atoms in the Cottrell atmospheres are present due to the misfit of Fe atoms in the dislocation, but it is not the Fe atoms that attract the C atoms, but it is the C atoms that seek a refuge due to the solubility that is virtually zero in the perfect crystalline α -Fe matrix. These C atoms, therefore, end up in a dislocation, because the sites in the dislocation are “less uncomfortable” than in the ferrite matrix, thus not in order to relieve the stress, and therefore do not affect the global stress field.

After the structural aspect of Cottrell atmospheres was studied, the kinetic aspect was investigated in the fourth chapter via AKMC. Since AKMC requires the knowledge of activation energies for all interstitial paths, Linear Combination of Stress States (LinCoSS) method was employed to translate the local stress of each C atom into its activation energies. This translation process involves only a handful of equations with no lengthy iterative calculation such as MS, which would be otherwise required for Climbing Image-Nudged Elastic Band (CI-NEB) or Activation Relaxation Technique (ART). Since LinCoSS does not take chemical interactions between C atoms into account, the difference between CI-NEB and LinCoSS was saved in the form of a library, which was used in the AKMC simulations whenever there were two or more C atoms in the neighborhood. As for the vicinity of dislocation line, the kinetics of C atoms in this region was not calculated, since the binding energies of the interstitial sites in this region are so strong that the C atoms that arrive in this region would not leave it anymore. The C atoms that arrive in this region are therefore removed from the AKMC simulation. In order to have a realistic core that corresponds to the ongoing saturation level, the Cottrell atmospheres created through MMC in the previous chapter are inserted, according to the number of C atoms that arrived in the core region. The AKMC simulations were performed only in the cylindrical zone which has a dimension of 15 nm in radius and 2.8 nm in height. In the rest of the simulation box, the C atoms performed a random walk, where the amplitude of

the displacements was determined through the diffusion coefficient and the time increment given by AKMC. The simulations were launched for an edge dislocation with the same thermodynamical parameters as the experimental results based on thermoelectric power [Lavaire *et al.*, 2001] and yield stress increase [De *et al.*, 2000]. Finally, a comparison showed a good agreement between the AKMC results and the experimental data.

Apart from the Fe-C system, MMC was further applied to the composite of nanocrystalline Ni, in which the alloying atoms are known to segregate in the grain boundaries and are predicted to make the grains thermally stable. For this, Ni-W and Ni-Mo systems were investigated. After the energy minimization through MMC, segregation of alloying atoms could be observed. Then the thermal stability of the equilibrated simulation boxes was studied through MD at the temperature of 1,000 K. It could be seen that from the solute contents 0.5 at.% for Ni-W and 0.7 at.%, the grains were stable up to 500 ns. For the solute content of 1 at.%, the grains of both Ni-W and Ni-Mo were stable at the temperature of 1,000 K up to 1 μ s.

Compared with the previous investigation of Veiga *et al.* [Veiga *et al.*, 2010] on Cottrell atmospheres through AKMC, this work had two major improvements. Firstly, it allowed the C atoms to leave and enter the simulation box. Secondly, it included direct C-C interactions. This enabled two important physical quantities in the formation of Cottrell atmospheres to play a role, namely the C concentration and the dislocation density. This, again, enabled us to realize for the first time a calculation of formation kinetics of Cottrell atmosphere via AKMC which was comparable with experimental results. However, whereas the experimental investigations on the structure of Cottrell atmospheres such as via atom probe tomography often focus on a steel which contains a high amount of solute atoms, the kinetics of atmosphere formation is mostly studied with very low C concentrations and high dislocation densities. This means that the saturated Cottrell atmospheres contain very little carbon in these experiments. Accordingly, a large area of the Cottrell atmospheres does not overlap with the region in which LinCoSS is still valid. Therefore, it is crucial to extend the zone, in which we can calculate the kinetics, to truly validate our AKMC scheme. The first attempt that can perhaps be carried out is to combine LinCoSS with an MS-based method, such as CI-NEB or ART. As a matter of fact, the modified ART, Veiga-ART, first introduced in the thesis of R. Veiga [Veiga, 2011], was originally integrated into the current AKMC scheme in this thesis as well, *i.e.* it was intended to be employed in the region near dislocation line in which LinCoSS was not valid. However, due

to the overly high number of lengthy calculations to be performed to attain a fully saturated Cottrell atmosphere, the use of ART was eventually abandoned. To overcome this problem, another idea that can be tried out is to extend the polynomial approximation of LinCoSS to higher orders. As it was shown in chap. 4, it is very likely that the error of LinCoSS is significantly reduced if the stress polynomials of third order is taken into consideration as well. For this, it is important to compare the activation energies obtained using the RB potential with *ab initio* calculations first, especially to know what exactly occurs when the stress is very high and complex.

Also, the structure of dislocation core was not studied in this work, except for the C-free state of a screw dislocation, in which an easy core was observed, which is in agreement with what was previously reported [Clouet *et al.*, 2011]. Recently, it was reported using DFT calculations that the easy core transforms into a hard core configuration [Nguyen, 2009; Ventelon *et al.*, 2015], which is qualitatively reproduced with the RB potential.

Recent development in computational resources allowed several works [Khater *et al.*, 2014; Veiga *et al.*, 2015; Tapasa *et al.*, 2007] to realize an investigation into pinning force of Cottrell atmospheres on the atomistic level. In these studies, simulation boxes containing a small number of C atoms in/around a dislocation were sheared at a constant rate. Yet, these were done either in MS, in which there is no notion of time, or in MD at very high straining rate. Hence, these results cannot be directly compared to the experimental results. Provided that the activation energy of dislocation unpinning can be somehow calculated, pinning force measurement can be performed while conforming to the strain rate given by experiments, using the time evolution given by AKMC. This would be also an important step to validate the AKMC simulations of this work, since the assumption of linearity between the yield stress and the number of C atoms inside a Cottrell atmosphere has to be confirmed/refuted. Furthermore, this study may allow to observe a phenomenon such as Portevin-Le Chatelier effect, which has never been seen on the atomic level.

In the formation of Cottrell atmospheres through MMC, the octahedral interstitial sites around dislocations were occupied one by one. However, the saturated Cottrell atmospheres may evolve into a different phase, such as carbide or α' -Fe. With our current interatomic potential, carbide cannot be studied. However, a relation between the stability of α' -Fe and Cottrell atmospheres around a dislocation, or even around grain boundaries or dislocation loops may be established with the methods presented in this thesis. Moreover, by combining DFT calculations,

as recently performed by Nematollahi *et al.* [Nematollahi *et al.*, 2016], it may also be manageable to extend the scheme to carbides.

In this thesis, the interatomic potentials for the investigation on grain boundary segregation of alloying atoms and thermal stability of grain boundaries may have been used somewhat far away from their original purposes. Despite the industrial interest in regarding the same type of problem for several types of alloys, it often comes to the question of the existence of appropriate interatomic potential. Since the realization of solute atom segregation and the thermal stability study are well established, the scheme needs a major revamp to include the acquisition of interatomic potentials, *e.g.* in the form of Finnis-Sinclair potential [Finnis and Sinclair, 1984] via *ab initio*. This would enable for each topic of this type to create a complete scheme of 1, creation of interatomic potential via *ab initio*. 2, segregation of solute atoms in structural defects or precipitation via MMC. 3, thermal stability study via MD.

Appendices

Appendix A

Assessment of the order parameter via free energy calculation

The free energy or Helmholtz free energy F of a system of volume V containing n_C C atoms depends on the repartition of C atoms among the octahedral site types. Let us assume a given repartition n_C^x , n_C^y and n_C^z atoms in site types x , y and z , respectively. The free energy is given by:

$$F = U - TS \quad (\text{A.1})$$

where U is the energy of the system and S is its entropy. In the following, it is assumed that ordering occurs in z -type sites, *i.e.* there is the same amount of C atoms in x and y octahedral sites, which leads to:

$$n_C = n_C^x + n_C^y + n_C^z \quad (\text{A.2})$$

$$n_C^x = n_C^y = \frac{(n_C - n_C^z)}{2} \quad (\text{A.3})$$

Hence, n_C^z is the only free parameter of the system. Consequently, the n_C^z that gives the minimum free energy is what is looked for, which means in particular:

$$\frac{\partial F}{\partial n_C^z} = \frac{\partial U}{\partial n_C^z} - T \frac{\partial S}{\partial n_C^z} = 0 \quad (\text{A.4})$$

Therefore, the energy U is calculated below, followed by the entropy S .

It is known that the each C atom induces a macroscopic tetragonal distortion ε_{ij} on the lattice, which interacts with the distortion of other C atoms. There are three components that contribute to the total energy U , the “chemical” contribution U_0 , the elastic stored energy and the interaction energy, such that:

$$U = U_0 + \frac{1}{2}VC_{ijkl}\varepsilon_{ij}\varepsilon_{kl} - \sum_{n_C} P_{ij}^{x,y,z}\varepsilon_{ij} \quad (\text{A.5})$$

where $P_{ij}^{x,y,z}$ is the dipole tensors accounting for the tetragonal distortion of one C atom lying in x , y or z site type:

$$P_{ij}^x = \begin{bmatrix} \lambda & 0 & 0 \\ 0 & \lambda' & 0 \\ 0 & 0 & \lambda' \end{bmatrix} \quad P_{ij}^y = \begin{bmatrix} \lambda' & 0 & 0 \\ 0 & \lambda & 0 \\ 0 & 0 & \lambda' \end{bmatrix} \quad P_{ij}^z = \begin{bmatrix} \lambda' & 0 & 0 \\ 0 & \lambda' & 0 \\ 0 & 0 & \lambda \end{bmatrix} \quad (\text{A.6})$$

Since there is no shear induced by the C atoms, both $P_{ij}^{x,y,z}$ and ε_{ij} can be reduced to:

$$P_i^x = \begin{bmatrix} \lambda & \lambda' & \lambda' \end{bmatrix}, \varepsilon_i = \begin{bmatrix} \varepsilon_x \\ \varepsilon_y \\ \varepsilon_z \end{bmatrix} \quad (\text{A.7})$$

the same for P_i^y and P_i^z . The total energy is then:

$$U = U_0 + \frac{1}{2}VC_{ij}\varepsilon_i\varepsilon_j - (n_C^x P_i^x + n_C^y P_i^y + n_C^z P_i^z)\varepsilon_i \quad (\text{A.8})$$

As the total stress σ_i is given by $\sigma_i = (1/V)(\partial U/\partial \varepsilon_i)$, on a stress free sample, $\sigma_i = 0$, eq. (A.8) leads to:

$$VC_{ij}\varepsilon_j = (n_C^x P_i^x + n_C^y P_i^y + n_C^z P_i^z) \quad (\text{A.9})$$

Multiplying both sides of this equation by the compliance tensor S_{ij} leads to the expression of the macroscopic strain tensor induced by a given repartition of C atoms:

$$\varepsilon_i = \frac{1}{V}S_{ij}(n_C^x P_j^x + n_C^y P_j^y + n_C^z P_j^z) \quad (\text{A.10})$$

When shear is not accounted, the compliance tensor S_{ij} depends on Young's modulus E , Poisson ratio ν , though the contracted expression:

$$S_{ij} = \begin{bmatrix} 1/E & -\nu/E & -\nu/E \\ -\nu/E & 1/E & -\nu/E \\ -\nu/E & -\nu/E & 1/E \end{bmatrix} \quad (\text{A.11})$$

Replacing eq. (A.10) in eq. (A.8) leads to:

$$\begin{aligned} U &= U_0 - \frac{1}{2}(n_C^x P_i^x + n_C^y P_i^y + n_C^z P_i^z) \cdot \varepsilon_i \\ &= U_0 - \frac{S_{ij}}{2V} \left(\frac{n_C - n_C^z}{2} P_i^x + \frac{n_C - n_C^z}{2} P_i^y + n_C^z P_i^z \right) \\ &\quad \cdot \left(\frac{n_C - n_C^z}{2} P_j^x + \frac{n_C - n_C^z}{2} P_j^y + n_C^z P_j^z \right) \end{aligned} \quad (\text{A.12})$$

The partial derivative with respect to n_C^z gives:

$$\frac{\partial U}{\partial n_C^z} = \frac{(1+\nu)(\lambda' - \lambda)^2}{2VE} (3n_C^z - n_C) = -\lambda_0 x_C Z \quad (\text{A.13})$$

where $\lambda_0 = (1+\nu)(\lambda' - \lambda)^2 / (v^{\text{at}} E)$ and Z is the order parameter defined in eq. (2.1). From eq. (A.12), the parameter λ_0 can also be defined as:

$$\lambda_0 = 3 \frac{U|_{n_C^z=n_C} - U|_{n_C^z=n_C/3}}{(n_{\text{Fe}} + n_C)x_C^2} \quad (\text{A.14})$$

where $U|_{n_C^z=n_C}$ and $U|_{n_C^z=n_C/3}$ are the internal energy of fully ordered and fully disordered systems, respectively.

Next, the configurational entropy is calculated, which is given by:

$$S = k_B \ln \left[\prod_{i=x,y,z} \frac{n_{\text{Fe}}!}{n_C^i! (n_{\text{Fe}} - n_C^i)!} \right] \quad (\text{A.15})$$

Using Stirling's approximation, the partial derivative of S with respect to n_C^z is given by:

$$\frac{\partial S}{\partial n_C^z} = k_B \ln \left[\frac{(n_{\text{Fe}} - n_C^z)(n_C - n_C^z)}{(2n_{\text{Fe}} - n_C + n_C^z)n_C} \right] \quad (\text{A.16})$$

Eq. (A.16) and eq. (A.13) finally lead to the equilibrium master equation

(eq. (2.6)):

$$-\lambda_0 x_C Z - k_B T \ln \left[\frac{3 - 2x_C(2 + Z)}{3 - x_C(4 - Z)} \cdot \frac{1 - Z}{1 + 2Z} \right] = 0 \quad (\text{A.17})$$

The value of the Z that solves this equation is the order parameter in the equilibrium state for a given temperature T and C concentration x_C .

Appendix B

Anisotropic elasticity theory

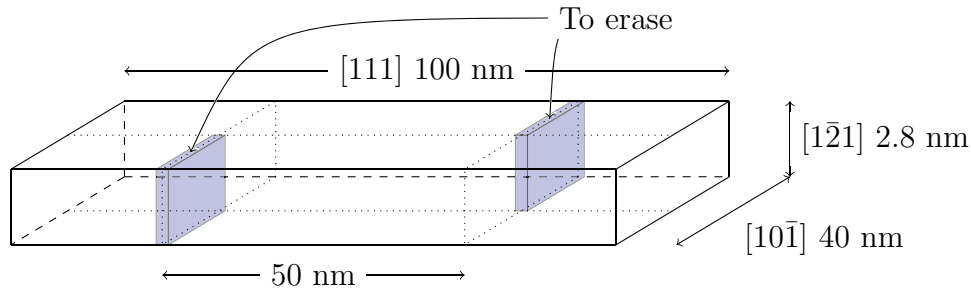


Figure B.1: Simulation box in which two edge dislocations are created with periodic boundary conditions in three directions

There are two different methods to create an edge dislocation from a perfectly crystalline simulation box. The first method is to remove atoms inside two atomic half-planes (*cf.* fig. B.1). Then the entire simulation box is relaxed in periodic boundary conditions in all directions, as explained in chap. 3. This method, however, has the drawback that the dislocations interact with each other over the periodic boundary conditions. The second method is to calculate the displacements of Fe atoms $\{u_k(x, y, z)\}$ ($k = x, y, z$) from their initial positions in the crystalline structure. The displacements are well known for isotropic materials, but due to the strong anisotropy of bcc-Fe (Zener ratio: $A = 2.36$ [Raabe *et al.*, 2002]), instead of the classical isotropic elasticity theory, the anisotropic elasticity theory proposed by Hirth and Lothe [Hirth and Lothe, 1968] should be employed. Just as in the classical isotropic elasticity theory, the displacements are calculated from the elastic coefficients c_{ijkl} ($i, j, k, l = x, y, z$) and the Burgers vector b_k . It is known, however, that the analytical equations for the displacements can be given only in special cases and therefore the general solution was not treated in their original theory. In this section, the numerical method to give general equations for displacements is explained.

Firstly, the anisotropic elasticity theory described by Hirth and Lothe [Hirth and Lothe, 1968] is presented briefly. The starting equation exploits the fact that the stress divergence is equal to zero at equilibrium ¹:

$$\frac{\partial \sigma_{ij}}{\partial x_j} = C_{ijkl} \frac{\partial \varepsilon_{kl}}{\partial x_j} = C_{ijkl} \frac{\partial^2 u_k}{\partial x_j \partial x_l} = 0, \quad \forall i = x, y, z \quad (\text{B.1})$$

where σ_{ij} is the stress tensor and ε_{ij} is the deformation tensor. In the following, the axis z coincides with the dislocation line and the axes x, y and z are enumerated as 1, 2 and 3, respectively. As it can be found in isotropic elasticity theory, it is assumed that the stress amplitude around a dislocation is inversely proportional to the distance from the dislocation line $r = \sqrt{x^2 + y^2}$, *i.e.* $\sigma \sim 1/r$. Hence, $\varepsilon \sim 1/r$ and therefore the ansatz for u_k is given in the following form:

$$u_k = -\frac{DA_k}{2\pi i} \ln(x + py) \quad (\text{B.2})$$

where D, A_k and p are unknown parameters to be determined in the following ². The prefactor $1/2\pi i$ in eq. (B.2) cancels out the result of the line integral around the origin as given in the Cauchy's integral theorem.

Inserting eq. (B.2) into eq. (B.1) we obtain:

$$(c_{i1k1} + p(c_{i1k2} + c_{i2k1}) + p^2 c_{i2k2}) A_k = 0 \quad (\text{B.3})$$

The determinant of the 3×3 -tensor $\{c_{i1k1} + p(c_{i1k2} + c_{i2k1}) + p^2 c_{i2k2}\}_{ik} = M(p)$ must be zero in order that $\{A_k\}$ has non trivial solutions³:

$$0 = \det M(p) \quad (\text{B.4})$$

$$= \begin{vmatrix} c_{11} + (c_{14} + c_{41})p + c_{44}p^2 & c_{14} + (c_{12} + c_{44})p + c_{42}p^2 & c_{15} + (c_{16} + c_{45})p + c_{46}p^2 \\ c_{41} + (c_{44} + c_{21})p + c_{24}p^2 & c_{44} + (c_{42} + c_{24})p + c_{22}p^2 & c_{45} + (c_{46} + c_{25})p + c_{26}p^2 \\ c_{51} + (c_{54} + c_{61})p + c_{64}p^2 & c_{54} + (c_{52} + c_{64})p + c_{62}p^2 & c_{55} + (c_{56} + c_{65})p + c_{66}p^2 \end{vmatrix} \quad (\text{B.5})$$

¹In the following the Einstein notation is always used

²Strictly speaking, the definition of D is redundant as it can be incorporated into A_k . However, it allows to make the determination of A_k easier later on.

³Due to the symmetry, $\sigma_{ij} = \sigma_{ji}$ and $\varepsilon_{ij} = \varepsilon_{ji}$, simplified notation $\{11, 22, 33, 23, 31, 12, 32, 13, 21\} = \{1, 2, 3, 4, 5, 6, 4, 5, 6\}$ is used here.

This gives a polynomial of degree 6 for p . It is known that there is no purely real solution to the eq. (B.5) [Eshelby *et al.*, 1953]. Since the elastic constants must be real, the six solutions for p must satisfy the relations $p(1) = p(4)^*$, $p(2) = p(5)^*$ and $p(3) = p(6)^*$. Eq. (B.2) turns into:

$$u_k = -\text{Re} \left[\sum_n^3 \frac{D(n)A_k(n)}{2\pi i} \ln(x + p(n)y) \right] \quad (\text{B.6})$$

Whether it is a screw or an edge dislocation, the line integral of the deformation around a dislocation gives the Burgers vector. The displacements being the integral of the deformation, we obtain the Burgers vector by inserting the boundary conditions:

$$\oint \varepsilon_{kj} dx_j = \lim_{y \rightarrow -0} u_k(x, y) - \lim_{y \rightarrow +0} u_k(x, y) = \text{Re} \left[\sum_n^3 \pm D(n)A_k(n) \right] = b_k \quad (\text{B.7})$$

The sign \pm is negative, if the imaginary part of $p(n)$ is positive, otherwise is positive. We can choose $p(1)$, $p(2)$ and $p(3)$ in the way that the sign is always positive by exploiting the fact that if $p(n)$ is a solution, $p(n)^*$ is also a solution.

At equilibrium the total force on the dislocation must be equal to zero. This means that the total stress that is exerted on any arbitrary surface around the dislocation must be equal to zero.

$$0 = \oint S \cdot ((\vec{e}_1 dx + \vec{e}_2 dy) \times \vec{e}_3) \quad (\text{B.8})$$

$$= \text{Re} \left[\sum_n^3 (c_{i2k1} + p(n)c_{i2k2}) D(n)A_k(n) \right] \quad (\text{B.9})$$

where S is the stress tensor, which is calculated using eq. (B.6) and the relation:

$$\sigma_{ij} = c_{ijkl} \varepsilon_{kl} = \frac{c_{ijkl}}{2} \left(\frac{\partial u_k}{\partial x_l} + \frac{\partial u_l}{\partial x_k} \right) \quad (\text{B.10})$$

So far, we have obtained 7 equations in eqs. (B.5), (B.7) and (B.9). And there are parameters $D(n)$, $A_k(n)$ and $p(n)$ to determine. In the original book of Hirth and Lothe [Hirth and Lothe, 1968], special cases in which eq. (B.5) can be solved analytically were treated. Indeed, according to the Abel-Ruffini theorem [Abel *et*

al., 1881], there is no analytic solution to the eq. (B.5). In this section, therefore, the numerical method to obtain $p(n)$ is explained, then the explicit equations for the further unknown parameters $D(n)$ and $A_k(n)$ are presented, which eventually leads to the explicit form of u_k .

As we defined the enumeration of $p(n)$ in such a way that the sign is always in positive in eq. (B.7), the imaginary part of $p(1)$, $p(2)$ and $p(3)$ are negative, it suffices to search for the solutions of eq. (B.5) in the region $\text{Im}[p] < 0$. The solutions to eq. (B.5) are looked for iteratively using the Newton-Raphson method⁴:

$$p_{m+1}(n) = p_m(n) - \frac{\det M(p_m(n))}{\det M(p_m(n)) - \det M(p_{m-1}(n))} (p_m(n) - p_{m-1}(n)) \quad (\text{B.11})$$

The initial point $p_{m=0}$ is chosen randomly. This process is iterated until the condition $\det M(p_{n,m}) < 10^{-3} \text{ GPa}^3$ is fulfilled.

Next, $A_k(n)$ are calculated that satisfy the eq. (B.3) for each $p(n)$. Obviously, the values of $A_k(n)$ can be determined up to a multiplication by a constant. Thus, one of the non-zero components of $A_k(n)$ can be chosen as 1. In order to know which components of $A_k(n)$ are non-zero, we define the minor of the matrix M by:

$$[M]_{ij} := M_{(i+1) \bmod 3 (j+1) \bmod 3} M_{(i+2) \bmod 3 (j+2) \bmod 3} - M_{(i+1) \bmod 3 (j+2) \bmod 3} M_{(i+2) \bmod 3 (j+1) \bmod 3} \quad (\text{B.12})$$

In the following, we use the notation $i+1$, $j+1$ etc. instead of $(i+1) \bmod 3$, $(j+1) \bmod 3$. The component $A_k(n)$ is non-zero, if $[M]_{kj}$ is non-zero. In order to have the numerically most stable value, the maximum value of $[M]_{kj}$ is searched for, and for the corresponding component $A_k(n)$ the value 1 is allocated. The other two components are calculated by:

$$\begin{pmatrix} A_{k+1}(n) \\ A_{k+2}(n) \end{pmatrix} = -\frac{1}{[M]_{ik}(n)} \begin{pmatrix} M_{i+1k+2}(n) & -M_{ik+2}(n) \\ -M_{i+1k+1}(n) & M_{ik+1}(n) \end{pmatrix} \begin{pmatrix} M_{ik}(n) \\ M_{i+1k}(n) \end{pmatrix} \quad (\text{B.13})$$

Finally, the values for $D(n)$ are to determine. The eqs. (B.7) and (B.9) can

⁴In order for the iterative calculation to converge within a reasonable amount of time, the real and imaginary parts are treated separately.

be written as:

$$\begin{aligned} \operatorname{Re} \left[\sum_n^3 D(n) A_k(n) \right] &= \sum_n^3 (\operatorname{Re}[D(n)] \operatorname{Re}[A_k(n)] - \operatorname{Im}[D(n)] \operatorname{Im}[A_k(n)]) \\ &= b_k \end{aligned} \quad (\text{B.14})$$

and

$$\begin{aligned} \operatorname{Re} \left[\sum_n^3 \underbrace{(c_{i2k1} + p(n)c_{i2k2}) A_k(n)}_{q_i(n)} D(n) \right] &= \sum_n^3 (\operatorname{Re}[q_i(n)] \operatorname{Re}[D(n)] - \operatorname{Im}[q_i(n)] \operatorname{Im}[D(n)]) \\ &= 0 \end{aligned} \quad (\text{B.15})$$

Eqs. (B.14) and (B.15) can be combined to:

$$\sum_n^3 \begin{pmatrix} \operatorname{Re}[A_i(n)] & -\operatorname{Im}[A_i(n)] \\ \operatorname{Re}[q_i(n)] & -\operatorname{Im}[q_i(n)] \end{pmatrix} \begin{pmatrix} \operatorname{Re}[D(n)] \\ \operatorname{Im}[D(n)] \end{pmatrix} = \begin{pmatrix} b_i \\ 0 \end{pmatrix} \quad (\text{B.16})$$

Eq. (B.16) is valid for each direction of i . Therefore, it can be expanded into a matrix of 6×6 by taking the three values of n in the row and the three directions of i in the column. The explicit solution for $D(n)$ is found by calculating the equation⁵:

$$\begin{pmatrix} \operatorname{Re}[D_1] \\ \operatorname{Im}[D_1] \\ \operatorname{Re}[D_2] \\ \operatorname{Im}[D_2] \\ \operatorname{Re}[D_3] \\ \operatorname{Im}[D_3] \end{pmatrix} = \begin{pmatrix} \operatorname{Re}[A_{11}] & -\operatorname{Im}[A_{11}] & \operatorname{Re}[A_{12}] & -\operatorname{Im}[A_{12}] & \operatorname{Re}[A_{13}] & -\operatorname{Im}[A_{13}] \\ \operatorname{Re}[q_{11}] & -\operatorname{Im}[q_{11}] & \operatorname{Re}[q_{12}] & -\operatorname{Im}[q_{12}] & \operatorname{Re}[q_{13}] & -\operatorname{Im}[q_{13}] \\ \operatorname{Re}[A_{21}] & -\operatorname{Im}[A_{21}] & \operatorname{Re}[A_{22}] & -\operatorname{Im}[A_{22}] & \operatorname{Re}[A_{23}] & -\operatorname{Im}[A_{23}] \\ \operatorname{Re}[q_{21}] & -\operatorname{Im}[q_{21}] & \operatorname{Re}[q_{22}] & -\operatorname{Im}[q_{22}] & \operatorname{Re}[q_{23}] & -\operatorname{Im}[q_{23}] \\ \operatorname{Re}[A_{31}] & -\operatorname{Im}[A_{31}] & \operatorname{Re}[A_{32}] & -\operatorname{Im}[A_{32}] & \operatorname{Re}[A_{33}] & -\operatorname{Im}[A_{33}] \\ \operatorname{Re}[q_{31}] & -\operatorname{Im}[q_{31}] & \operatorname{Re}[q_{32}] & -\operatorname{Im}[q_{32}] & \operatorname{Re}[q_{33}] & -\operatorname{Im}[q_{33}] \end{pmatrix}^{-1} \begin{pmatrix} b_1 \\ 0 \\ b_2 \\ 0 \\ b_3 \\ 0 \end{pmatrix} \quad (\text{B.17})$$

The inverse matrix is calculated using the Gaussian elimination. Now the relations for all the unknown parameters p_n (from eq. (B.11)), $A_k(n)$ (from eq. (B.13)) and $D(n)$ (from eq. (B.17)) are established. This means that the displacements u_k can be calculated. Eq. (B.6) turns into

⁵ $A_i(n)$ and $q_i(n)$ are replaced by A_{in} and q_{in}

$$u_k = \text{Im} \left[\sum_n^3 \frac{D(n)A_k(n)}{2\pi} \ln(x + p(n)y) \right] \quad (\text{B.18})$$

$$\begin{aligned} &= - \sum_n^3 \frac{(\text{Re}[A_k(n)]\text{Im}[D(n)] + \text{Re}[A_k(n)]\text{Im}[D(n)])}{2\pi} \frac{\ln((x + \text{Re}[p(n)]y)^2 + (\text{Im}[p(n)]y)^2)}{2} \\ &\quad + \sum_n^3 \frac{(\text{Re}[A_k(n)]\text{Re}[D(n)] - \text{Im}[A_k(n)]\text{Im}[D(n)])}{2\pi} \text{atan} \left(\frac{\text{Im}[p(n)]y}{x + \text{Re}[p(n)]y} \right) \end{aligned} \quad (\text{B.19})$$

One important aspect of this result is to predict how large a simulation box has to be, in order to eliminate box size effect (*cf.* fig. B.2). To allow for this, the stress is calculated using this result by:

$$\sigma_{ij} = \frac{c_{ijkl}}{2} \left(\frac{\partial u_k}{\partial x_l} + \frac{\partial u_l}{\partial x_k} \right) \quad (\text{B.20})$$

$$= - \text{Im} \left[\sum_n \frac{D(n)A_k(n)}{2\pi} \frac{c_{ijk1} + p(n)c_{ijk2}}{x + p(n)y} \right] \quad (\text{B.21})$$

$$= - \text{Im} \left[\sum_n \frac{D(n)A_k(n)}{2\pi} \frac{(c_{ijk1} + p(n)c_{ijk2})(x + p(n)^*y)}{|x + p(n)y|^2} \right] \quad (\text{B.22})$$

$$\begin{aligned} &= - \sum_n \frac{\text{Re}[D(n)]\text{Im}[A_k(n)](c_{ijk1}x + (c_{ijk2}x + c_{ijk1}y)\text{Re}[p(n)] + c_{ijk2}|p(n)|^2y)}{2\pi|x + p(n)y|^2} \\ &\quad - \sum_n \frac{\text{Im}[D(n)]\text{Re}[A_k(n)](c_{ijk1}x + (c_{ijk2}x + c_{ijk1}y)\text{Re}[p(n)] + c_{ijk2}|p(n)|^2y)}{2\pi|x + p(n)y|^2} \\ &\quad - \sum_n \frac{(\text{Re}[D(n)]\text{Re}[A_k(n)] - \text{Im}[D(n)]\text{Im}[A_k(n)])(c_{ijk2}x - c_{ijk1}y)\text{Im}[p(n)]}{2\pi|x + p(n)y|^2} \end{aligned} \quad (\text{B.23})$$

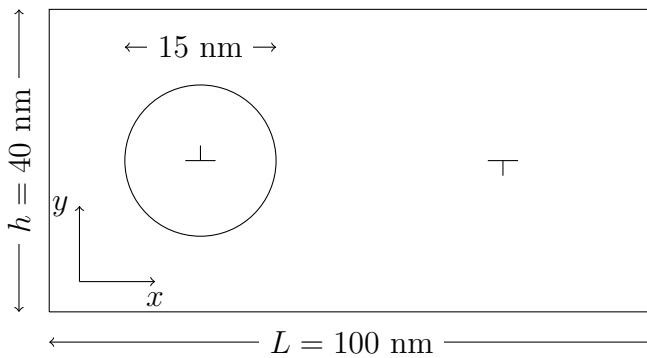


Figure B.2: Simulation box containing two edge dislocations with periodic boundary conditions in all three directions

The non-zero elastic coefficients that are calculated via molecular statics in the orientation for the edge dislocation $x = [111], y = [\bar{1}01], z = [1\bar{2}1]$ are given below

(all units in GPa):

$$\begin{pmatrix} c_{11} & c_{12} & c_{13} & c_{14} & c_{15} & c_{16} \\ c_{21} & c_{22} & c_{23} & c_{24} & c_{25} & c_{26} \\ c_{31} & c_{32} & c_{33} & c_{34} & c_{35} & c_{36} \\ c_{41} & c_{42} & c_{43} & c_{44} & c_{45} & c_{46} \\ c_{51} & c_{52} & c_{53} & c_{54} & c_{55} & c_{56} \\ c_{61} & c_{62} & c_{63} & c_{64} & c_{65} & c_{66} \end{pmatrix} = \begin{pmatrix} 332.6 & 100.4 & 100.4 & 0 & 0 & 0 \\ 100.4 & 310.3 & 122.7 & 0 & -31.59 & 0 \\ 100.4 & 122.7 & 310.3 & 0 & 31.59 & 0 \\ 0 & 0 & 0 & 93.80 & 0 & -31.59 \\ 0 & -31.59 & 31.59 & 0 & 71.46 & 0 \\ 0 & 0 & 0 & -31.59 & 0 & 71.46 \end{pmatrix} \quad (\text{B.24})$$

Fig. B.3 shows the stress field of non-zero components around an edge dislocation calculated by MS and anisotropic elasticity theory. The simulation box dimensions are given in fig. B.2, with periodic boundary conditions in all three directions. Obviously, the deviation of stress is more conspicuous in the region far away from the dislocation line. This is caused by the periodic boundary conditions, as the stress must be cancelled out on the simulation boundaries in the x and y directions. In the LinCoSS method [Tchitchekova *et al.*, 2014], the error in activation energy is under 0.5 % (which translates to an error of 20 % in diffusion coefficient at ambient temperature), if the error in stress is under 0.1 GPa. Following the anisotropic elasticity theory, the box height h must be over 225 nm and the width L must be over 425 nm. This size, however, cannot be treated by the MD with current numerical resources.

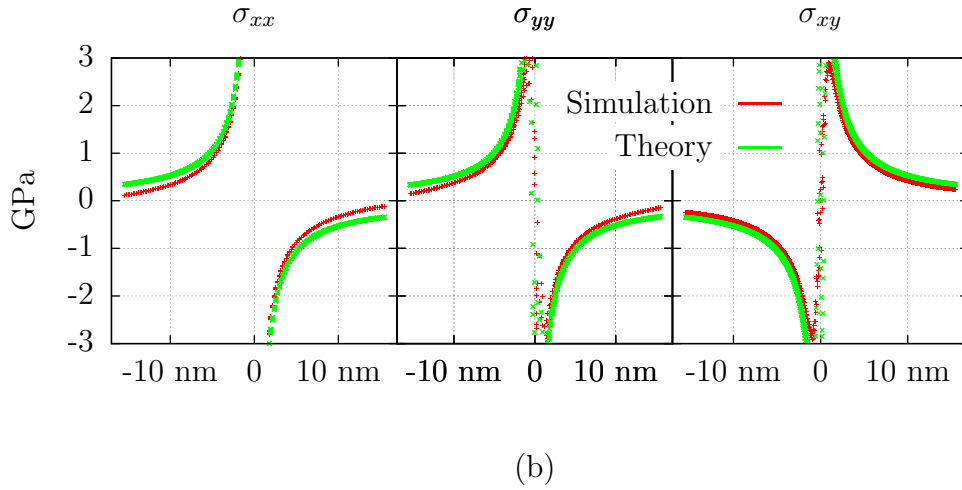
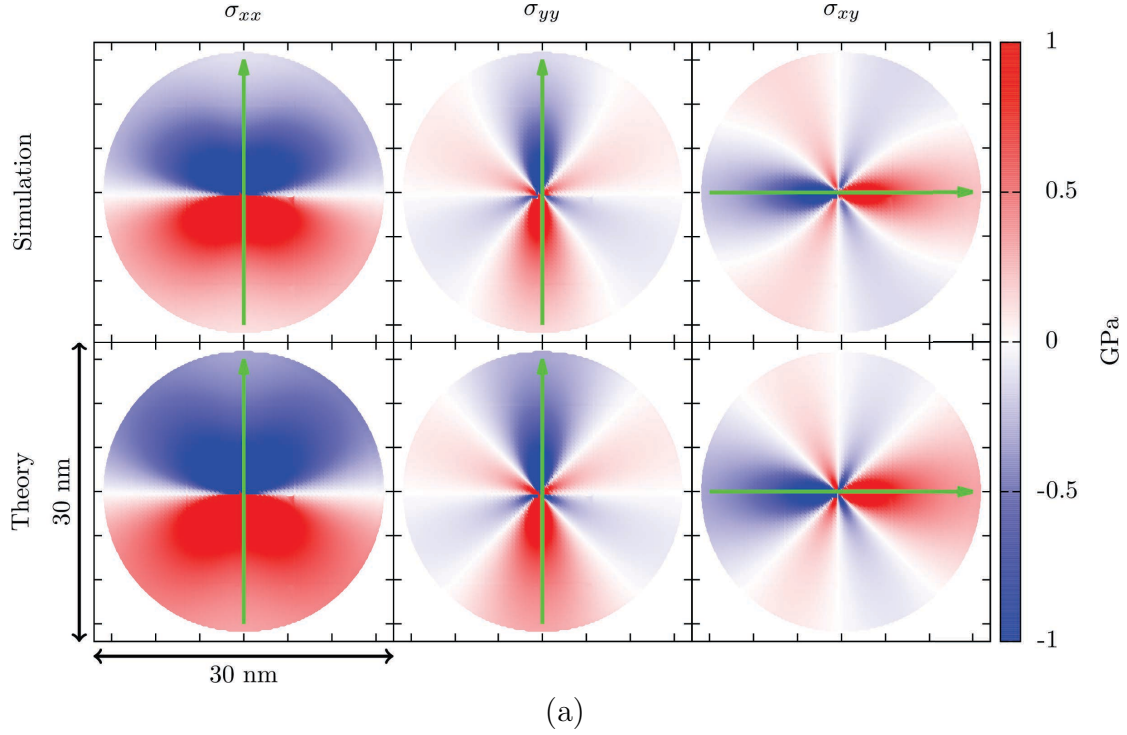


Figure B.3: (a): Stress field calculated by MS simulation and anisotropic elasticity theory. (b): Stress value under the green lines as a function of the distance from the dislocation line.

Appendix C

How to calculate attempt frequency κ

For a given interstitial jump with associated activation energy E , the probability $p dt$ that this interstitial jump is effectuated within a time span of dt follows the Arrhenius law:

$$p dt = \kappa \exp\left(-\frac{E}{k_B T}\right) dt \quad (\text{C.1})$$

where κ is the attempt frequency. Considering that C atoms perform most of

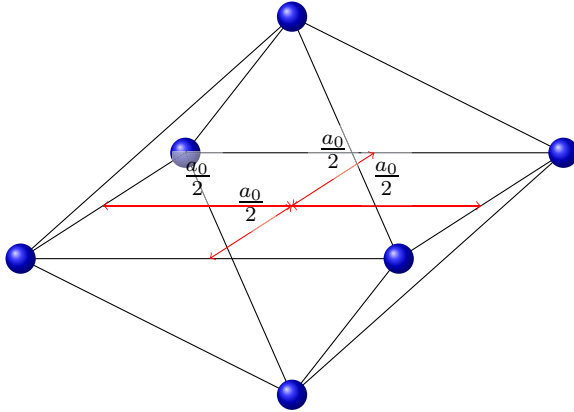


Figure C.1: Distance between an octahedral interstitial site in the middle and neighbouring sites.

the time a random walk in bcc Fe, the attempt frequency described in chap. 1 sec. 1.4 can be estimated by comparing with experimental results by looking at the diffusion coefficient. Suppose \vec{x}_n is the displacement of a C atom from the initial position after n interstitial jumps and t_n is its dwelling time. According to the diffusion equation, the relation between \vec{x}_n and t_n is given by:

$$\langle \vec{x}_n^2 \rangle = 6D \langle t_n \rangle \quad (\text{C.2})$$

where the brackets stand for average value. The distance of one interstitial jump is half a lattice parameter, $a_0/2$ (*cf.* fig. C.1), with $a_0 = 0.286$ nm. By inserting this into eq. (C.2) we obtain:

$$\langle t_n \rangle = \frac{a_0^2}{8D} \quad (\text{C.3})$$

According to the Arrhenius law, the diffusion coefficient D is given by $D = D_0 \exp(-E/k_B T)$ where E is the activation energy for a C atom to migrate from an interstitial site to an adjacent interstitial site. Eq. (C.3) then becomes:

$$\langle t_n \rangle = \underbrace{\frac{a_0^2}{8D_0}}_{=1/\kappa} \exp\left(\frac{E}{k_B T}\right) \quad (\text{C.4})$$

With the experimental results of D_0 we can quantify κ (*cf.* eq. (1.17)):

	D_0 [m ² /s]	κ [1/s]
McLellan and Wasz [1993]	4.876×10^{-7}	4.78×10^{13}
Da Silva and McLellan [1976]	1.670×10^{-7}	1.64×10^{13}
Wert and Zener [1949]	8×10^{-7}	7.87×10^{13}

Appendix D

Correction of LinCoSS

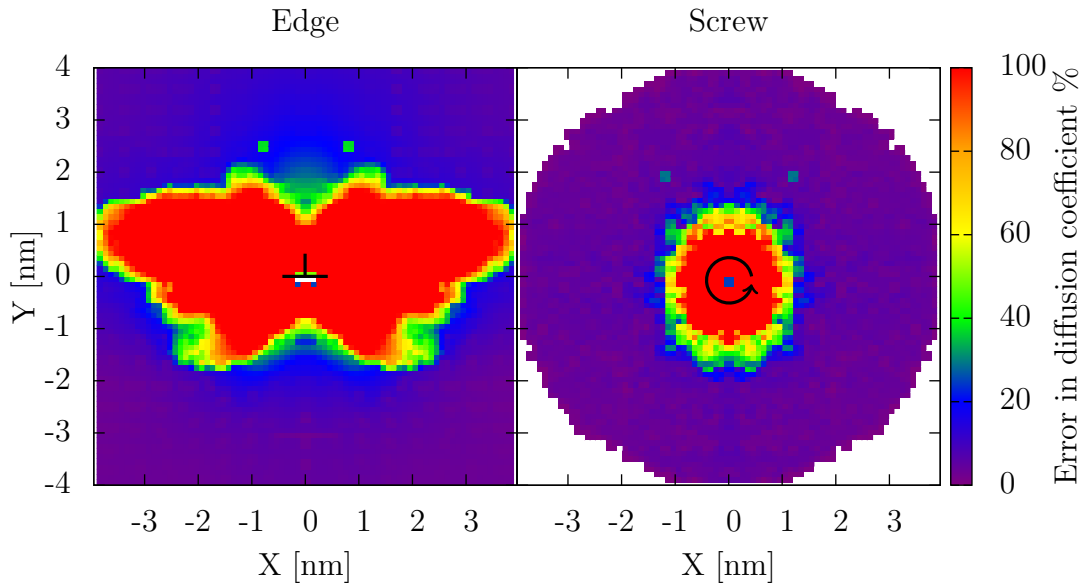


Figure D.1: Error in diffusion coefficient around an edge and a screw dislocation for 300 K. The measurement is performed only in the region $X > 0$ due to the symmetry of the stress field. To better visualize the results the results are mirrored on the other side. Within each square of $0.04 \text{ nm} \times 0.04 \text{ nm}$, the maximum error value is shown.

In chap. 4, sec. 4.2, the error of LinCoSS with respect to CI-NEB was calculated as around an edge and a screw dislocation (*cf.* fig. D.1). As so far no sufficiently fast computational technique has been found to calculate activation energies that can be incorporated into AKMC for the investigation of Cottrell atmosphere formation, it is crucial to possibly lower the error of LinCoSS. There are three possible explanations that are suggested for the origin of the error.

1. The stress gradient was not taken into account in the conception of LinCoSS, whereas it may affect the activation energy around dislocations.

2. It was assumed that the activation energy given by CI-NEB is a continuous function. The reliability of the values obtained, however, has not been examined for strong matrix deformation.
3. LinCoSS is based on the approximation of the Taylor expansion of degree 2, *i.e.* of the form

$$E(\vec{\sigma}) = E(0) + \sum_i \frac{\partial E}{\partial \sigma_i}(0) \sigma_i + \sum_i \frac{\partial^2 E}{\partial \sigma_i^2}(0) \sigma_i^2$$

with $i = xx, yy, zz, xy, xz, yz$. However, cross terms such as $\sum_{i,j} \frac{\partial^2 E}{\partial \sigma_i \partial \sigma_j}(0) \sigma_i \sigma_j$ ($i \neq j$) are not taken into account.

In the following sections, these three possible sources of error are treated independently, to find the source of the error.

D.1 First possibility: Stress gradient

In the previous section, the error of LinCoSS was calculated by comparing the activation energy via CI-NEB in a simulation box containing a dislocation E_D^{NEB} and the activation energy via LinCoSS E_D^{Lin} by taking the local stress value of the C atom (*cf.* fig. 4.4). Since the dislocation creates a stress gradient, E_D^{NEB} may differ from the activation energy calculated via CI-NEB in a bulk E_B^{NEB} for the same stress value. If $E_D^{\text{NEB}} - E_B^{\text{NEB}} (= \Delta E^{\text{NEB}})$ corresponds to $E_D^{\text{NEB}} - E_D^{\text{Lin}} (= \Delta E^{\text{Lin}})$, it implies that the error of LinCoSS comes from the stress gradient that was not taken into account when LinCoSS was designed. This section aims at comparing the activation energies via CI-NEB in a simulation box containing a dislocation and in a bulk by reproducing the stress field of the simulation box containing a dislocation for each interstitial jump in a bulk simulation box and perform a CI-NEB calculation. While reproducing the stress field around a dislocation, the coordinate transformation (*cf.* sec. 1.4.2) is also performed accordingly. The reproduction of the stress field is done by modifying the box dimension via conjugate gradient (CG) method. The activation energy differences are calculated according to the following procedure:

1. Detection of the interstitial jumps in the simulation box containing a dislocation, for which the activation energy error of LinCoSS is larger than 5 % ($= 100 \times |E_D^{\text{NEB}} - E_D^{\text{Lin}}| / E_D^{\text{NEB}}$)
2. Calculation of the local stress field around the interstitial jumps

3. Reproduction of the stress in a bulk (10x10x10 lattices) after the coordinate transformation
4. Calculation of the activation energy E_B^{NEB} via CI-NEB.
5. Calculation of the difference between $E_D^{\text{NEB}} - E_B^{\text{NEB}} (= \Delta E^{\text{NEB}})$ and $E_D^{\text{NEB}} - E_D^{\text{Lin}} (= \Delta E^{\text{Lin}})$.

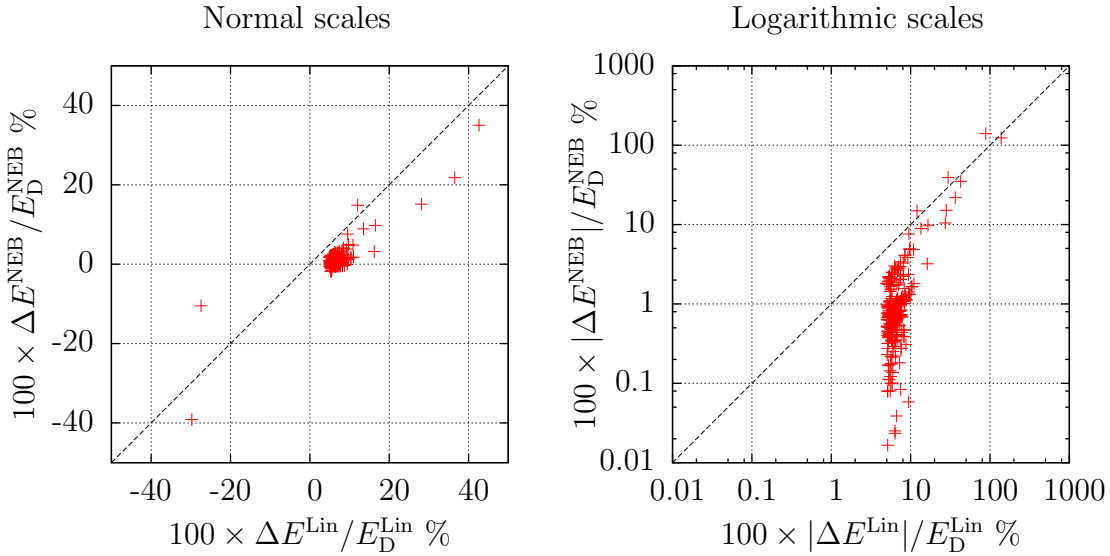


Figure D.2: Comparison of the error of LinCoSS and CI-NEB. The left figure shows the errors. The right figure shows the errors in absolute values in logarithmic scale in both directions. The black line shows the same value for LinCoSS and CI-NEB. If a point is under the black line, ΔE^{Lin} is larger, *i.e.* the error of LinCoSS is not reproduced by the CI-NEB calculation in the bulk.

The results are given in normal scales and in logarithmic scales with absolute values (*cf.* fig. D.2). It can be seen that LinCoSS generally overestimates the activation energies. Apparently, ΔE^{NEB} is not exactly zero. However, in most of the cases, ΔE^{NEB} is significantly lower than $\Delta E^{\text{LinCoSS}}$. Hence, it implies that the error of LinCoSS is not caused by the stress gradient, that is present around the dislocation.

D.2 Second possibility: Reliability of measurement with CI-NEB

When LinCoSS was designed, it was assumed that the CI-NEB gives a smooth activation energy landscape as a function of the stress. In order to verify this, the activation energy landscape is obtained by varying two components of stress. The

calculation was performed in a small simulation box of $10 \times 10 \times 10$ Fe-lattices with one C atom inside.

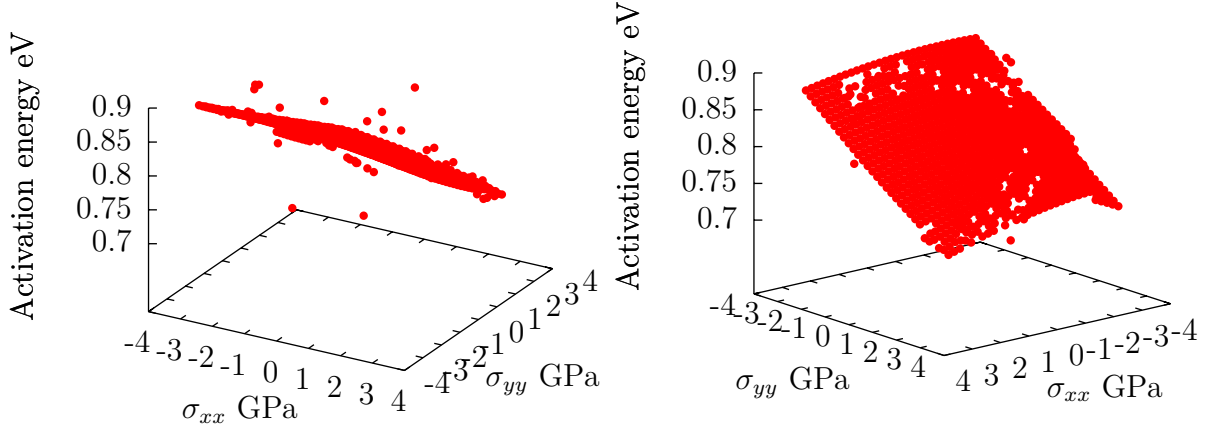


Figure D.3: Activation energy calculated through CI-NEB in dependence on σ_{xx} and σ_{yy} from two different angles. 40 points in each stress component was measured, making the total number of points of 1600.

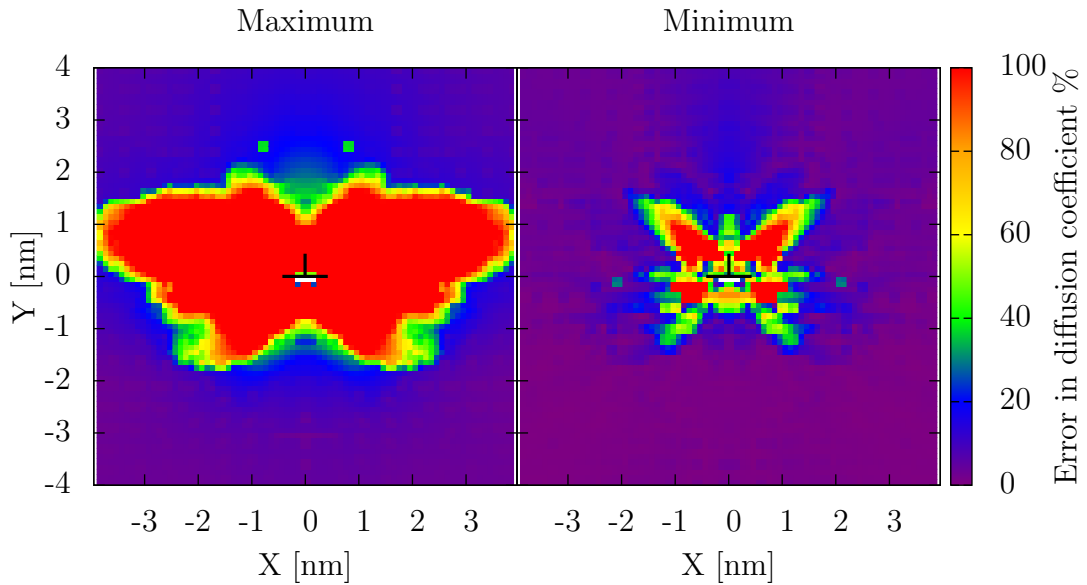


Figure D.4: Comparison of error in diffusion coefficient by taking the maximum (left) and the minimum (right) of all points being in each square cylinder of $0.1 \text{ nm} \times 0.1 \text{ nm}$

As an example, the activation energies as a function of σ_{xx} and σ_{yy} are shown in fig. D.3. Clearly there is a certain number of irregular values. This could be observed for other combinations of two stress components as well. This means that the activation energy is obviously not correctly calculated with CI-NEB for

certain values of stress. Indeed, instead of taking the maximum value of all errors within each $0.1 \text{ nm} \times 0.1 \text{ nm}$ square cylinder, by taking the minimum value, the region in which LinCoSS is not valid shrinks significantly (*cf.* fig. D.4).

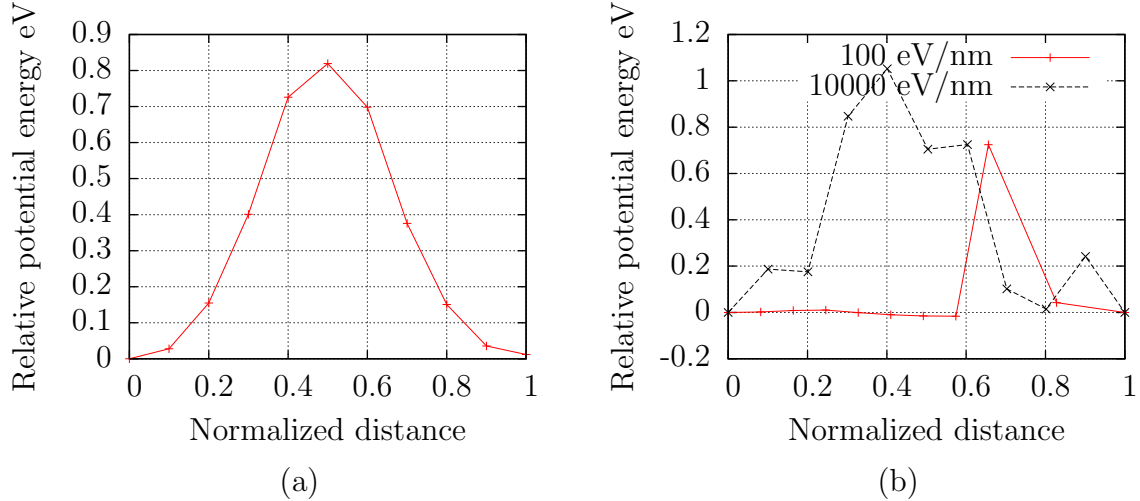


Figure D.5: Potential energy evolution of CI-NEB relative to the first replica. (a): Stress free state. (b): $\sigma_{xx} = -3 \text{ GPa}$, $\sigma_{xy} = 3 \text{ GPa}$. The label shows the spring force of the CI-NEB (*cf.* chap. 1.4.1 sec. 1)

A further investigation into the potential energy of each replica at the end of CI-NEB for a point with irregularity (*cf.* fig. D.5) shows that the energy evolution does not give a regular form.

However, although this irregularity may have had a contribution to the increase of the error in diffusion coefficient, the irregular points are only sparsely distributed, which makes it very unlikely that the entire region of large error was covered due to this irregularity.

D.3 Third possibility: Dependence on cross terms

In the original article, LinCoSS was developed by calculating the activation energy by CI-NEB while solely one stress component was varied. Then the results were fitted through a function of type $E(\sigma_i) = a_i \sigma_i^2 + b_i \sigma_i + E_0$ ($i = xx, yy, zz, xy, xz, yz$) via least square method. In order to apply the same method to the coefficients of cross terms $\frac{\partial^2 E}{\partial \sigma_i \partial \sigma_j}(0) \sigma_i \sigma_j$, the activation energy was measured with CI-NEB while varying two stress components independently.

However, it turned out that the activation energy calculated through CI-NEB does not behave regularly as a function of two stress components, as it can be seen in fig. D.6 for the case of $\{\sigma_{xx}, \sigma_{xy}\}$. In particular, in the presence of both uniaxial and shear stress, the activation energy landscape undergoes a clear kink.

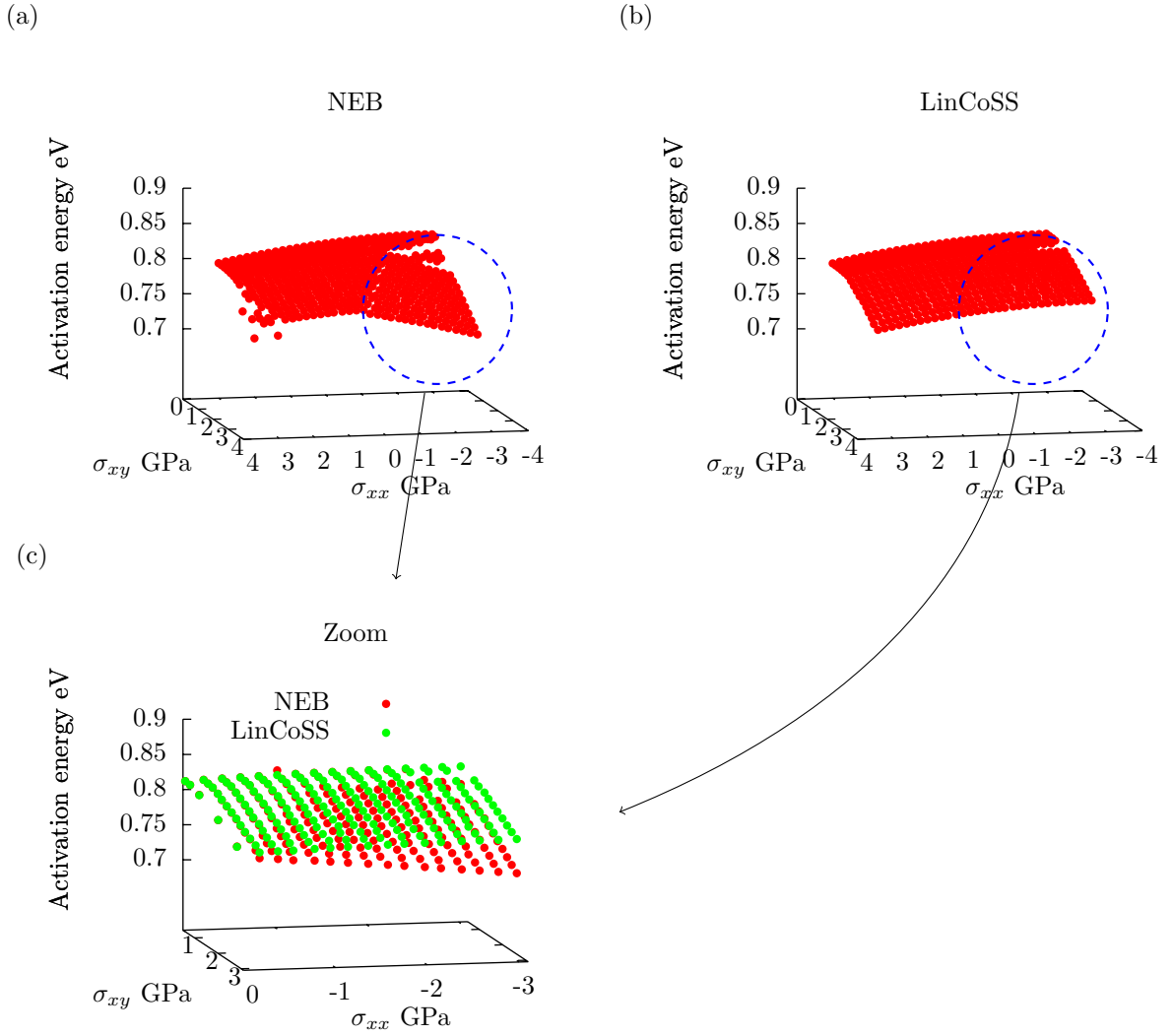


Figure D.6: (a): Activation energy measured through CI-NEB in dependence on σ_{xx} and σ_{xy} . (b): Activation energy calculated through LinCoSS. (c): Superposition of two CI-NEB and LinCoSS in the kink region.

The same behavior is also observed for $\{\sigma_{xx}, \sigma_{xz}\}$ and $\{\sigma_{xy}, \sigma_{xz}\}$ (*cf.* fig. D.7). This behavior was not taken into account by LinCoSS when it was conceived, as it appears only when two stress components are present. Yet, Taylor approximation of the energy landscape cannot account for such a behavior, either.

On the other hand, this kink zones can be relatively well identified and the activation energy variation within these zones is more or less proportional to the stress variation. Therefore, the parametrization for each combination of stress

components is undertaken in the form¹:

$$E'(\sigma_i, \sigma_j) = a'_i \sigma_i + b'_j \sigma_j + E'_0 \quad (\text{D.1})$$

where $i, j = xx, yy, zz, xy, xz, yz, i \neq j$ and a'_i and b'_j are parameters to be obtained by fitting the activation energies obtained through CI-NEB. Hence, whenever the stress components $\{\sigma_i, \sigma_j\}$ is in the kink zone, eq. (D.1) replaces eq. (4.1), which results in:

$$E'(\sigma_{xx}, \sigma_{yy}, \sigma_{zz}, \sigma_{xy}, \sigma_{yz}, \sigma_{xz}) = E(\sigma_{xx}, \sigma_{yy}, \sigma_{zz}, \sigma_{xy}, \sigma_{yz}, \sigma_{xz}) - E(\sigma_i) - E(\sigma_j) + \underbrace{E'(\sigma_i, \sigma_j)}_{\text{Correction}} \quad (\text{D.2})$$

Specifically, it is done in the zones which satisfy:

$$-\sigma_{xx} + |\sigma_{xy}| > 2.8 \text{ GPa} \quad (\text{D.3})$$

$$-\sigma_{xx} + |\sigma_{xz}| > 2.8 \text{ GPa} \quad (\text{D.4})$$

$$|\sigma_{xy}| + |\sigma_{xz}| > 2.0 \text{ GPa} \quad (\text{D.5})$$

where for the condition (D.5), the correction is performed only in the compression zone since it is clearly not necessary in the traction zone. The corrections are calculated by fitting the results and we obtained following equations:

$$E(\sigma_{xx}, \sigma_{xy}) = E_{x,y} + a_{x,y} \sigma_{xx} + b_{x,y} \sigma_{xy} + c_{x,y} \sigma_{xx}^2 + d_{x,y} \sigma_{xy}^2 \quad (\text{D.6})$$

$$E(\sigma_{xx}, \sigma_{xz}) = E_{x,y} + a_{x,z} \sigma_{xx} + b_{x,z} \sigma_{xz} + c_{x,z} \sigma_{xx}^2 + d_{x,z} \sigma_{xz}^2 \quad (\text{D.7})$$

$$E(\sigma_{xy}, \sigma_{xz}) = E_{x,y} + a_{y,z} \sigma_{xy} + b_{y,z} \sigma_{xz} + c_{y,z} \sigma_{xy}^2 + d_{y,z} \sigma_{xz}^2 \quad (\text{D.8})$$

$E_{x,y} = 0.8583$	eV	$E_{x,z} = 0.8585$	eV	$E_{y,z} = 0.8585$	eV
$a_{x,z} = 0.009311$	$\frac{\text{eV}}{\text{GPa}}$	$a_{x,y} = 0.009685$	$\frac{\text{eV}}{\text{GPa}}$	$a_{y,z} = -0.03019$	$\frac{\text{eV}}{\text{GPa}}$
$b_{x,y} = -0.03210$	$\frac{\text{eV}}{\text{GPa}}$	$b_{x,z} = -0.03275$	$\frac{\text{eV}}{\text{GPa}}$	$c_{x,y} = -0.0006221$	$\frac{\text{eV}}{\text{GPa}}$
$c_{x,z} = -0.0007454$	$\frac{\text{eV}}{\text{GPa}^2}$	$c_{y,z} = -0.0006151$	$\frac{\text{eV}}{\text{GPa}^2}$	$d_{x,z} = 0.001664$	$\frac{\text{eV}}{\text{GPa}^2}$
$d_{x,y} = -0.0003360$	$\frac{\text{eV}}{\text{GPa}^2}$	$b_{y,z} = -0.03354$	$\frac{\text{eV}}{\text{GPa}^2}$	$d_{y,z} = 0.002074$	$\frac{\text{eV}}{\text{GPa}^2}$

Near the dislocation line, the conditions (D.3), (D.4) and (D.5) are satisfied at the same time. When two of them are satisfied, the mean value of the corrections is taken, which means *e.g.* $E_{\text{correction}} = (E(\sigma_{xx}, \sigma_{xy}) + E(\sigma_{xx}, \sigma_{xz}))/2$.

¹Hereafter, the notation $E(\sigma_i)$ is used to indicate the activation energy as a function of the component σ_i , $i = xx, yy, zz, xy, xz, yz$ and all the other components are equal to zero. Analogical notation for $E(\sigma_i, \sigma_j)$

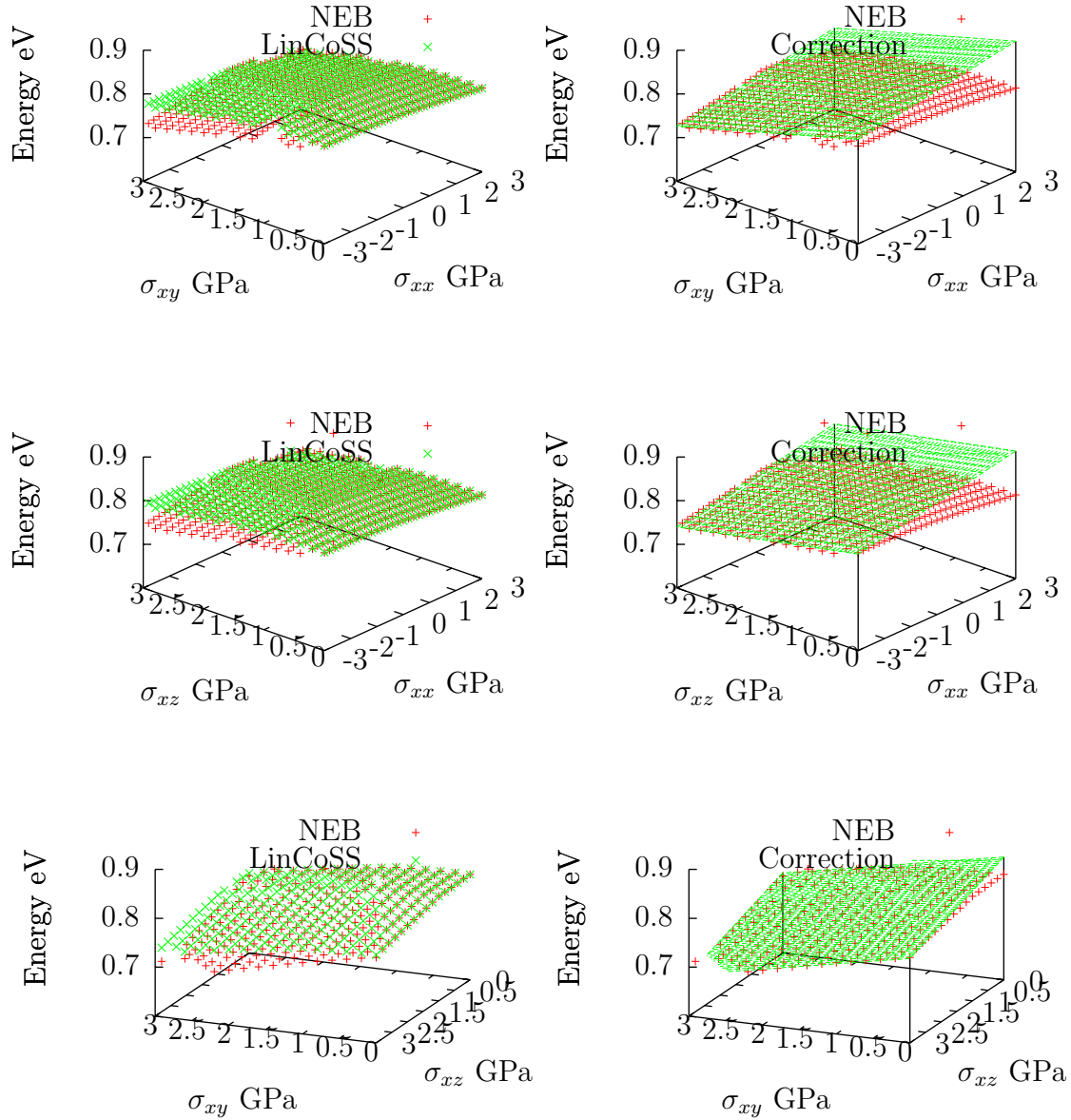


Figure D.7: Activation energy as a function of two stress components with CI-NEB and LinCoSS. Left: CI-NEB and original LinCoSS. Right: CI-NEB and corrected LinCoSS for the zone with kink.

It can be observed that this new correction indeed makes the error of LinCoSS with respect to CI-NEB smaller depending on the location (*cf.* fig. D.10). Yet the effect can be seen only in a small zone close to the dislocation line, which is surrounded by high error region. The reason why the correction to LinCoSS worked near the dislocation line and failed in the surrounding area can be better understood with fig. D.11. Indeed, the zone in which the error is significantly lowered is also the zone in which the correction is performed. On the other hand,

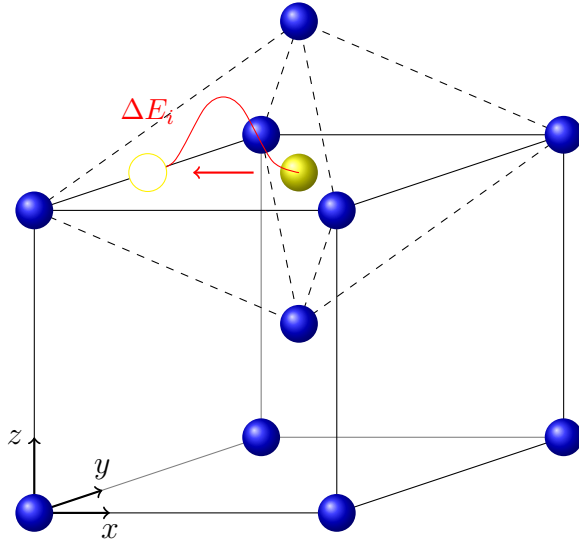


Figure D.8: Activation energy calculation using CI-NEB.

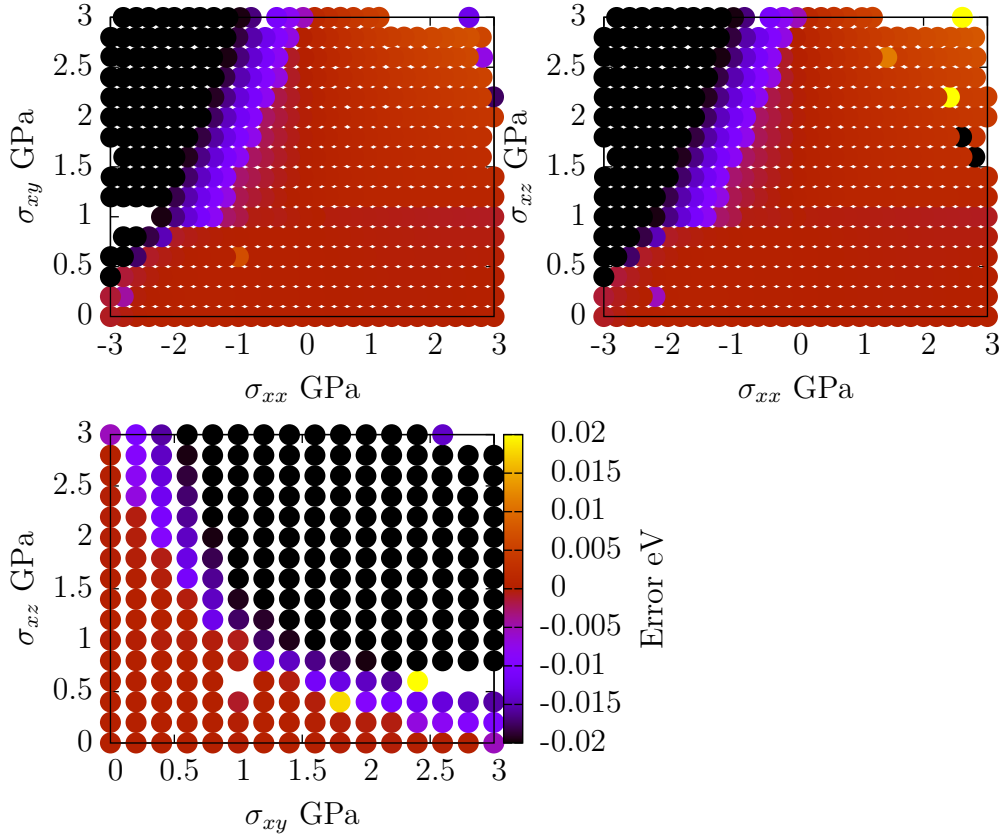


Figure D.9: Difference in activation energy calculated by CI-NEB and LinCoSS in eV for pairs of stress components for which a kink was observed.

the region in which the error is not corrected is outside of the region where LinCoSS is corrected. This implies that there is possibly a similar kink of higher order, such as $\sigma_{xx}\sigma_{xy}\sigma_{xz}$, as the kinks are observed for the stress combinations of $\{\sigma_{xx}\sigma_{xy}\}$, $\{\sigma_{xx}\sigma_{xz}\}$ and $\{\sigma_{xy}\sigma_{xz}\}$. This possibility, however, is not investigated in this work,

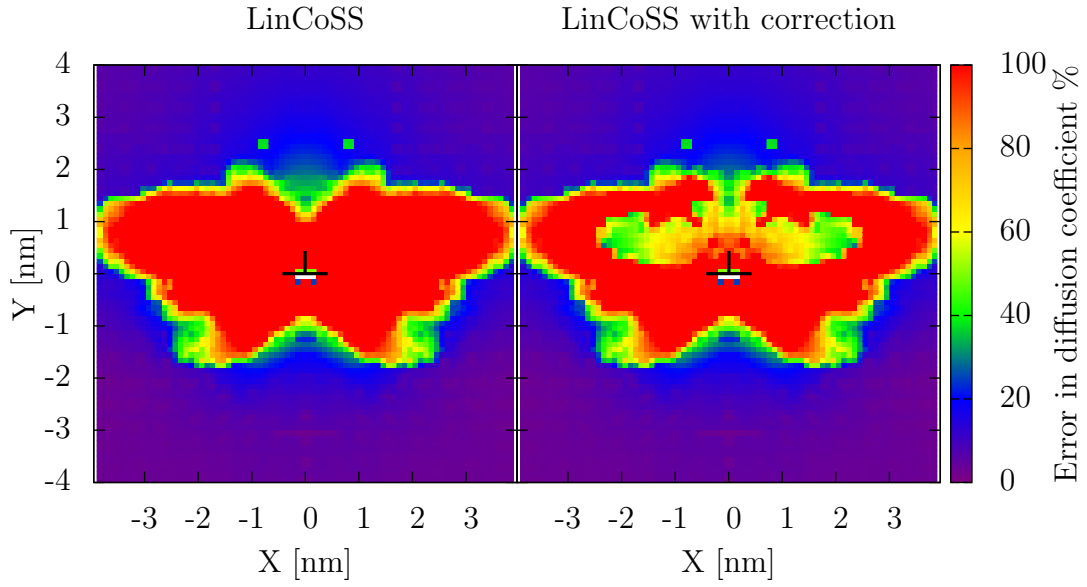


Figure D.10: Error in diffusion coefficient around an edge dislocation with and without correction in the kink zones.

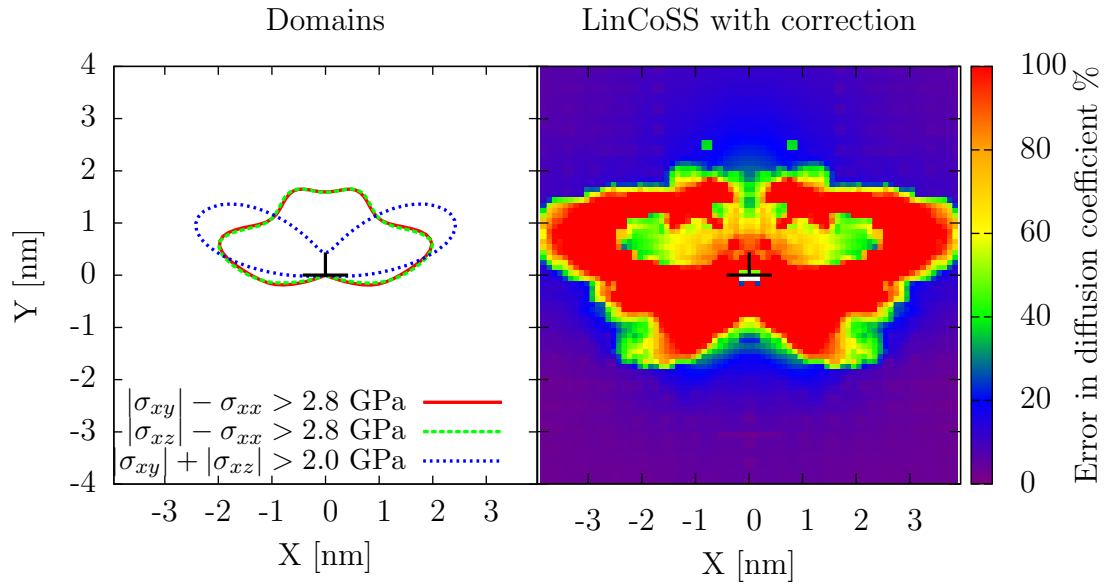


Figure D.11: Left: Zones in which the corrections are performed. Right: LinCoSS with correction

firstly due to the calculation time that would have been required, and secondly because it is not clear, whether this kink is a physical phenomenon or merely an artifact of the interatomic potential. Hence, a further investigation into this region via *ab initio* calculation is desirable.

D.4 Validity of LinCoSS: Conclusion



The error of LinCoSS with reference to CI-NEB in activation energy is not related to the stress gradient, that is present around a dislocation but not taken into account by LinCoSS. It may be partially related to the sparsely observed irregular calculation results of CI-NEB. However, the largest factor that contributed to the high error region is the kink in the activation energy landscape that appears when two stress components are varied at the same time. This also explains why the zone of validity of LinCoSS that is given in this work differs so strongly from the original article [Tchitchekova *et al.*, 2014], since it was performed only as a function of three stress components, σ_{xx} , σ_{yy} and σ_{xy} . Among these components, there is only the combination of σ_{xx} and σ_{xy} for which a kink is observed. The correction to LinCoSS that takes all the kinks into account improves the results in the zone near the dislocation line, but has no effect on the surrounding zone, where the error is still significantly high. It is likely related to the kink that would appear for higher order terms, that involve three or more stress components. However, it is not clear whether this is a physical phenomenon or merely an artifact of the interatomic potential employed in this study. Therefore, the correction to the activation energy studied in this section is not used in the AKMC simulations and the original LinCoSS is used.

Appendix E

Chemical correction library

The AKMC simulation explained in chap. 4 used LinCoSS for the activation energy calculation, which does not involve an MS/MD simulation and therefore is sufficiently fast to be incorporated into AKMC. However, LinCoSS calculates activation energies only from local stress, which means it does not take chemical interactions between C atoms into account, which NEB does on the other hand. Since it is known that the C atoms only reside in octahedral interstitial sites in bcc Fe, there are only a finite number of configurations for 2 C atoms within a certain distance. The idea of chemical correction is described as follows: Firstly, the activation energies of all possible configurations for 2 C atoms within a distance of 1 nm are calculated using LinCoSS and NEB in a small bulk simulation box. Then the difference of the values is saved in a form of a library. This library is called in the AKMC simulations, whenever there are two or more C atoms within a distance of 1 nm and added to the activation energy calculated via LinCoSS. In this section, the creation of this library as well as the method to use it in AKMC is explained.

E.1 Creation of chemical correction library

The activation energies of the C atom C_0 at (x_0, y_0, z_0) , which is a z -type site (*cf.*  in fig. E.1) having the neighboring atom C_1 at (x_1, y_1, z_1) (*cf.*  in fig. E.1) are calculated according to following procedure:

1. Create a simulation box of Fe with $15 \times 15 \times 15$ lattices.
2. Put C_1 at (x_1, y_1, z_1) and measure the stress field $\sigma_i \implies$ Calculation of activation energies E_s^{Lin} , $s = 0, \dots, 3$ via LinCoSS (*cf.* fig. E.2)

3. Put C_0 at $(x_0, y_0, z_0) \Rightarrow$ Calculation of activation energies E_s^{NEB} , $i = 0, \dots, 3$ via NEB.
4. Save the difference $E_s^{\text{chem}} = E_s^{\text{NEB}} - E_s^{\text{Lin}}$ in the array $(2(x_1 - x_0)/a_0, 2(y_1 - y_0)/a_0, 2(z_1 - z_0)/a_0) = (n_x, n_y, n_z)$ (cf. fig. E.2), where a_0 is the lattice parameter ($a_0 = 0.285531$ nm).

The activation energies are therefore saved in an array of four dimensions $E_{sn_x n_y n_z}$, in which s stands for the four possibilities of interstitial jumps and n_x, n_y, n_z stand for the position of C_1 with respect to C_0 in lattice parameter dimension.

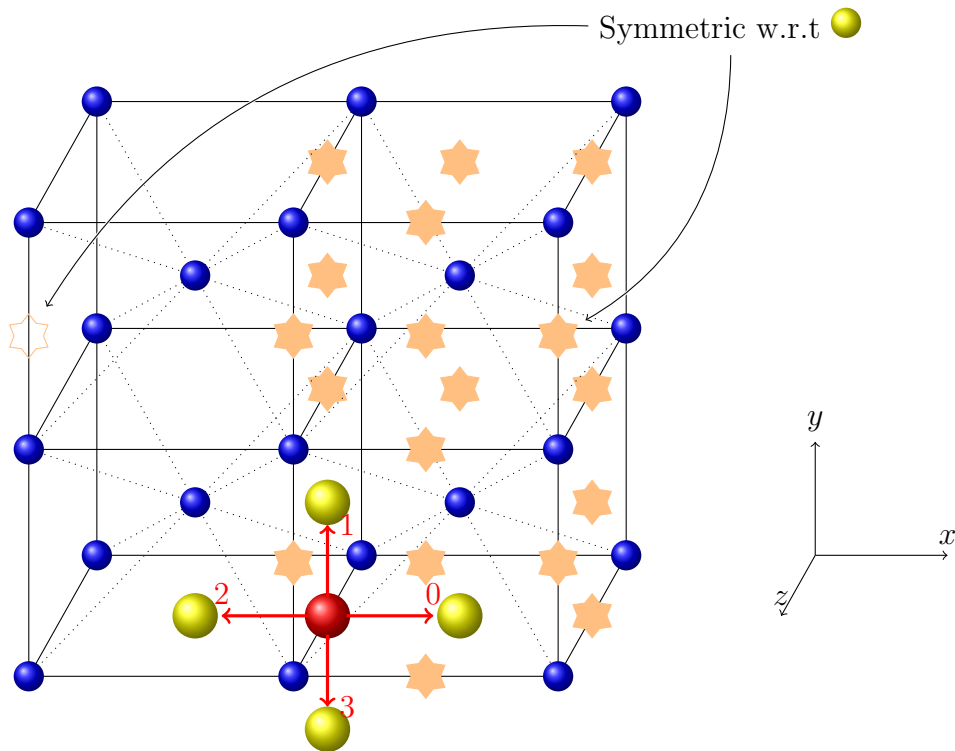


Figure E.1: How activation energies are calculated and saved for the chemical correction library. The spheres represent the C atom C_0 .

There are, however, around 4,000 neighboring octahedral interstitial sites within a distance of 1 nm. It is therefore not efficient from the computational point of view to calculate all the values in an array. Also, many of the sites are geometrically symmetric with respect to C_0 , which means they can be obtained by transforming the coordinates.

E.2 Implementation in AKMC

The calculation procedure of n_x , n_y and n_z (given in the previous section) of the chemical library $E_{sn_x n_y n_z}^{\text{chem}}$ for the C atom at $\vec{r}_0 = (x_0, y_0, z_0)$ having the neighboring C atom at $\vec{r}_1 = (x_1, y_1, z_1)$ is given by¹:

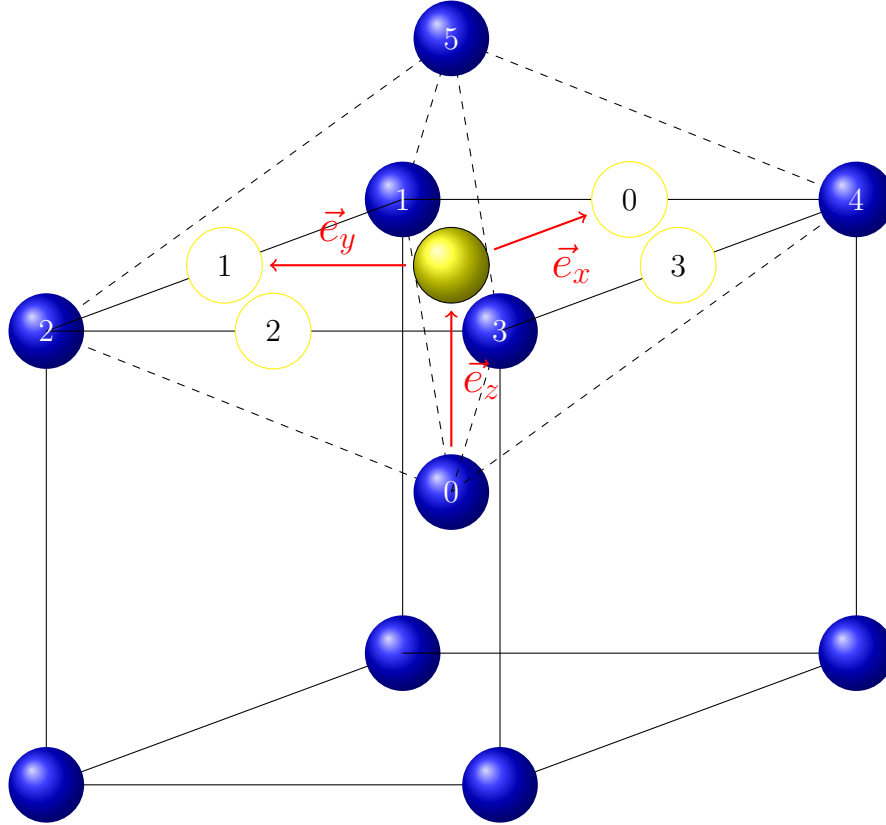


Figure E.2: The activation energies are saved as indicated as 0, 1, 2 and 3.

$$n_i = 2A_{ij} \frac{r_{0j} - r_{1j}}{a_0} \quad (\text{E.1})$$

where $i, j, k, l = x, y, z$. A_{kl} is given by:

$$A = \begin{pmatrix} \frac{1}{\sqrt{3}} & -\frac{1}{\sqrt{2}} & \frac{1}{\sqrt{6}} \\ \frac{1}{\sqrt{3}} & 0 & \frac{2}{\sqrt{6}} \\ \frac{1}{\sqrt{3}} & \frac{1}{\sqrt{2}} & \frac{1}{\sqrt{6}} \end{pmatrix} \quad (\text{E.2})$$

A accounts for the rotation due to the lattice orientation around edge and screw dislocation. n_i is therefore given in the dimension of number of lattice parameter and therefore is an array of natural numbers. Since the values in the library are

¹The axes x, y, z are enumerated as 0,1,2

saved considering C_0 being in a z -site, n_i is rotated to n'_i by:

$$n'_i = n_{(i+2-\tau_0) \bmod 3} \quad (\text{E.3})$$

where τ_0 is the site type of C_0 . The activation energies are saved according to fig. E.2 as explained in the previous section. If $n'_0 (= n'_x)$ is negative, E_0 and E_2 must be swapped. Similarly, if $n'_1 (= n'_y)$ is negative, E_1 and E_3 must be swapped. Therefore, the index s of $E_{sn_x n_y n_z}$ is changed through s' by:

$$s' = \begin{cases} \begin{cases} s & \text{if } n'_1 \geq 0 \\ 2 - s & \text{else} \end{cases} & \text{if } s = 0, 2 \\ \begin{cases} s & \text{if } n'_2 \geq 0 \\ 4 - s & \text{else} \end{cases} & \text{else} \end{cases} \quad (\text{E.4})$$

It is forbidden for any two C atoms to be within a distance of $\sqrt{2}a_0$. In order to realize it, an additional value of $E'_{s'n'_x n'_y n'_z}$ is added to the chemical correction following condition:

$$E'_{s'n'_x n'_y n'_z} = \begin{cases} 1 \text{ eV} & \text{if } \begin{cases} (n'_0 - 1, n'_1, n'_2)^2 \leq 8, s = 0 \\ (n'_0, n'_1 - 1, n'_2)^2 \leq 8, s = 1 \\ (n'_0 + 1, n'_1, n'_2)^2 \leq 8, s = 2 \\ (n'_0, n'_1 + 1, n'_2)^2 \leq 8, s = 3 \end{cases} \\ 0 & \text{else} \end{cases} \quad (\text{E.5})$$

In total, the chemical correction E_{chem} is given by:

$$E_{\text{chem}} = E_{s'|n'_x||n'_y||n'_z}^{\text{chem}} + E'_{s'n'_x n'_y n'_z} \quad (\text{E.6})$$

Appendix F

Elastic correction library

The chemical interactions are added to the activation energies calculated via LinCoSS. Since LinCoSS converts local stress into activation energies, the information on the local stress in the presence of the neighboring C atoms is required. This could be obtained by removing the C atom from the simulation box, for which the activation energies are calculated, and relaxing the simulation box. However, since an energy minimization requires a lengthy MS calculation, it is not realistic to incorporate it into AKMC. As stated in the previous section, there are only a countable number of arrangements of two C atoms within 1 nm in bcc-Fe. Therefore the idea of elastic correction library is to calculate the stress field around one C atom in a bulk simulation box in advance, and add it to the local stress field of C atoms in AKMC simulations, assuming that the stress created by a C atom and the stress created by the dislocation are additive.

F.1 Creation of elastic correction library

The stress field created by one C atom is calculated and saved according to the following procedure:

1. Create a bulk simulation box of Fe with $15 \times 15 \times 15$ lattices.
2. Put a C at (x_0, y_0, z_0) which is a z -type site \implies Relaxation of simulation box.
3. Measure stress field $\sigma_{n_x n_y n_z}^{ij}$ after relaxation, where x, y, z stand for the position of neighboring octahedral interstitial sites and $i, j = x, y, z$ in the array $(2(x - x_0)/a_0, 2(y - y_0)/a_0, 2(z - z_0)/a_0) = (n_x, n_y, n_z)$ (cf. fig. E.2), where a_0 is the lattice parameter ($a_0 = 0.285531$ nm).

F.2 Implementation in AKMC

For the C atom C_0 at position $\vec{r}_0 = (x_0, y_0, z_0)$ of site type τ_0 having a neighboring C atom C_1 at $\vec{r}_1 = (x_1, y_1, z_1)$ the calculation of n_i is performed by:

$$n_i = 2A_{ij} \frac{r_{1j} - r_{0j}}{a_0} \quad (\text{F.1})$$

Since the values in the library are saved considering C_0 being in a z -site, n_i is rotated to n'_i by

$$n'_i = n_{(i+2-\tau_0) \bmod 3} \quad (\text{F.2})$$

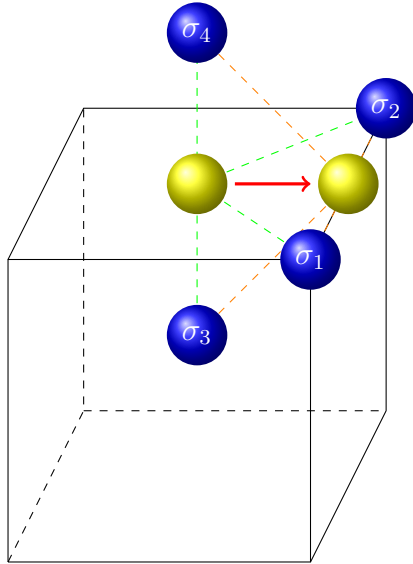


Figure F.1: Interstitial jump of a C atom (yellow sphere). From the Fe atoms depicted (blue spheres), the stress value is calculated and the mean value is taken.

where sgn is sign function, which gives 1 if the argument is positive or zero, and -1 if the argument is negative.

As explained in chap. 1 sec. 1.4.2, the stress field for a C atom to calculate an activation energy is taken from the average stress of the four nearest Fe atoms from the interstitial jump (*cf.* fig. F.1). Depending on the relative site type¹ of C_1 with respect to C_2 , the calculation changes. Therefore, from the stress library $\sigma_{n_x n_y n_z}^{ij}$, the stresses are taken as follows:

¹The *relative site type* is determined considering the site type of C_1 as z , *i.e.* if the site type of C_1 is indeed z , then the site type of C_0 is the same as its relative site type. If *e.g.* the site type of C_1 is x and the site type of C_0 is x , the relative site type of C_1 is z , since both C_0 and C_1 have the same site type.

If the relative site type is x :

$$\sigma_1^{ij} = \sigma_{n'_x+1, n'_y, n'_z}^{ij} + \sigma_{n'_x-1, n'_y, n'_z}^{ij} + \sigma_{n'_x, n'_y+\text{sgn}(n'_y), n'_z+\text{sgn}(n'_z)}^{ij} + \sigma_{n'_x, n'_y+\text{sgn}(n'_y), n'_z-\text{sgn}(n'_z)}^{ij} \quad (\text{F.3})$$

$$\sigma_2^{ij} = \sigma_{n'_x+1, n'_y, n'_z}^{ij} + \sigma_{n'_x-1, n'_y, n'_z}^{ij} + \sigma_{n'_x, n'_y+\text{sgn}(n'_y), n'_z+\text{sgn}(n'_z)}^{ij} + \sigma_{n'_x, n'_y-\text{sgn}(n'_y), n'_z+\text{sgn}(n'_z)}^{ij} \quad (\text{F.4})$$

$$\sigma_3^{ij} = \sigma_{n'_x+1, n'_y, n'_z}^{ij} + \sigma_{n'_x-1, n'_y, n'_z}^{ij} + \sigma_{n'_x, n'_y-\text{sgn}(n'_y), n'_z+\text{sgn}(n'_z)}^{ij} + \sigma_{n'_x, n'_y-\text{sgn}(n'_y), n'_z-\text{sgn}(n'_z)}^{ij} \quad (\text{F.5})$$

$$\sigma_4^{ij} = \sigma_{n'_x+1, n'_y, n'_z}^{ij} + \sigma_{n'_x-1, n'_y, n'_z}^{ij} + \sigma_{n'_x, n'_y+\text{sgn}(n'_y), n'_z-\text{sgn}(n'_z)}^{ij} + \sigma_{n'_x, n'_y-\text{sgn}(n'_y), n'_z-\text{sgn}(n'_z)}^{ij} \quad (\text{F.6})$$

If the relative site type is y :

$$\sigma_1^{ij} = \sigma_{n'_x, n'_y, n'_z+1}^{ij} + \sigma_{n'_x, n'_y, n'_z-1}^{ij} + \sigma_{n'_x+\text{sgn}(n'_x), n'_y+\text{sgn}(n'_y), n'_z}^{ij} + \sigma_{n'_x+\text{sgn}(n'_x), n'_y-\text{sgn}(n'_y), n'_z}^{ij} \quad (\text{F.7})$$

$$\sigma_2^{ij} = \sigma_{n'_x, n'_y, n'_z+1}^{ij} + \sigma_{n'_x, n'_y, n'_z-1}^{ij} + \sigma_{n'_x+\text{sgn}(n'_x), n'_y+\text{sgn}(n'_y), n'_z}^{ij} + \sigma_{n'_x-\text{sgn}(n'_x), n'_y+\text{sgn}(n'_y), n'_z}^{ij} \quad (\text{F.8})$$

$$\sigma_3^{ij} = \sigma_{n'_x, n'_y, n'_z+1}^{ij} + \sigma_{n'_x, n'_y, n'_z-1}^{ij} + \sigma_{n'_x-\text{sgn}(n'_x), n'_y+\text{sgn}(n'_y), n'_z}^{ij} + \sigma_{n'_x-\text{sgn}(n'_x), n'_y-\text{sgn}(n'_y), n'_z}^{ij} \quad (\text{F.9})$$

$$\sigma_4^{ij} = \sigma_{n'_x, n'_y, n'_z+1}^{ij} + \sigma_{n'_x, n'_y, n'_z-1}^{ij} + \sigma_{n'_x+\text{sgn}(n'_x), n'_y-\text{sgn}(n'_y), n'_z}^{ij} + \sigma_{n'_x-\text{sgn}(n'_x), n'_y-\text{sgn}(n'_y), n'_z}^{ij} \quad (\text{F.10})$$

If the relative site type is z :

$$\sigma_1^{ij} = \sigma_{n'_x, n'_y+1, n'_z}^{ij} + \sigma_{n'_x, n'_y-1, n'_z}^{ij} + \sigma_{n'_x+\text{sgn}(n'_x), n'_y, n'_z+\text{sgn}(n'_z)}^{ij} + \sigma_{n'_x-\text{sgn}(n'_x), n'_y, n'_z+\text{sgn}(n'_z)}^{ij} \quad (\text{F.11})$$

$$\sigma_2^{ij} = \sigma_{n'_x, n'_y+1, n'_z}^{ij} + \sigma_{n'_x, n'_y-1, n'_z}^{ij} + \sigma_{n'_x+\text{sgn}(n'_x), n'_y, n'_z+\text{sgn}(n'_z)}^{ij} + \sigma_{n'_x+\text{sgn}(n'_x), n'_y, n'_z-\text{sgn}(n'_z)}^{ij} \quad (\text{F.12})$$

$$\sigma_3^{ij} = \sigma_{n'_x, n'_y+1, n'_z}^{ij} + \sigma_{n'_x, n'_y-1, n'_z}^{ij} + \sigma_{n'_x+\text{sgn}(n'_x), n'_y, n'_z-\text{sgn}(n'_z)}^{ij} + \sigma_{n'_x-\text{sgn}(n'_x), n'_y, n'_z-\text{sgn}(n'_z)}^{ij} \quad (\text{F.13})$$

$$\sigma_4^{ij} = \sigma_{n'_x, n'_y+1, n'_z}^{ij} + \sigma_{n'_x, n'_y-1, n'_z}^{ij} + \sigma_{n'_x-\text{sgn}(n'_x), n'_y, n'_z+\text{sgn}(n'_z)}^{ij} + \sigma_{n'_x-\text{sgn}(n'_x), n'_y, n'_z-\text{sgn}(n'_z)}^{ij} \quad (\text{F.14})$$

As explained in chap. 1 sec. 1.4.2, since the activation energy is calculated by LinCoSS for a C atom going from a z -type site to a y -type site, a transformation of coordinate system has to be performed for the stress depending on the site type.

Let S matrix that transforms vector \vec{r} that is given in the coordinate system Σ into vector \vec{r}' that is given in another coordinate system Σ' (*i.e.* $S\vec{r} = \vec{r}'$), then the stress σ' which is given in the coordinate system Σ is given in the coordinate system Σ' by:

$$\sigma' = S^T \sigma S \quad (\text{F.15})$$

where S^T is the transposed matrix of S .

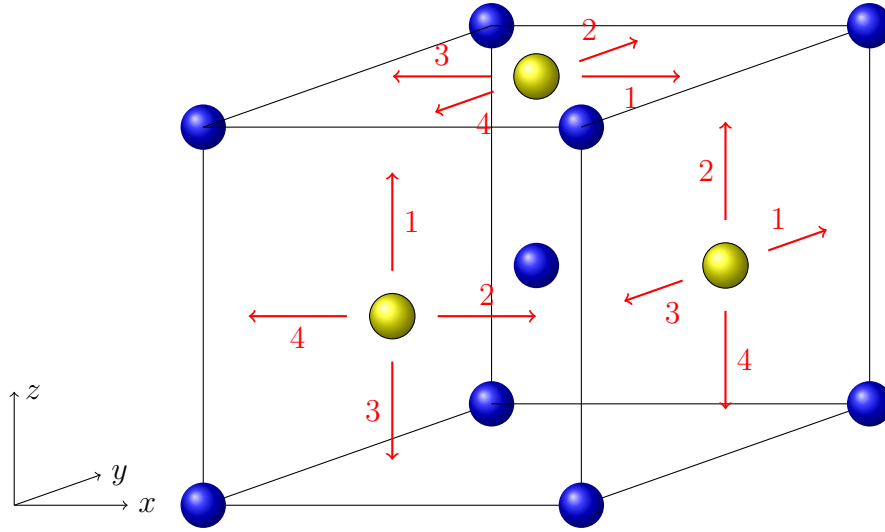


Figure F.2: Enumeration of interstitial jumps in different types of sites

S_i , where the index denotes the enumeration of interstitial jump (*cf.* fig. F.2), are calculated depending on the relative site type:

If the relative site type is x :

$$S_1 = \begin{pmatrix} 0 & 1 & 0 \\ 0 & 0 & 1 \\ 1 & 0 & 0 \end{pmatrix} \quad S_2 = \begin{pmatrix} 0 & 0 & 1 \\ 0 & 1 & 0 \\ 1 & 0 & 0 \end{pmatrix} \quad (\text{F.16})$$

If the relative site type is y :

$$S_1 = \begin{pmatrix} 1 & 0 & 0 \\ 0 & 1 & 0 \\ 0 & 0 & 1 \end{pmatrix} \quad S_2 = \begin{pmatrix} 0 & 0 & 1 \\ 0 & 1 & 0 \\ 1 & 0 & 0 \end{pmatrix} \quad (\text{F.17})$$

If the relative site type is z :

$$S_1 = \begin{pmatrix} 1 & 0 & 0 \\ 0 & 1 & 0 \\ 0 & 0 & 1 \end{pmatrix} S_2 = \begin{pmatrix} 0 & 1 & 0 \\ 1 & 0 & 0 \\ 0 & 0 & 1 \end{pmatrix} \quad (\text{F.18})$$

In all cases $S_2 = S_0$ and $S_3 = S_1$, since LinCoSS is symmetric with respect to the change of sign.

Bibliography

- N H Abel, L Sylow, and S Lie. *Oeuvres completes*, volume 1. Grøndahl & søn, 1881.
- G J Ackland, M I Mendeleev, D J Srolovitz, S Han, and A V Barashev. Development of an interatomic potential for phosphorus impurities in α -iron. *Journal of Physics: Condensed Matter*, 16(27):S2629, 2004.
- V Afshari and C Dehghanian. Effects of grain size on the electrochemical corrosion behaviour of electrodeposited nanocrystalline Fe coatings in alkaline solution. *Corrosion Science*, 51(8):1844–1849, 2009.
- A Al Mazouzi, A Alamo, D Lidbury, D Moinereau, and S Van Dyck. Perform 60: Prediction of the effects of radiation for reactor pressure vessel and in-core materials using multi-scale modelling–60 years foreseen plant lifetime. *Nuclear Engineering and Design*, 241(9):3403–3415, 2011.
- D J Bacon, D M Barnett, and R O Scattergood. Anisotropic continuum theory of lattice defects. *Progress in Materials Science*, 23:51 – 262, 1980.
- A Ballesteros, R Ahlstrand, C Bruynooghe, U von Estorff, and L Debarberis. The role of pressure vessel embrittlement in the long term operation of nuclear power plants. *Nuclear Engineering and Design*, 243:63–68, 2012.
- G T Barkema and N Mousseau. Event-based relaxation of continuous disordered systems. *Phys. Rev. Lett.*, 77:4358–4361, Nov 1996.
- C S Barrett. *Structure of metals*. McGraw-Hill Book Company, Inc.; New York, New York, 1943.
- E Bauer-Grosse. Thermal stability and crystallization studies of amorphous tm-c films. *Thin Solid Films*, 447–448:311 – 315, 2004. Proceedings of the 30th International Conference on Metallurgical Coatings and Thin Films.

- C S Becquart, J M Raulot, G Bencteux, C Domain, M Perez, S Garruchet, and H Nguyen. Atomistic modeling of an Fe system with a small concentration of C. *Computational Materials Science*, 40(1):119 – 129, 2007.
- J Belotteau, C Berdin, S Forest, A Parrot, and C Prioul. Mechanical behavior and crack tip plasticity of a strain aging sensitive steel. *Materials Science and Engineering: A*, 526(1):156–165, 2009.
- E Bitzek, P M Derlet, P M Anderson, and H Van Swygenhoven. The stress-strain response of nanocrystalline metals: a statistical analysis of atomistic simulations. *Acta Materialia*, 56(17):4846–4857, 2008.
- K Boylan, D Ostrander, U Erb, G Palumbo, and K T Aust. An in-situ tem study of the thermal stability of nanocrystalline Ni P. *Scripta metallurgica et materialia*, 25(12):2711–2716, 1991.
- E M Bringa, A Caro, Y Wang, M Victoria, J M McNaney, B A Remington, R F Smith, B R Torralva, and H Van Swygenhoven. Ultrahigh strength in nanocrystalline materials under shock loading. *Science*, 309(5742):1838–1841, 2005.
- W Cai, R B Sills, D M Barnett, and W D Nix. Modeling a distribution of point defects as misfitting inclusions in stressed solids. *Journal of the Mechanics and Physics of Solids*, 66:154–171, 2014.
- D Caillard and J Bonneville. Dynamic strain aging caused by a new peierls mechanism at high-temperature in iron. *Scripta Materialia*, 95:15–18, 2015.
- Elisa Cantergiani, Amélie Fillon, Ben Lawrence, Xavier Sauvage, Michel Perez, Colin P Scott, and Arnaud Weck. Tailoring the mechanical properties of steel sheets using fec films and diffusion annealing. *Materials Science and Engineering: A*, 657:291–298, 2016.
- C Castro, M Pinault, S Coste-Leconte, D Porterat, N Bendiab, C Reynaud, and M Mayne-L’Hermite. Dynamics of catalyst particle formation and multi-walled carbon nanotube growth in aerosol-assisted catalytic chemical vapor deposition. *Carbon*, 48(13):3807 – 3816, 2010.
- L Cheng, C M Brakman, B M Korevaar, and E J Mittemeijer. The tempering of iron-carbon martensite; dilatometric and calorimetric analysis. *Metallurgical Transactions A*, 19(10):2415–2426, 1988.

- P V Chirkov, A A Mirzoev, and D A Mirzaev. Molecular-dynamics simulations of carbon ordering in bcc Fe and its impact on martensite transition. *Materials Today: Proceedings*, 2:S553–S556, 2015.
- E Clouet, S Garruchet, H Nguyen, M Perez, and C S Becquart. Dislocation interaction with C in α -Fe: A comparison between atomic simulations and elasticity theory. *Acta Materialia*, 56(14):3450–3460, 2008.
- E Clouet, L Ventelon, and F Willaime. Dislocation core energies and core fields from first principles. *Phys. Rev. Lett.*, 102:055502, Feb 2009.
- E Clouet, L Ventelon, and F Willaime. Dislocation core field. ii. screw dislocation in iron. *Physical Review B*, 84(22):224107, 2011.
- A W Cochardt, G Schoek, and H Wiedersich. Interaction between dislocations and interstitial atoms in body-centered cubic metals. *Acta metallurgica*, 3(6):533–537, 1955.
- A H Cottrell and B A Bilby. Dislocation theory of yielding and strain ageing of iron. *Proceedings of the Physical Society. Section A*, 62(1):49, 1949.
- A H Cottrell. Report of a conference on strength of solids. *Physical Society, London*, 30, 1948.
- J R G Da Silva and R B McLellan. Diffusion of carbon and nitrogen in bcc iron. *Materials Science and Engineering*, 26(1):83–87, 1976.
- A K De, S Vandeputte, and B C De Cooman. Static strain aging behavior of ultra low carbon bake hardening steel. *Scripta materialia*, 41(8):831–837, 1999.
- A K De, K De Blauwe, S Vandeputte, and B C De Cooman. Effect of dislocation density on the low temperature aging behavior of an ultra low carbon bake hardening steel. *Journal of Alloys and Compounds*, 310(1):405–410, 2000.
- A K De, S Vandeputte, and B C De Cooman. Kinetics of low temperature precipitation in a ULC-bake hardening steel. *Scripta materialia*, 44(4):695–700, 2001.
- A J Detor and C A Schuh. Grain boundary segregation, chemical ordering and stability of nanocrystalline alloys: Atomistic computer simulations in the Ni–W system. *Acta Materialia*, 55(12):4221–4232, 2007.
- A M El-Sherik and U Erb. Synthesis of bulk nanocrystalline nickel by pulsed electrodeposition. *Journal of Materials Science*, 30(22):5743–5749, 1995.

- U Erb. Electrodeposited nanocrystals: synthesis, properties and industrial applications. *Nanostructured Materials*, 6(5):533–538, 1995.
- J D Eshelby, W T Read, and W Shockley. Anisotropic elasticity with applications to dislocation theory. *Acta Metallurgica*, 1(3):251 – 259, 1953.
- T S Eyre and A Baxter. The formation of white layers at rubbing surfaces. *Tribology*, 5(6):256–261, 1972.
- H I Faraoun, Y D Zhang, C Esling, and H Aourag. Crystalline, electronic, and magnetic structures of θ -Fe₃C, χ -Fe₅C₂, and η -Fe₂C from first principle calculation. *Journal of applied physics*, 99(9):093508, 2006.
- M W Finnis and J E Sinclair. A simple empirical n-body potential for transition metals. *Philosophical Magazine A*, 50(1):45–55, 1984.
- D Frenkel and B Smit. Understanding molecular simulations: from algorithms to applications. *Academic, San Diego*, 1996.
- M Fukuhara and A Sanpei. Elastic moduli and internal friction of low carbon and stainless steels as a function of temperature. *ISIJ international*, 33(4):508–512, 1993.
- S Garruchet and M Perez. Modelling the carbon snoek peak in ferrite: Coupling molecular dynamics and kinetic monte-carlo simulations. *Computational Materials Science*, 43(2):286–292, 2008.
- H Gleiter. Nanostructured materials: basic concepts and microstructure. *Acta materialia*, 48(1):1–29, 2000.
- G Gulino, R Vieira, J Amadou, P Nguyen, M J Ledoux, S Galvagno, G Centi, and C Pham-Huu. c_2h_6 as an active carbon source for a large scale synthesis of carbon nanotubes by chemical vapour deposition. *Applied Catalysis A: General*, 279(1–2):89 – 97, 2005.
- K Hamad-Schifferli, J J Schwartz, A T Santos, S Zhang, and J M Jacobson. Remote electronic control of DNA hybridization through inductive coupling to an attached metal nanocrystal antenna. *Nature*, 415(6868):152–155, 2002.
- Y Hanlummyuang, P A Gordon, T Neeraj, and D C Chrzan. Interactions between carbon solutes and dislocations in bcc iron. *Acta Materialia*, 58(16):5481–5490, 2010.

- G Henkelman and H Jónsson. Improved tangent estimate in the nudged elastic band method for finding minimum energy paths and saddle points. *The Journal of Chemical Physics*, 113(22):9978–9985, 2000.
- G Henkelman, B P Uberuaga, and H Jónsson. A climbing image nudged elastic band method for finding saddle points and minimum energy paths. *The Journal of Chemical Physics*, 113(22):9901–9904, 2000.
- J P Hirth and J Lothe. *Theory of dislocations*. McGraw-Hill Book Company, 1968.
- D E Jiang and Emily A Carter. Carbon dissolution and diffusion in ferrite and austenite from first principles. *Physical Review B*, 67(21):214103, 2003.
- I Jouanny, V Demange, J Ghanbaja, and E Bauer-Grosse. Structural characterization of Fe–C coatings prepared by reactive triode-magnetron sputtering. *Journal of Materials Research*, 25(09):1859–1869, 2010.
- K Kamber, D Keefer, and C Wert. Interactions of interstitials with dislocations in iron. *Acta Metallurgica*, 9(5):403–414, May 1961.
- M Kehoe and P M Kelly. The role of carbon in the strength of ferrous martensite. *Scripta Metallurgica*, 4(6):473 – 476, 1970.
- A G Khachaturian and G A Shatalov. K teorii uporyadocheniya atomov ugleroda v kristalle martensita. *Fizika metallov i metallovedenie*, 32(1):5, 1955.
- A G Khachaturyan. Theory of phase transformations in solids. *John Wiley & Sons, New York, NY*, 1983.
- H A Khater, G Monnet, D Terentyev, and A Serra. Dislocation glide in Fe–carbon solid solution: from atomistic to continuum level description. *International Journal of Plasticity*, 62:34–49, 2014.
- R Khatirkar, K V Mani Krishna, L Kestens, R H Petrov, P Pant, and I Samajdar. Strain localizations in ultra low carbon steel. In *Materials Science Forum*, volume 702, pages 782–785. Trans Tech Publ, 2012.
- R Kirchheim. Grain coarsening inhibited by solute segregation. *Acta Materialia*, 50(2):413–419, 2002.
- L Kong, X Li, W Lai, J Liu, and B Liu. Interfacial reaction of W/Cu examined by an n-body potential through molecular dynamics simulations. *Japanese journal of applied physics*, 41(7R):4503, 2002.

- A Königer, C Hammerl, M Zeitler, and B Rauschenbach. Formation of metastable iron carbide phases after high-fluence carbon ion implantation into iron at low temperatures. *Phys. Rev. B*, 55:8143–8147, Apr 1997.
- G Krauss. Martensite in steel: strength and structure. *Materials Science and Engineering: A*, 273–275:40 – 57, 1999.
- L P Kubin, Y Estrin, and C Perrier. On static strain ageing. *Acta metallurgica et materialia*, 40(5):1037–1044, 1992.
- G V Kurdjumov and A G Khachaturyan. Phenomena of carbon atom redistribution in martensite. *Metallurgical Transactions*, 3(5):1069–1076, 1972.
- G V Kurdjumov and A G Khachaturyan. Nature of axial ratio anomalies of the martensite lattice and mechanism of diffusionless $\gamma \rightarrow \alpha$ transformation. *Acta Metallurgica*, 23(9):1077–1088, 1975.
- T T Lau, C J Först, X Lin, J D Gale, S Yip, and K J Van Vliet. Many-body potential for point defect clusters in Fe-c alloys. *Physical review letters*, 98(21):215501, 2007.
- N Lavaire, J Merlin, and V Sardoy. Study of ageing in strained ultra and extra low carbon steels by thermoelectric power measurement. *Scripta materialia*, 44(4):553–559, 2001.
- N Lavaire. *Etude des phénomènes à l'origine du vieillissement des aciers pour emballage à Ultra Bas Carbone (ULC): apport du pouvoir thermo-électrique à la caractérisation des états microstructuraux*. PhD thesis, Institut National des Sciences Appliquées de Lyon, 2001.
- B Lawrence, C W Sinclair, and M Perez. Carbon diffusion in supersaturated ferrite: a comparison of mean-field and atomistic predictions. *Modelling and Simulation in Materials Science and Engineering*, 22(6):065003, 2014.
- E Lindstrand. A method for the measurement of elastic relaxation, and its use for determination of the solubility of carbon in α -iron. *Acta Metallurgica*, 3(5):431–435, 1955.
- F Liu and R Kirchheim. Nano-scale grain growth inhibited by reducing grain boundary energy through solute segregation. *Journal of crystal growth*, 264(1):385–391, 2004.

- Q Liu and S Zhao. Cu precipitation on dislocation and interface in quench-aged steel. *MRS Communications*, 2(04):127–132, 2012.
- W Lojkowski, M Djahanbakhsh, G Bürkle, S Gierlotka, W Zielinski, and H J Fecht. Nanostructure formation on the surface of railway tracks. *Materials Science and Engineering: A*, 303(1):197–208, 2001.
- L Y Lyssak and Y N Vovk. On the nature of phase transformations during hardening manganese steel. *The Physics of Metals and Metallography*, 20(4):540–546, 1965.
- V Massardier, N Lavaire, M Soler, and J Merlin. Comparison of the evaluation of the carbon content in solid solution in extra-mild steels by thermoelectric power and by internal friction. *Scripta Materialia*, 50(12):1435–1439, June 2004.
- R B McLellan and M L Wasz. Carbon diffusivity in bcc iron. *Journal of Physics and Chemistry of Solids*, 54(5):583–586, 1993.
- M A Meyers, A Mishra, and D J Benson. Mechanical properties of nanocrystalline materials. *Progress in materials science*, 51(4):427–556, 2006.
- M K Miller, E A Kenik, K F Russell, L Heatherly, D T Hoelzer, and P J Maziasz. Atom probe tomography of nanoscale particles in ODS ferritic alloys. *Materials Science and Engineering: A*, 353(1-2):140–145, July 2003.
- S Morito, J Nishikawa, and T Maki. Dislocation density within lath martensite in Fe-C and Fe-Ni alloys. *ISIJ international*, 43(9):1475–1477, 2003.
- G J Moyar and D H Stone. An analysis of the thermal contributions to railway wheel shelling. *Wear*, 144(1):117–138, 1991.
- G A Nematollahi, B Grabowski, D Raabe, and J Neugebauer. Multiscale description of carbon-supersaturated ferrite in severely drawn pearlitic wires. *Acta Materialia*, 111:321–334, 2016.
- Q H Nguyen. *Etude numérique de l'interaction des hétéro interstitiels avec la dislocation dans le α -Fe*. PhD thesis, Université Lille, 2009.
- W J Parak, D Gerion, T Pellegrino, D Zanchet, C Micheel, S C Williams, R Boudreau, M A Le Gros, C A Larabell, and A P Alivisatos. Biological applications of colloidal nanocrystals. *Nanotechnology*, 14(7):R15, 2003.

- J Pešička, R Kužel, A Dronhofer, and G Eggeler. The evolution of dislocation density during heat treatment and creep of tempered martensite ferritic steels. *Acta materialia*, 51(16):4847–4862, 2003.
- A Portevin and F Le Chatelier. Sur un phénomène observé lors de l’essai de traction d’alliages en cours de transformation. *Comptes Rendus de l’Académie des Sciences Paris*, 176:507–510, 1923.
- G P P Pun, K A Darling, L J Kecskes, and Y Mishin. Angular-dependent inter-atomic potential for the Cu–Ta system and its application to structural stability of nano-crystalline alloys. *Acta Materialia*, 100:377–391, 2015.
- D Raabe, P Klose, B Engl, K P Imlau, F Friedel, and F Roters. Concepts for integrating plastic anisotropy into metal forming simulations. *Advanced Engineering Materials*, 4(4):169, 2002.
- K Renard, S Ryelandt, and P J Jacques. Characterisation of the Portevin-le Châtelier effect affecting an austenitic TWIP steel based on digital image correlation. *Materials Science and Engineering: A*, 527(12):2969–2977, 2010.
- W C Roberts-Austen. Fourth report to the alloys research committee. *Proceedings of the Institution of Mechanical Engineers*, 52(1):31–100, 1897.
- A L Roitburd and A G Khachaturyan. Interstitial atoms and crystallographic mechanism of the martensite transformation in steels. *FIZIKA METALLOV METALLOVEDENIE*, 30(6):1189–1199, 1970.
- A V Ruban. Self-trapping of carbon atoms in α' -Fe during the martensitic transformation: A qualitative picture from ab initio calculations. *Physical Review B*, 90(14):144106, 2014.
- C P Scott, C Sinclair, and A Weck. Amorphous Fe 1- x c x coatings as carbon reservoirs for diffusion strengthening of steel sheets. *Scripta Materialia*, 65(9):763–766, 2011.
- D Sheppard, R Terrell, and G Henkelman. Optimization methods for finding minimum energy paths. *The Journal of chemical physics*, 128(13):134106, 2008.
- D H Sherman, S M Cross, S Kim, F Grandjean, G J Long, and M K Miller. Characterization of the carbon and retained austenite distributions in martensitic medium carbon, high silicon steel. *Metallurgical and Materials Transactions A*, 38(8):1698–1711, 2007.

- C W Sinclair, M Perez, R G A Veiga, and A Weck. Molecular dynamics study of the ordering of carbon in highly supersaturated α -Fe. *Physical Review B*, 81(22):224204, 2010.
- B Soenen, A K De, S Vandeputte, and B C De Cooman. Competition between grain boundary segregation and cottrell atmosphere formation during static strain aging in ultra low carbon bake hardening steels. *Acta materialia*, 52(12):3483–3492, 2004.
- J L Strudel, P Groh, L P Kubin, and J L Martin. Dislocations et déformation plastique. *Ecole d'été d'Yrvals, Ed. de Physique*, 1979.
- S Takebayashi, T Kunieda, N Yoshinaga, K Ushioda, and S Ogata. Comparison of the dislocation density in martensitic steels evaluated by some x-ray diffraction methods. *ISIJ international*, 50(6):875–882, 2010.
- K Tapasa, Y N Osetsky, and D J Bacon. Computer simulation of interaction of an edge dislocation with a carbon interstitial in α -iron and effects on glide. *Acta materialia*, 55(1):93–104, 2007.
- L Tau and C O Bennett. Reaction of carbon monoxide/hydrogen over an iron/carbon catalyst. *The Journal of Physical Chemistry*, 90(20):4825–4832, 1986.
- K A Taylor, L Chang, G B Olson, G D W Smith, M Cohen, and J B Van der Sande. Spinodal decomposition during aging of Fe-Ni-C martensites. *Metallurgical Transactions A*, 20(12):2717–2737, 1989.
- D S Tchitchekova, J Morthomas, F Ribeiro, R Ducher, and M Perez. A novel method for calculating the energy barriers for carbon diffusion in ferrite under heterogeneous stress. *The Journal of Chemical Physics*, 141(3):–, 2014.
- G G Tibbetts. Diffusivity of carbon in iron and steels at high temperatures. *Journal of Applied Physics*, 51(9):4813–4816, 1980.
- A Udyansky, J Von Pezold, V N Bugaev, M Friák, and J Neugebauer. Interplay between long-range elastic and short-range chemical interactions in Fe-C martensite formation. *Physical Review B*, 79(22):224112, 2009.
- M J Van Genderen, A Böttger, R J Cernik, and E J Mittemeijer. Early stages of decomposition in iron-carbon and iron-nitrogen martensites: Diffraction analysis using synchrotron radiation. *Metallurgical Transactions A*, 24(9):1965–1973, 1993.

- R G A Veiga, M Perez, C S Becquart, C Domain, and S Garruchet. Effect of the stress field of an edge dislocation on carbon diffusion in α -iron: coupling molecular statics and atomistic kinetic monte carlo. *Physical Review B*, 82(5):054103, 2010.
- R G A Veiga, M Perez, C S Becquart, E Clouet, and C Domain. Comparison of atomistic and elasticity approaches for carbon diffusion near line defects in α -iron. *Acta Materialia*, 59(18):6963–6974, October 2011.
- R G A Veiga, M Perez, C S Becquart, and C Domain. Atomistic modeling of carbon cottrell atmospheres in bcc iron. *Journal of Physics: Condensed Matter*, 25(2):025401, 2012.
- R G A Veiga, C S Becquart, and M Perez. Comments on “atomistic modeling of an Fe system with a small concentration of c”. *Computational Materials Science*, 82:118–121, 2014.
- R G A Veiga, H Goldenstein, M Perez, and C S Becquart. Monte carlo and molecular dynamics simulations of screw dislocation locking by cottrell atmospheres in low carbon Fe–C alloys. *Scripta Materialia*, 108:19, 2015.
- R G A Veiga. *Computational insights into the strain aging phenomenon in bcc iron at the atomic scale*. PhD thesis, Institut National des Sciences Appliquées de Lyon, 2011.
- L Ventelon, B Lüthi, E Clouet, L Proville, B Legrand, D Rodney, and F Willaime. Dislocation core reconstruction induced by carbon segregation in bcc iron. *Physical Review B*, 91(22):220102, 2015.
- S Vepřek, P Nesladek, A Niederhofer, F Glatz, M Jilek, and M Šima. Recent progress in the superhard nanocrystalline composites: towards their industrialization and understanding of the origin of the superhardness. *Surface and Coatings Technology*, 108:138–147, 1998.
- L Verlet. Computer” experiments” on classical fluids. i. thermodynamical properties of lennard-jones molecules. *Physical review*, 159(1):98, 1967.
- A F Voter. Introduction to the kinetic monte carlo method. In *Radiation Effects in Solids*, pages 1–23. Springer, 2007.
- H Wang, Y Liang, M Gong, Y Li, W Chang, T Mefford, J Zhou, J Wang, T Regier, and F Wei. An ultrafast nickel-iron battery from strongly coupled

- inorganic nanoparticle/nanocarbon hybrid materials. *Nature communications*, 3:917, 2012.
- A Weck, C W Sinclair, C P Scott, and C Maunder. Supersaturated α -iron in vapour-deposited Fe-c thin films. *Journal of Materials Science*, 47(19):6939–6947, 2012.
- J Weissmüller. Alloy effects in nanostructures. *Nanostructured Materials*, 3(1):261–272, 1993.
- J Weissmuller. Synthesis and processing of nanocrystalline powder. *TMS, Warrendale, PA*, 3, 1996.
- C Wert and C Zener. Interstitial atomic diffusion coefficients. *Phys. Rev.*, 76:1169–1175, Oct 1949.
- C A Wert. Diffusion coefficient of C in α -iron. *Physical Review*, 79(4):601, 1950.
- J Wilde, A Cerezo, and G D W Smith. Three-dimensional atomic-scale mapping of a cottrell atmosphere around a dislocation in iron. *Scripta Materialia*, 43(1):39, 2000.
- D V Wilson and B Russell. The contribution of atmosphere locking to the strain-ageing of low carbon steels. *Acta metallurgica*, 8(1):36–45, 1960.
- L Xiao, Z Fan, and Z Jinxiu. Lattice-parameter variation with carbon content of martensite. i. x-ray-diffraction experimental study. *Physical Review B*, 52(14):9970, 1995.
- L Xie, H Liu, and W Yang. Adapting the nudged elastic band method for determining minimum-energy paths of chemical reactions in enzymes. *The Journal of Chemical Physics*, 120(17):8039–8052, 2004.
- C Zener. Theory of strain interaction of solute atoms. *Physical Review*, 74(6):639, 1948.
- Y Zhang, X Zhao, N Bozzolo, C He, L Zuo, and C Esling. Low temperature tempering of a medium carbon steel in high magnetic field. *ISIJ international*, 45(6):913–917, 2005.
- C Zhang, M Zhou, X Yu, L Ma, and F Yu. Modified iron-carbon as heterogeneous electro-fenton catalyst for organic pollutant degradation in near neutral ph condition: Characterization, degradation activity and stability. *Electrochimica Acta*, 160:254–262, 2015.

- J Z Zhao, A K De, and B C De Cooman. Kinetics of cottrell atmosphere formation during strain aging of ultra-low carbon steels. *Materials Letters*, 44(6):374–378, 2000.
- J Z Zhao, A K De, and B C De Cooman. Formation of the cottrell atmosphere during strain aging of bake-hardenable steels. *Metallurgical and Materials Transactions A*, 32(2):417–423, 2001.
- F Zhong, X Liu, J Zhang, M Kang, and Z Guo. Lattice-parameter variation with carbon content of martensite. II. long-wavelength theory of the cubic-to-tetragonal transition. *Physical Review B*, 52(14):9979, 1995.
- X W Zhou, R A Johnson, and H N G Wadley. Misfit-energy-increasing dislocations in vapor-deposited CoFe/NiFe multilayers. *Physical Review B*, 69(14):144113, 2004.
- C Zhu, A Cerezo, and G D W Smith. Carbide characterization in low-temperature tempered steels. *Ultramicroscopy*, 109(5):545–552, 2009.



FOLIO ADMINISTRATIF

THESE DE L'UNIVERSITE DE LYON OPEREE AU SEIN DE L'INSA LYON

NOM : Waseda
(avec précision du nom de jeune fille, le cas échéant)

DATE de SOUTENANCE : 13 décembre 2016

Prénoms : Osamu

TITRE : Atomic scale investigation of ageing in metals

NATURE : Doctorat

Numéro d'ordre : 2016LYSEI150

Ecole doctorale : ED34

Spécialité : Matériaux

RESUME : Selon la théorie de Cottrell et Bilby, les dislocations à travers leur champ de contrainte interagissent avec les atomes de soluté qui s'agrègent au cœur et autour des dislocations (atmosphère de Cottrell). Ces atmosphères « bloquent » les dislocations et fragilisent le matériau. Dans cette thèse, les techniques de simulations à l'échelle atomique telles que la Dynamique Moléculaire, les simulations Monte Carlo Cinétique, Monte Carlo Métropolis ont été développées qui permettent de prendre en compte les interactions entre plusieurs centaines d'atomes de carbone et la dislocation, pour étudier la cinétique de formation ainsi que la structure d'une atmosphère de Cottrell. Par ailleurs, la technique de simulation est appliquée à deux autres problématiques: premièrement, il est connu que les atomes de C dans la ferrite se mettent en ordre (mise en ordre de Zener). La stabilité de cette phase est étudiée en fonction de la température et la concentration de C. Deuxièmement, la ségrégation des atomes de soluté dans les nano-cristaux de Ni ainsi que la stabilité des nano-cristaux avec les atomes de soluté dans les joints de grain à haute température est étudiée.

MOTS-CLÉS : Atmosphère de Cottrell, Mise en ordre de Zener, Stabilité des nano-cristaux, Monte Carlo Cinétique, Monte Carlo Métropolis, Dynamique Moléculaire

Laboratoire (s) de recherche : MATEIS METAL

Directeur de thèse: PEREZ Michel

Président de jury : BECQUART Charlotte

Composition du jury : NEUGEBAUER Jörg, RODNEY Davide, RIBEIRO Fabienne, JELEA Andrei, MORTHOMAS Julien, CHANTRENNE Patrice